7-17-2009

Motion Correction Algorithm of Lung Tumors for Respiratory Gated PET Images

Jiali Wang
Florida International University, jiali.wang@fiu.edu

DOI: 10.25148/etd.FI09082401

FLORIDA INTERNATIONAL UNIVERSITY

Miami, Florida

MOTION CORRECTION ALGORITHM OF LUNG TUMORS FOR RESPIRATORY GATED PET IMAGES

A dissertation submitted in partial fulfillment of the

requirement for the degree of

DOCTOR OF PHILOSOPHY

in

BIOMEDICAL ENGINEERING

by

Jiali Wang

2009

To: Dean Amir Mirmiran
College of Engineering and Computing

This dissertation, written by Jiali Wang, and entitled Motion Correction Algorithm of Lung Tumors for Respiratory Gated PET Images, having been approved in respect to style and intellectual content, is referred to you for judgment.

We have read this dissertation and recommend that it be approved.

Malek Adjouadi, Ph.D.

Giri Narasimhan, Ph.D.

Wei-Chiang Lin, Ph.D.

Juan M Franquiz, Ph.D.

Anthhony J. Mcgoron, Ph.D., Major Professor

Date of Defense: July 17, 2009

The dissertation of Jiali Wang is approved.

8/5/09

Dean Amir Mirmiran
College of Engineering and Computing

Dean George Walker
University Graduate School

Florida International University, 2009

DEDICATION

I dedicate this dissertation to my family. To my parents, my dear wife and my newborn baby boy, who have always been a source of encouragement and inspiration throughout my life and without whose understanding, guidance, support and most of all love, I would not have the goals I would have to strive, and be the best to realize my dreams. I love you all!

ACKNOWLEDGEMENTS

The completion of this work would not have been possible without the support and assistance of my professors, colleagues and friends. My sincere gratitude goes first and foremost to my advisor, Dr. Anthony J. Mcgoron for providing me with the opportunity to work on this research project; for his patience, motivation, enthusiasm, and immense knowledge; and for his sponsorship through my Ph.D's study.

Besides my advisor, I would like to thank the rest of my dissertation committee members: Dr. Wei-Chiang Lin, Dr. Giri Narasimhan and Dr. Malek Adjouadi for their insightful comments and advices on my dissertation.

A special thanks to Dr. Juan M. Franquiz for his original idea of this dissertation, and for his continued guidance, instruction and encouragement. Thank you to Dr. James Byrne for whose expert advice and helpful insights on this project and for his assistance with designing and preparing my experiments. Lastly, I offer my regards and blessings to all of those who supported me in any respect during the completion of this dissertation.

This work is supported in part by research grant from the National Institutes of Health (NIH R15CA118284-01) and FIU University Dissertation Year Fellowship.

ABSTRACT OF THE DISSERTATIOIN

MOTION CORRECTION ALGORITHM OF LUNG TUMORS FOR RESPIRATORY GATED PET IMAGES

by

Jiali Wang

Florida International University, 2009

Miami, Florida

Professor Anthony J. Mcgoron, Major Professor

Respiratory gating in lung PET imaging to compensate for respiratory motion artifacts is a current research issue with broad potential impact on quantitation, diagnosis and clinical management of lung tumors. However, PET images collected at discrete bins can be significantly affected by noise as there are lower activity counts in each gated bin unless the total PET acquisition time is prolonged, so that gating methods should be combined with imaging-based motion correction and registration methods.

The aim of this study was to develop and validate a fast and practical solution to the problem of respiratory motion for the detection and accurate quantitation of lung tumors in PET images. This included: (1) developing a computer-assisted algorithm for PET/CT images that automatically segments lung regions in CT images, identifies and localizes lung tumors of PET images; (2) developing and comparing different registration algorithms which processes all the information within the entire respiratory cycle and integrate all the tumor in different gated bins into a single reference bin. Four registration/integration algorithms: Centroid Based, Intensity Based, Rigid Body and Optical Flow registration were compared as well as two registration schemes: Direct

Scheme and Successive Scheme. Validation was demonstrated by conducting experiments with the computerized 4D NCAT phantom and with a dynamic lung-chest phantom imaged using a GE PET/CT System. Iterations were conducted on different size simulated tumors and different noise levels. Static tumors without respiratory motion were used as gold standard; quantitative results were compared with respect to tumor activity concentration, cross-correlation coefficient, relative noise level and computation time. Comparing the results of the tumors before and after correction, the tumor activity values and tumor volumes were closer to the static tumors (gold standard). Higher correlation values and lower noise were also achieved after applying the correction algorithms. With this method the compromise between short PET scan time and reduced image noise can be achieved, while quantification and clinical analysis become fast and precise.

TABLE OF CONTENTS

LIST OF TABLES

LIST OF FIGURES

FIGURE PAGE

1. INTRODUCTION

Lung cancer is one of the most common types of cancers in the United States, with more than 161,000 deaths per year [1]. The early and most probable curable stage of the disease in all histological types is the solitary pulmonary nodule (SPN) [2, 3], a well-circumscribed, small, rounded, dense pulmonary tumor. Five-year survival for post operation of stage I lung cancer and nodules smaller than 3 cm has been reported to be over 80% [4] . Each year there are approximately 150,000 SPNs being identified in the United States [2]. Of those, about 30% to 40% are malignant nodules [5]. Since the early treatment of a small SPN has a high probability of curability, accurate definition of tumor volume and position is especially important. Computed tomography (CT) is the most common imaging technique for providing anatomical and morphological information of tumors in the body. Since its advent, especially the helical or spiral CT, the sensitivity of detecting SPNs has increased significantly while decreasing the limit of the size of detected nodules to smaller than 3 mm [6-8]. However, a vast majority of small SPNs appear on CT as indeterminate tumors [9, 10]. In this situation molecular imaging with ^{18}FDG-PET as a non-invasive procedure for differentiating malignant from benign SPNs has been proposed and successfully used [11-15].

Molecular imaging with ^{18}FDG-PET provides significantly higher sensitivity (87%) and specificity (91%) than CT (68% and 61%, respectively) in detection and characterization of malignant lung nodules [16-19]. It has become a popular imaging modality for lung cancer diagnosis, staging, monitoring response to treatments, and for differentiating tumor recurrence from scarring and other benign structures. The major advantage of ^{18}FDG-PET over other imaging modalities is that ^{18}FDG-PET allows imaging molecular

processes *in vivo*. The radiotracer ^{18}FDG is a glucose analogue that is trapped intracellularly during glucose metabolism [20, 21]. The increased glycolysis in cancer cells increases the number of glucose membrane transporters and consequently the uptake of ^{18}FDG-PET molecules, so the accumulation of the radiotracer when imaged by PET easily distinguishes malignant from benign cells [22]. This fact has also lead to the use of molecular imaging fused with CT for defining a more accurate delineation of tumor volume in radiation therapy planning [19, 23].

Even with the advances of PET and CT, only about 15% of SPNs are being detected at an early stage[24-26]. One major inconvenience of ^{18}FDG-PET imaging is the relatively long scan time (usually 5 to 7 minutes). Many clinical and research studies have shown that, in ^{18}FDG-PET, respiratory motion degrades the quality of the images by blurring and distorting the real size, shape and position of the tumors , reducing SUV (standardized uptake value) and tumor-to-background ratio. Artifacts created by respiratory motion can negatively impact the application of ^{18}FDG-PET for the detection and quantitation of small tumors, and for monitoring response to treatment and radiation therapy planning [27, 28]. At the present time there is no standard and validated practical methodology in the context of clinical PET studies to compensate respiratory motion.

2. BACKGROUND

2.1. Lung Cancer

Lung cancer is a disease caused by the rapid growth and division of cells in lung tissue. Despite the large development of medical science in last decades, lung cancer causes more deaths than any other cancer in the world. It accounts for 14% of all cancers and 28% of all cancer deaths every year in the United States [1, 29]. For therapeutic, biological and clinical reasons, lung cancers are divided into two major groups, which make up more than 90% of all lung cancer cases: small cell lung cancer (SCLC) and non-small cell lung cancer (NSCLC). NSCLC is more common and can spread to different parts of the body. SCLC makes up about 15% to 20% of all lung cancer cases and is far more aggressive than NSCLC [20].

Approximately 30% of new cancers present as solitary pulmonary nodules. Determining the malignancy of an SPN is an integral and challenging part of diagnosis. The features indicating malignancy include [12, 20-22]:

- Size: the larger the nodule the more likely it is to be malignant, however 42% of cancers are less than 2 cm at presentation.
- Margin characteristics: malignant SPNs tend to be irregular lobulated or speculated, however 20% of cancers may have a smooth margin and appear benign.
- Growth: the doubling time of a nodule in volume, ranging from 15 to 450 days. Any tumor that increases in size over a two-year period of observation, or less, must be considered malignant until proven otherwise.
- Metabolism: neoplastic tissue demonstrates increased glucose metabolism compared to normal tissues.

Therefore better and more accurate estimation of size, growth rate, and metabolic activity of lung tumors may improve diagnosis. But in most cases, it is hard to detect the lung cancers early because symptoms usually do not appear until the disease is advanced. The tendency of early spread of lung cancer and a late diagnosis usually results in the increasing incidence of lung cancer. Survival from lung cancer is highly dependent on the clinical stage. Appropriate staging of the patient determines the surgical respectability and ultimately the prognosis [23, 27, 30].

2.1.1 Staging

Staging is the process of finding out how localized or widespread the cancer is [21, 22] It is usually based on the tumor size, whether lymph nodes contain cancer, and how far the cancer has spread within the lung and to other parts of the body. Staging is a major indicator of the curative potential and the limitations of available therapy for lung cancer to date. It distinguishes people with limited disease from those with distant metastases. The value of staging lies in its ability to identify consistent, reproducible, patient groups that may help the physician to choose appropriate treatment for each patient.

The system used to describe the growth and spread of non-small cell lung cancer (NSCLC) is the TNM staging system as shown in Table 2.1 [31, 32] where T refers to the size of tumor, N represents regional node involvement and M represents metastasis status. Lung cancer treatment ultimately depends upon such staging. In general, the lower the stage, the more favorable is the individual's prognosis. This study attempts to improve the estimate of tumor size, which will improve the accuracy of its staging.

Stage	TNM subset
Stage 0	Carcinoma *in situ*
Stage IA	T1 N0 M0
Stage IB	T2 N0 M0
Stage IIA	T1 N1 M0
Stage IIB	T2 N1 M0, T3 N0 M0
Stage IIIA	T3 N1 M0, T1 N2 M0 T2 N2 M0 T3 N2 M0
Stage IIIB	T4 N0 M0, T4 N1 M0, T4 N2 M0, T1 N3 M0, T2 N3 M0
Stage IV	T (any) N (any) M1

Table 2.1 Stage determinations using TNM staging system [31, 32].

2.1.2 Diagnosis and Treatment

A wide range of diagnostic procedures and tests has been used to diagnose lung cancers:

- Sputum can be collected and examined microscopically for the presence of malignant cells which have sloughed from the surface of the tumor.
- Bronchoscopic is a visual examination of the windpipe and lung branches using a flexible scope.
- Needle biopsy may be performed on suspicious areas in the lungs or pleura. A small sample is taken of the tissue for analysis.
- Bone scan may also be performed to rule out suspicions of metastasis to the bones.

Conventional noninvasive diagnostic techniques include chest radiography, Computed Tomography (CT), Magnetic Resonance Imaging (MRI) and Positron Emission Tomography (PET) [33].

Depending on the type and stage of the disease, lung cancer can be treated with surgery, chemotherapy, radiation therapy, or a combination of these treatments [23].

- *Surgery*: often used for non-small cell lung cancers which have not spread beyond the lung. Three surgical procedures have been commonly used: wedge resection (removal

- *Chemotherapy*: for patients whose tumors are somewhat more advanced, e.g., larger tumors that have not spread from the lung.
- *Radiotherapy*: utilizing high-energy, ionizing radiation (e.g., gamma rays) to kill cancer cells, used in more aggressive or widespread tumors. It can be applied to shrink a tumor that is later removed by surgery, to relieve symptoms, or to destroy malignant cells in a tumor that cannot be removed surgically.

Evaluation of the treatment result plays a major role in the management of lung cancer. It may help in avoiding unnecessary attempts at curative surgery in patients with un-resectable mediastinal disease. Monitoring of anti-tumor therapy is conventionally performed by sequential determination of tumor size using morphological imaging modalities like CT/MRI. Early and accurate detection and staging can improve prognosis.

2.2 Non-Invasive Imaging Modalities in Lung Cancer Management

2.2.1 Chest Radiography

X-ray imaging, also known as radiographs or roentgenograms has been developed over the past 100 years. It is based on the absorption of X-rays as they pass through different parts of the body, interact with a detection device (such as X-ray film) and provide a 2-dimensional projection image. The picture appears on the film as a "negative" type picture, the denser a structure is, the whiter it looks. For example, muscle or soft tissue appears dark on an X-ray film while solid tissue like bones appears very white. The chest X-ray is the most commonly performed diagnostic X-ray examination, used for initial

study for the diagnosis of lung cancer (Figure 2.1). It has excellent spatial resolution (0.17 mm) [34] and good penetration depth.

Disadvantages: The chest X-ray is a 2D image, so no volumetric analysis can be performed on X-ray images. It has ionizing radiation, poor contrast among soft tissues. It overlooks 10% of lung cancer in non-calcified tumors and is also poor for detailing the primary tumor's involvement with mediastinal structures or with the chest wall [34].

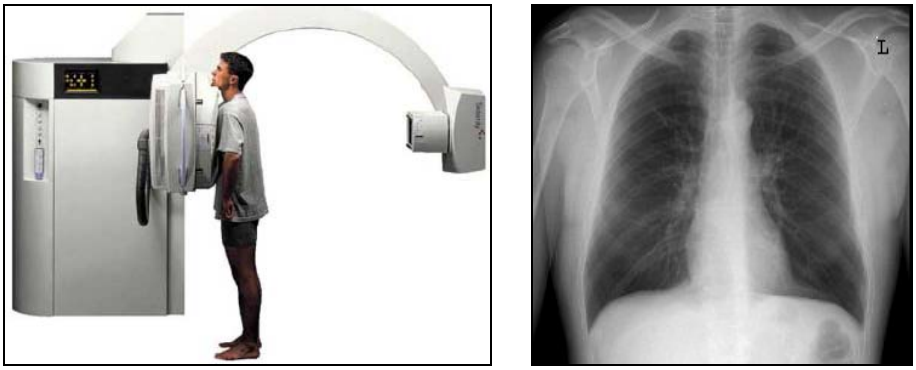

Figure 2.1 X-ray machine and Posterio-anterior view of one chest radiography image. (source: http://www.radiologyinfo.org/)

2.2.2 Computed Tomography Imaging

CT, also referred as "CAT scanning" (Computer Axial Tomography scanning), was first introduced by Hounsfield in 1971. He was awarded the Nobel Prize for this invention in 1979 [14]. It is now the most common imaging technique for providing anatomical information on the size and location of tumors in the body.

CT techniques enable 2D and 3D external and internal visualizations of objects. Conventional radiographs depict a three dimensional object as a two dimensional image, on which overlying tissues are superimposed [35]. CT overcomes this problem by obtaining images from different angles using special X-ray equipment, and then reconstructing them to create a cross-section of body tissues and organs. The CT image

preserves full spatial information, and it can show bone, soft tissues, and blood vessels in the same image [36]. Since the advent of CT, the sensitivity of detection significantly increased while the size of the nodule being detected reduced to less than 3 mm [35, 36]. The spatial resolution of CT is also very good (0.4 mm). Faster spiral CT scan times (less than 1 second) and thinner collimation (1 to 2 mm) have allowed detecting small tumors that could be missed by conventional CT scanners because of respiratory motion and partial volume effect [37]. CT can identify the malignancy of a number of nodules according to their density, calcification, morphological features, growth and size [4].

Disadvantages: Volumetric analysis of CT requires a time consuming tracing of tumor contours in a stack of slices [38]. It has high ionizing radiation; i.e., a typical abdomen CT uses about 50 times the amount of radiation used for a chest X-ray [39]. The specificity of CT to distinguish malignant and benign tumors is generally low as CT can only measure anatomy not function, lots of malignant tumors appear on CT as indeterminate [21, 22, 30]. For lymph node size less than 1 cm diameter it may be difficult to identify its metastases or to differentiate between malignant and enlarged reactive nodes in clinical staging. Changes in function resulting from therapy often occur prior to changes in anatomy and these changes will not show in CT images [35].

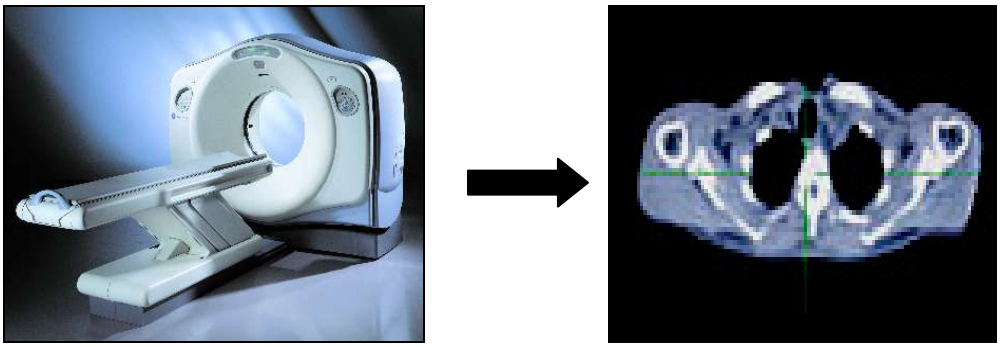

Figure 2.2 CT scanner on the left and CT transaxial slice (through the lung) on the right (Source: http://www.wiproge.com/)

2.2.3 ^{18}FDG-Positron Emission Tomography

Positron Emission Tomography (PET) is a type of nuclear medicine imaging technique that involves cross sectional data acquisition and reconstruction like CT. It has become an important technique in imaging certain diseases such as disorders of the brain, the heart, the lung, and other organs.

PET imaging starts with the injection of a radioactive tracer isotope (e.g., ^{11}C, ^{15}O, ^{18}F) [19, 40], which decay by emitting a positron. The emitted positron collides with a free electron usually within a few millimeters from the emission point. The annihilation of the two subatomic particles produces a pair of 511 keV gamma rays moving in two opposite directions, and is detected by an array of detectors surrounding the patient. This mechanism of positron annihilation and generation of the two photons is very well shown in Figure 2.3. Only when pairs of detectors register photons simultaneously is the annihilation event recorded and processed. After enough annihilation events have been collected, the positron emitting tracer distribution is computed by tomography reconstruction procedures. Two-dimensional images are then reconstructed by PET. Multiple two-dimensional image planes are stacked to form a three-dimensional volume.

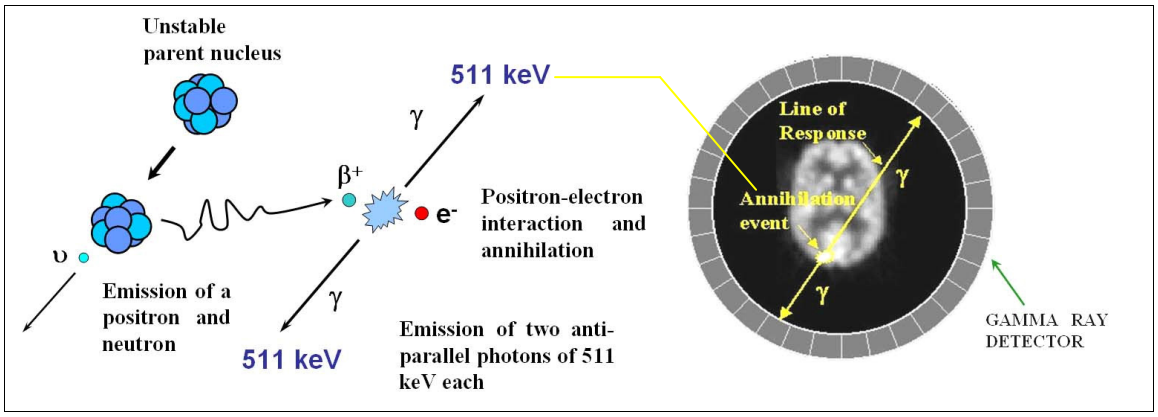

Figure 2.3 Positron annihilation and two 511 keV photons generated at an angle of 180˚ and detected by two opposing gamma ray detectors [28].

The most widely used radioactive isotope for PET in oncology is Fluorine-18-fluorodeoxyglucose (^{18}F-FDG) with a half life of approximately 110 minutes [25]. The development of ^{18}F-FDG has been the major factor in expanding the clinical role of PET imaging and the development of PET instrumentation. ^{18}F-FDG is relatively easy to synthesize with a high radiochemical yield. It is taken up by the cell, and not metabolized to CO_2 and water. It remains trapped within tissue, which makes it well suited to use as a glucose uptake tracer because glucose supplies 90-95% of the energy to the brain and the other part of the body and is therefore used as an indicator of energy requiring brain/body functions. This is of interest in oncology because proliferating cancer cells have a higher than average rate of glucose metabolism. The structure of positron emitting isotope FDG, is as shown below [19].

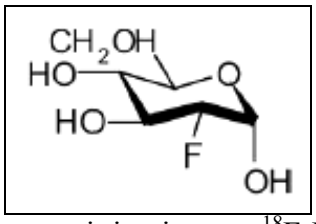

Figure 2.4 Structure of positron emitting isotope ^{18}F-FDG [19].

The sensitivity of ^{18}FDG-PET in identifying malignant nodules (greater than 1 cm) has been reported from 89% to 100%, specificity from 78% to 100%, positive predictive value from 86% to 94% and negative predictive value from 89% to 100% [7, 33, 37]. A negative ^{18}FDG-PET scan could be an indication to observe and follow-up a nodule that otherwise would require biopsy or surgery. A positive ^{18}FDG-PET scan indicates a high probability of malignancy and justifies an invasive management of the tumor [16, 17].

Disadvantages: Long acquisition time: usually takes 5-7 minutes per body position. Lack of anatomical reference for metabolic images and inaccurate quantitation of the radiotracer uptake in tumors due to the photon attenuation by the surrounding tissue. Photons that scatter or are absorbed by the tissue lead to a loss in detected events, which would otherwise have been recorded, would lead to higher image noise and image non-uniformity [33, 41]. Also PET images have low resolution (5 mm) due to the limitation of detectors, finite size of the voxels and the fact that the object structure varies rapidly over the region (tissue inhomogeneity) give rise to partial volume effect.

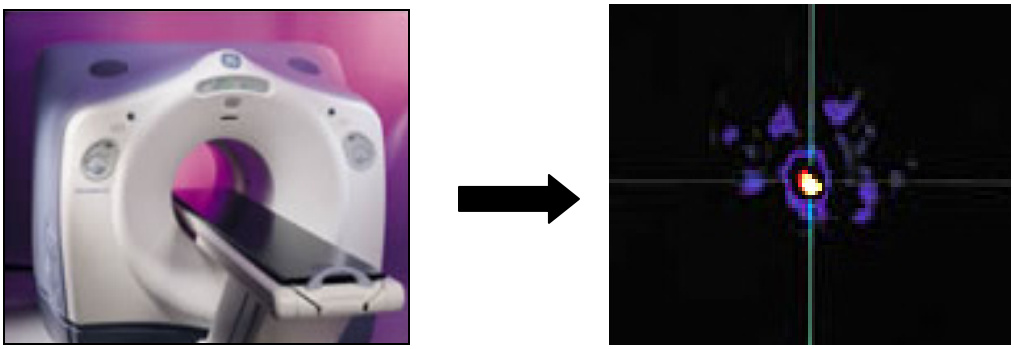

Figure 2.5 PET scanner on the left and PET transaxial slice (through the lung) on right. (Source: http://www.wiproge.com)

2.2.4 Hybrid PET/CT Scanners

The powerful prognostic information provided by PET can be enhanced by the incremental information provided by CT assessment. Several co-registration techniques were developed to fuse morphological imaging studies with PET including the use of fiducial markers and software programs that enable the translation, rotation, scaling, and warping of image data sets, but they were time consuming and less reliable for head neck and abdominal regions. The Hybrid PET/CT scanner (Figure 2.6) has been developed to compensate for both the attenuation of photons and the lack of anatomical reference in PET. It generates accurately co-registered PET and CT images (Figure 2.6) that help discriminate areas of physiologic uptake from malignant tumors in situations where conventional PET or CT alone is unclear [42]. Precisely localized PET information can be used to plan surgical and medical therapy and in doing so, improve the management of patients with malignant disease.

The advantages of the Hybrid PET/CT include: PET and CT are combined and the CT images can be used to construct an attenuation correction map. This attenuation map is noise-free, thus a practical solution is obtained for the need of a very rapid, low-noise and quantitatively correct method of PET attenuation correction. CT provides the anatomic framework needed for PET images. And PET and CT images can be automatically registered with sub-millimeter accuracy.

Disadvantages:

- The array of detectors detects two gamma rays with energy of 511 keV for PET imaging, whereas for CT imaging, the transmission energy is between 80 - 140 keV. Since the attenuation coefficients are energy-dependent, coefficients measured at CT

- CT acquisition only takes a few seconds while PET acquisition takes a few minutes. During long PET acquisition time, there will be respiratory motion, and this will make attenuation correction difficult because the images don't match for organs that move with respiration.
- Involuntary patient motion in the form of respiratory or cardiac motion might affect the automatic registration of PET and CT images [44, 45].

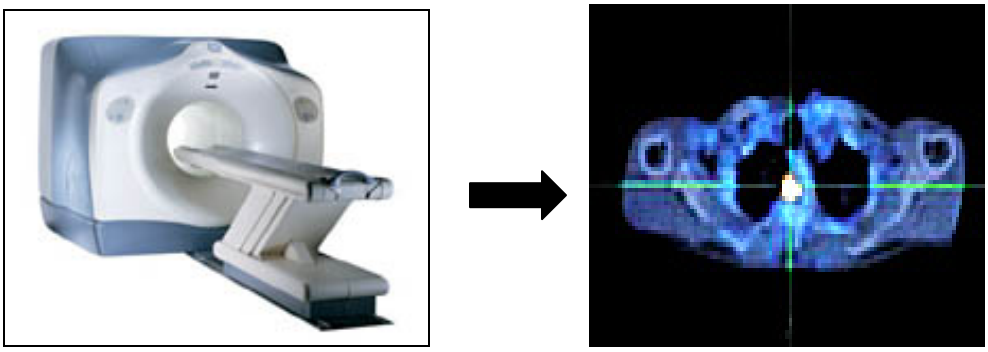

Figure 2.6 Hybrid PET/CT scanner on the left and PET/CT transaxial slice (through the lung) on the right. (Source: http://www.wiproge.com/)

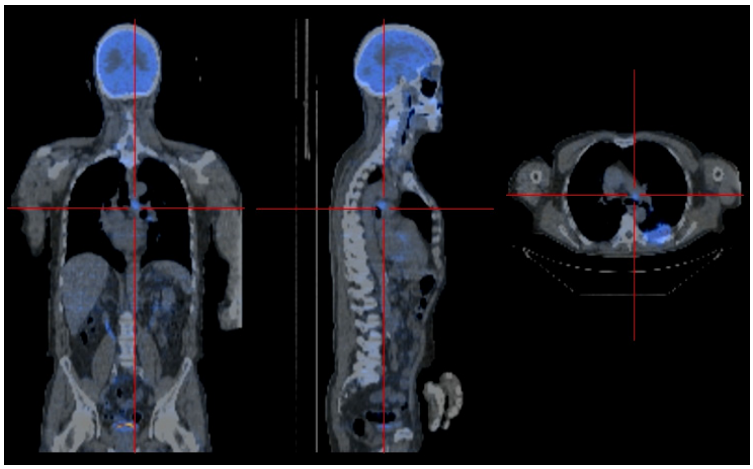

Figure 2.7 Fused PET and CT coronal, saggital and transaxial slices taken using the Hybrid PET/CT, Discovery LS from GE Medical systems (courtesy of GE Medical Systems).

2.2.5 Standardized Uptake Value

Positron Emission Tomography allows quantification of radioactivity concentrations inside the body which can be used to estimate glucose uptake of malignant tumors. There are many complex approaches to estimate glucose utilization rate, e.g. quantitative measurement of FDG, but the SUV (standardized uptake value) method is most commonly used. It is defined as a ratio of tissue radioactivity concentration of FDG (*KBq/ml*) in a structure encompassed by a ROI (region of interest) at time *T* (*C(T)*) divided by the injected dose (*KBq*) per gram body weight (*kg*), body surface area, or lean mass [45, 46].

$$SUV = \frac{C(T)}{Injected\ \ dose / Body\ \ weight},$$

where *C(T)* = FDG concentration in tissue at time *T*.

SUV is determined by the manual selection of voxels, and the maximum or average value of radioactivity concentration of FDG in a selected ROI, and these values need to be measured at a fixed time point. Calculations of SUV are computationally simple and require considerably less time than dynamic acquisition protocols. However they do require attenuation correction being performed as well as calibration of the system.

SUV is the most clinically utilized quantitative parameter of FDG accumulation. It is a frequently used parameter to differentiate tumors as malignant or benign, to classify disease stage, and to monitor their response to treatment. Studies show that the SUV of FDG is significantly higher in recurrent tumors than in non-cancerous tumors. A SUV cutoff threshold, combined with other parameters like the tumor location and shape, may

indicate the tumor's malignancy. Reports show that a SUV cutoff threshold for tumor malignancy ranging from 2.5 g/ml to 5.0 g/ml [47].

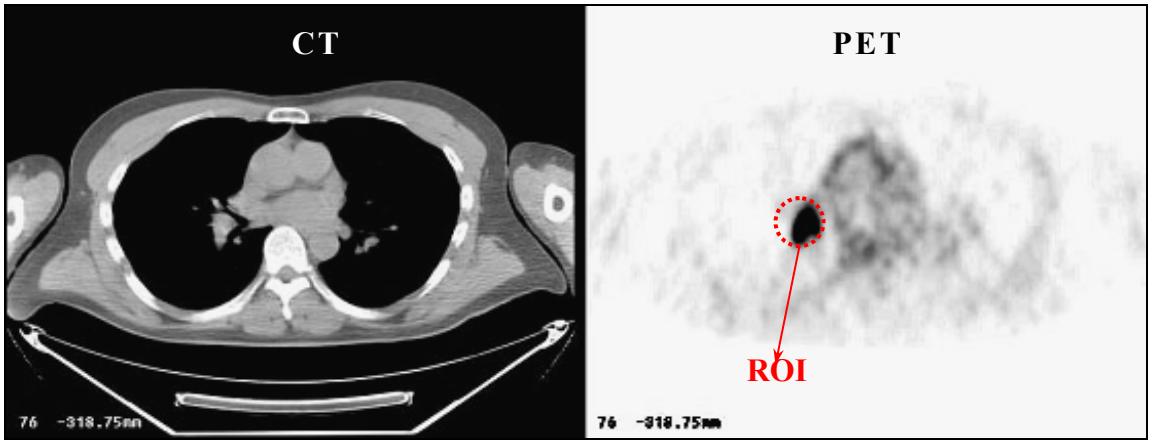

Figure 2.8 SUV is determined by manual selection of voxel, the maximum or average FDG concentration value in a selected ROI. SUV measurement in combination with other parameters is used to make the final assessment of the disease status.

SUV > 2.5: associated with lung malignancy

SUV > 5.0: prognostic value for recurrence NSCLC (Non-small cell lung cancers) stage I

SUV > 10.0: prognostic value independent of clinical stage and tumor size [47, 48]

One major disadvantage of SUV is its lack of precision. It is expressed by the maximum or average value of FDG concentration in an arbitrary region of interest that can include hypoxic or hypo-metabolic regions around the tumor's viable mass. The great variance of data affects individualized diagnosis or prognosis [47]. Another limitation of the SUV method in monitoring therapy is that it is highly dependent on the time of measurement. The SUV value of a malignant tumor was shown to increase gradually up to 90 minutes post injection [26]. So SUVs should only be compared among different cases at the same time after tracer injection.

2.3 Respiratory Motion Artifacts in ^{18}FDG-PET

The use of combined PET/CT provide a convergence of metabolic and anatomic imaging, with an accurate anatomical framework for molecular imaging and a noise free CT map for more accurate attenuation correction and, consequently, quantitation of ^{18}FDG uptake and characterization of lung tumors [37]. However, the relatively long acquisition time of ^{18}FDG -PET images, compared to the shorter CT collection time can produce some PET-CT mis-registration as a consequence of respiratory motion [33].

Many clinical studies and research papers have demonstrated how image quality is degraded by respiration [49]. Respiratory motion artifacts can distort target sizes and result in locating errors as different parts of the tumor move in and out of the image window during the patient's breath cycle. Some studies have reported that typical lung tumor motion displacement with respiration can range from 3 to 22 mm. Fluoroscopic studies [29] have also demonstrated that the tumors next to the diaphragm can move in a range of 30 mm, which is more than four times the 5 to 6 mm full width half-maximum (FWHM) resolution of current PET scanners.

2.3.2 Respiratory Gating in Radiation Therapy

The breathing motion of lung tumors has received particular attention in radiation therapy. Treatment planning estimates boundaries surrounding the tumor large enough to ensure delivering dose to the target region. But breathing motion could result in overestimating the tumor volume, leading to an increase in the planning target volume. That can mean healthy tissues nearby receive more radiation exposure than is necessary, which may lead to treatment-related complications.

Different respiratory gating systems have been proposed to synchronize the radiation beam with the position of the tumor in order to reduce the planning target volume [49]. These systems have included the indirect detection of tumor motion with different sensors, fluoroscopic real-time tumor tracking synchronized with a linear accelerator and breath-hold gating techniques [50, 51]. The common objective has been to irradiate the tumor in a time bin within the respiratory cycle in which the tumor can be considered almost static. To allow irradiation of moving tumors only during time intervals predefined by the user, Varian Medical Systems (Palo Alto, CA) has developed the Real-Time Position Management (RPM) Respiratory Gating System [52, 53] (Figure 2.9). The RPM tracks the vertical motion using an infrared video camera of two passive reflective markers on a plastic box placed on the patient's abdomen. A PC with vendor software digitizes the video signal and allows the user to select a trigger pulse at a specific amplitude or phase within the respiratory cycle. A clear and concise description of the RPM system and its operation can be found in Nehmeh et al. [54, 55]. This system, originally designed for respiratory gating in radiation therapy, has been used by the group for preliminary testing and assessment of respiratory gated PET scans.

Another respiratory gating system (AZ-773V) was developed in Japan in 2002 (Anzai Medical, Tokyo, Japan) [56, 57]. The AZ-733V System employs a respiratory sensor (strain gauge, Figure 2.10) which can be fastened around the patient's abdomen or thorax by hook and loop tape. The sensor detects the mechanical expansion of the thoracic cavity resulting from the respiratory motion as the pressure changes of up/downward movement of the chest and abdomen. The system was interfaced with the Siemens linear accelerator via an open gating portal and it outputs the gating signal that triggers beam on

and off. With the gating signal radiation therapy equipment can control the radiation beams to be restricted within the target range, reducing the dose being delivered to surrounding healthy tissues.

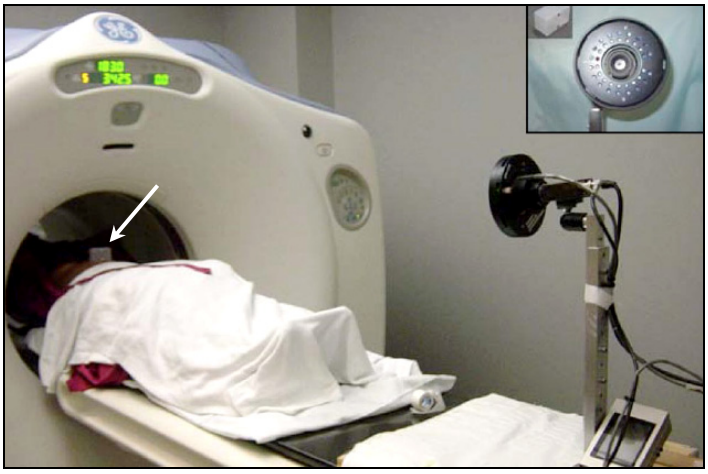

Figure 2.9 Patient setup in RPM acquisition mode. Plastic block (arrow) with two infrared passive reflectors is positioned on the abdomen of the patient. Infrared camera, positioned on the PET table, is used to trace the motion of reflectors and, thus, patient breathing motion [52].

(a)

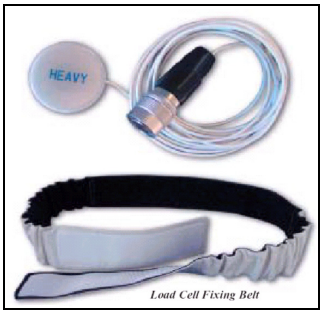

(b)

Figure 2.10 AZ-773V system: (a) PC system, (b) respiratory sensor. AZ-773V system monitors the respiratory movement by the strain gauge sensor and outputs the gating signals. (Source: http://www.anzai-med.co.jp)

2.3.3 Respiratory Gating of ^{18}FDG-PET

The requirement for effective attenuation correction, as well as improved spatial resolution, is that PET and CT data correspond to the same respiratory phase and spatial details. The gating of PET scans was initially investigated to compensate myocardial

motion in cardiac PET. Recently, Nehmeh et al [54, 55]. assessed lung motion artifacts in lung cancer and demonstrated more accurate quantitation and definition of PET tumors by dividing the breathing cycle into discrete time bins. The same group has acquired gated PET and CT data at discrete time bins within the respiratory cycle in a PET/CT scanner. They demonstrated higher accuracy of SUV determinations by reconstructing PET data with their corresponding binned CT data [41].

POLARIS is a high-resolution tracking system being developed. It is an infrared (IR) optical-electronic motion tracking device using four IR-reflective spheres [58]. The system has the advantages that it is not sensitive to room lighting conditions and takes much less disk space to store the IR-tracker output compared to optical image sequences. There are also efforts reported recently by the group in the University of Texas M. D. Anderson Cancer Center, which utilized a solid-state thermometer to detect the temperature difference of the air flow in the nostril due to inhalation and expiration [41, 59], as during expiration the air temperature in the nostril is expected to be higher than that during inspiration, since the exhaled air has been warmed by the lungs.

Figure 2.11 The POLARIS system uses four infrared-reflective spheres placed in a precisely known geometry [58].

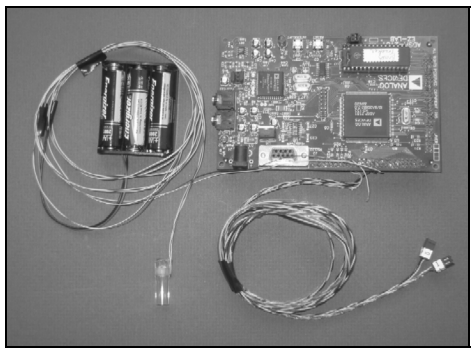
(a)
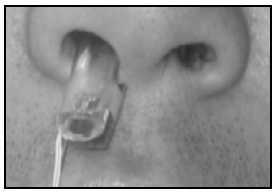
(b)

Figure 2.12 (a) temperature sensor respiration gating system and (b) the nostril sensor piece was tested by a volunteer [59].

All these methods have demonstrated the quantitative and qualitative benefits of reducing the blurring of tumors by taking images at discrete time bins within the respiratory cycle, however they have some drawbacks such as patient discomfort, implementation complexity, or relatively high cost. Also, PET images collected at discrete time bins within the breathing cycle can be significantly affected by noise as only one gate is used for reconstruction [60]. To achieve the same radioactive count statistics as in the un-gated images, a proportionally larger amount of the radio-tracer must be administered to the patient or the total PET acquisition time must be prolonged which are not practical options under normal clinical circumstances.

2.3.4 Non-gating Methods for Respiratory Motion Correction in PET

Several image-based and projection-based algorithms have also been developed to correct for motion artifacts in PET without the need for gating. The advantage of these methods compared to gating is that they are not affected by low statistical counts and require no additional patient set-up time. There is a comprehensive review of motion correction methods in PET being published by Rahmim [58]. Most are for brain and heart studies.

Lamare et al applied affine transformation to PET data in list mode to correct for respiratory motion without the need for gating [61]. Transformation parameters

accounting for respiratory motion were estimated based on maximizing the normalized mutual information between the reference data and the original data, and the transformation were then applied on the original list mode data. T The corrected and uncorrected list mode datasets were subsequently reconstructed using the One-Pass List mode Expectation Maximization (OPL-EM) algorithm. Similar to this one, Qiao et al have also achieved motion correction by successfully applying non-rigid motion compensation to list-mode computer simulated PET data [62]. The advantage is that no additional instrumentation is required and it can be applied to correct the motion of other organs besides the lungs. While list mode collection is not generally implemented on clinical cameras, it is probably not a limiting obstacle.

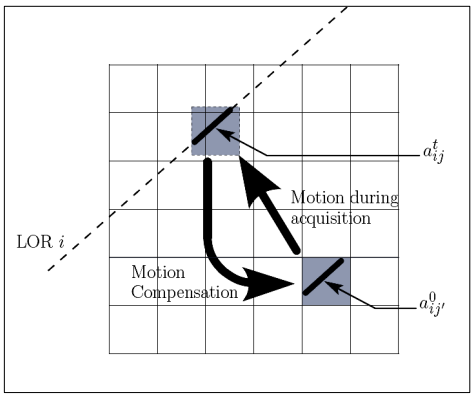

Figure 2.13 Incorporation of the elastic motion (non rigid) compensation during reconstruction of the list-mode PET data [62].

Deconvolution has been applied to reduce lung motion artifact with positive results [63]. A breathing motion model was used to locally estimate the location-dependent tissue location probability function (TLP) due to breathing. The deconvolution process is carried by an expectation-maximization iterative algorithm using the motion-based TLP. The method depends on an estimate of patient motion measured from 4D CT images. Generally, deconvolution methods are theoretically accurate for noise-less data, but

deconvolution tends to amplify the noise in real PET data.

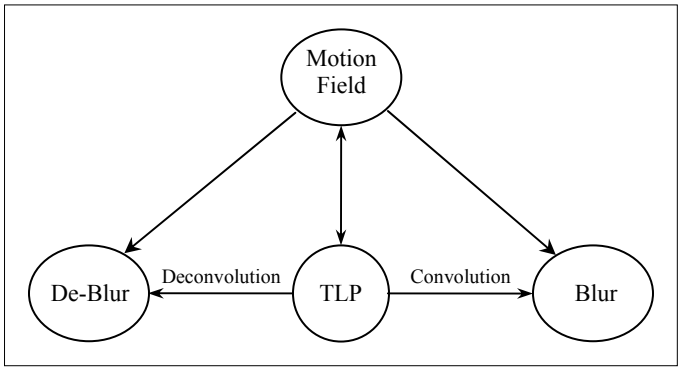

Figure 2.14 A block diagram of imaging and convolution/deconvolution interaction. Tissue motion effects can be removed from images via deconvolution, which requires an estimate of patient motion (TLP) [63].

Recently, Qiao et al [64] presented a region of interest (ROI) based registration method, whereby only the motion map of a user-defined ROI is required and the incorporation of motion into the system model is solely performed within the ROI. Results from the NCAT phantom and a physical phantom show that this method enables faster extraction of motion information and has the potential to achieve more accurate motion compensation. The inconvenience of this method is that the ROI has to be selected manually which makes it subjective to user input.

Another method proposed by Dawood et al [65, 66] using a global optical flow algorithm for motion correcting the individual gates and then combining the gates together. The optical flow tries to find the motion field between two data sets at each pixel position. In their method the entire data set was used to calculated the flow matrix. This is similar to Thorndyke et al's method by retrospective stacking amplitude based binning of data acquired in small time intervals, with rigid or deformable image registration [67]. They reported reduced organ displacements and increased SNR. But these methods require computing over the whole data set which will decrease calculation efficiency. The image

transformation and registration problem continues to be a challenge. To date, such approaches are still being developed and have not been implemented clinically, compared to gating, which is currently being implemented to some extend.

Nehmeh et al demonstrated that lung motion can be corrected without using gating by a method referred to as respiratory-correlated dynamic PET (RCDPET) [41] (Figure 2.13). A radioactive point source (^{68}Ge) attached to a rigid foam block is set on the patient's abdomen and is extended into the camera field of view at the level of the tumor by means of a low-density rod. The position of this source is used as an external reference to track respiratory motion through the consecutive dynamic frames. Image frames corresponding to a user-selected tumor position within the breathing cycle, in correlation with the point source position, are then identified after scanning and are retrospectively reconstructed. This method requires significantly more computation than does gating but does not require tracking hardware. It requires an external point source and the inherent poor spatial resolution of PET cannot match the resolution of cameras used for optical motion tracking. Also here is no motion correction in this method; it is rather a selection of "good" frames. Moreover the tumor position has to be known before scanning.

The non-gating methods are promising because they need not interfere with the current operation of the imaging session, but methods based on external optical tracking are further in clinical application since they are less computationally intensive. Methods using external marker suffer from the disadvantage that the surrogate signal does not directly equate to movement of the tumor. Since gating methods inherently decrease the image signal-to-noise ratio, they should be combined with some imaging-based motion correction methods to register the set of gated images into a single image for analysis.

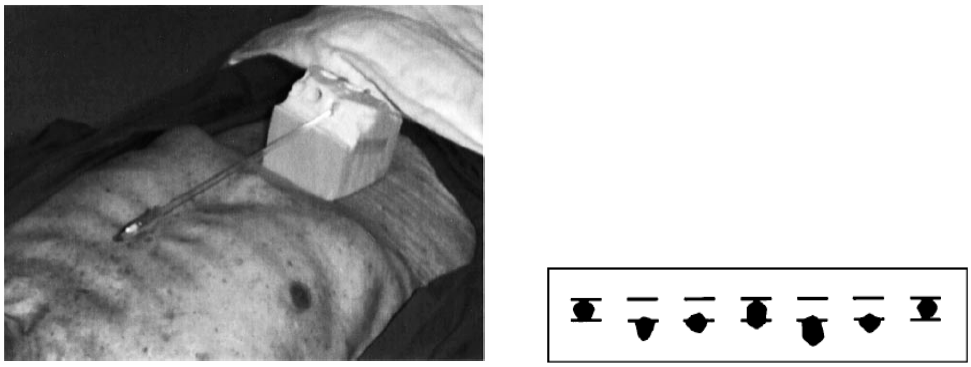

Figure 2.15 On the left, patient setup in RCDPET acquisition mode. Point source is at the end of a low-density rod, extending into the tumor FOV, and rigidly attached to the block positioned on the abdomen of the patient [41]. On the right, position of point source moves in and out of user-selected reference position (e.g., as defined by the 2 lines according to position of point source in first frame).

2.4 Computer Simulation of Respiratory Motion in PET

Respiratory mechanics has been simulated by the four-dimensional (4D) NURBS-based cardiac-torso (NCAT) phantom developed by Segars and Tsui at the University of North Carolina [9, 68-71]. It is a well established simulation program, originally developed to provide a realistic and flexible model of the human anatomy and physiology and is now widely used as a gold standard in nuclear medicine imaging research. The respiratory model was developed using 4D high-resolution respiratory-gated CT normal human data as its basis. The motion of the lung, heart, liver, abdominal organs and diaphragm involved in respiration, were incorporated into NCAT phantom as shown in Figure 2.14. There are many different user-defined parameters, like patient weight, motion extension of chest and diaphragm, heart size or tumor diameter. The NCAT data can hence be generated with great number of degrees of freedom in the simulated anatomy. Combined with accurate models of the imaging process, NCAT is capable of simulating imaging data close to that of real patients. It provides an excellent tool to study the effects of organ and patient movement in SPECT and PET images.

The NCAT phantom can be used to simulate ^{18}FDG distributions of activity and lung tumors. Projection data can be generated using the SimSET or other Monte Carlo simulation programs [9]. The voxelized phantoms are saved as raw binary images without header. Each voxel value in an output image is stored as a 4 byte floating point number (Little Endian). Many applications capable of reading a raw image format can be used to view the phantom images. In this study, Amide [72], a freely available application was used for viewing the phantoms as 2D slices or as 3D volumes.

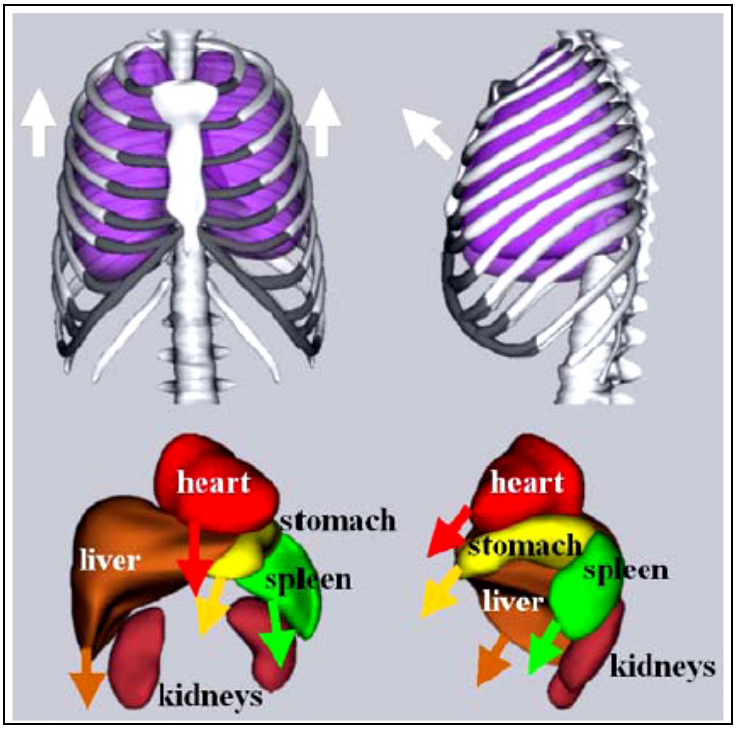

Figure 2.16 Motion of different organs during inspiration simulated in the 4D NCAT phantom. Expiratory motion is modeled in the reverse direction [71].

3. STATEMENT OF PURPOSE

The importance of compensating respiratory motion artifacts in lung ^{18}FDG-PET studies and the feasibility of practical solutions to this problem have been demonstrated by Nehmeh et al. and many other groups [54, 55]. However, at the present time only very few practical methodologies has been implemented in the clinical setting to compensate respiratory motion artifacts in ^{18}FDG-PET scans, and those are vulnerable by less activity counts and higher noise. This project is based on the division of the respiratory cycle into discrete time frames, such as proposed originally by Nehmeh et al. The innovative aspect is to develop an automatic motion track and integration algorithm that includes all the counts collected in the respiratory cycle into solely one reference bin. This proposed method has three major advantages: 1) PET scan time doesn't need to be increased for reducing statistical noise and increasing the signal to noise ratio, 2) the computer-assisted automatic algorithm would facilitate the 3D quantitation of activity and the introduction of the procedure to the clinical practice, and 3) the integration of the information of different bins into one set of tomographic slices, would make easier, faster and more reproducible the clinical interpretation of ^{18}FDG-PET scans.

3.1 Objectives

The overall goal of this study is to develop and validate a fast and practical solution to the problem of respiratory motion for the accurate interpretation and quantitation of ^{18}FDG uptake of lung tumors in lung PET images.

Specific Aims

1) To develop a computer-assisted algorithm for PET/CT images that automatically segments lung regions in CT images, and identifies and localizes focal increases of activity in lung regions of PET images by including the following steps:

- To include an edge detection algorithm based on gradient and gray-level thresholding, in order to define more precisely the borders of the lung.
- To define the optimal percentage of maximum counts to define the volume of tumors in PET scans. This was done experimentally by using the physical phantom and a set of hot spheres of known volume and activity.

2) To develop and compare different integration/registration algorithms. These algorithms will process all the information within the respiratory cycle; and include all the tumor counts collected in different bins into solely one reference bin.

3) To test, optimize, validate and verify accuracy of these objectives. These will be performed by conducting experiments with the computerized 4D NCAT phantom and with the physical dynamic respiratory phantom.

Optimization is determined by comparing which integration/registration method produces the maximum correlation value between the number of counts of integrated and reference bins, requires less computation time and has a higher tolerance for noise.

Validation using computerized 4D NCAT phantom

Tumor volume and activity in computerized phantoms are the true and standard values to which to compare the result of calculations. The result of applying the algorithm must provide the equivalent activity and volume to those that are simulated. The robustness of the algorithm is tested by simulating tumors of different size and positions in the lung.

The minimum volume and tumor-to-background ratio that can be resolved as a lung tumor were determined.

Validation using a physical dynamic respiratory phantom

Data collection followed the same protocol commonly used for clinical studies. Three conditions were compared: the physical phantom simulating the respiratory motion for a) gated data collection, b) un-gated data collection, and c) data collection without tumor motion, this was used as a gold standard (true value) to be compared with results. Tumor variables to be controlled were: volume, total number of counts (activity), and maximum and average number of counts. These values will be considered the gold standard to which the results of the algorithm are compared.

3.2 Significance of the Study

One limitation of molecular imaging with ^{18}FDG-PET for detecting, identifying and quantifying small tumors (< 1 cm) is the artifacts created by respiratory motion [40, 73]. Compensation of respiratory motion in lung PET image is a current research issue [54, 55, 74] with broad impact on quantitation, diagnosis, accuracy, and clinical management of lung tumors. The major objectives of respiratory motion correction are to: 1) improve tumor detection by better identification of small tumors that move significantly during respiration, and 2) improve quantitation of lung tumors that move with respiration. The long term goal of this project is to improve radiation therapy by combining gated PET/CT information with gated beam irradiation.

This research project proposed to develop and validate a computer-assisted method that can automatically localize SPN in lung PET images of discrete bins within the breathing cycle, followed by the algorithm of integrating all the information of a complete

respiratory cycle into a single reference bin. In this way, the best compromise between short PET scan time and reduced image noise could be achieved. The automatic algorithm and practical procedure can be used in a busy clinical setting, making quantitation and clinical analysis more precise and faster.

All the developmental and research work of this project is oriented to the practical implementation of results into the clinical setting through the incorporation of software and hardware tools into commercial PET/CT systems.

4. RESEARCH DESIGN AND METHODS

4.1 Phantom Imaging

Experiments were conducted using a Lung-Chest phantom with simulated spherical lung tumors filled with ^{18}FDG. In this study the Elliptical Lung-Spine Body Phantom (Model ECT/LUNG/P) was used [75], which is a fully tissue equivalent anthropomorphic phantom, including large, body-shaped lungs, which can be filled with Styrofoam beads or air to simulate lung tissue density. This phantom is designed to evaluate quantitative imaging intended to be applied to humans using SPECT and PET and it allows investigating the effects of imaging systems under conditions very similar to those in a patient.

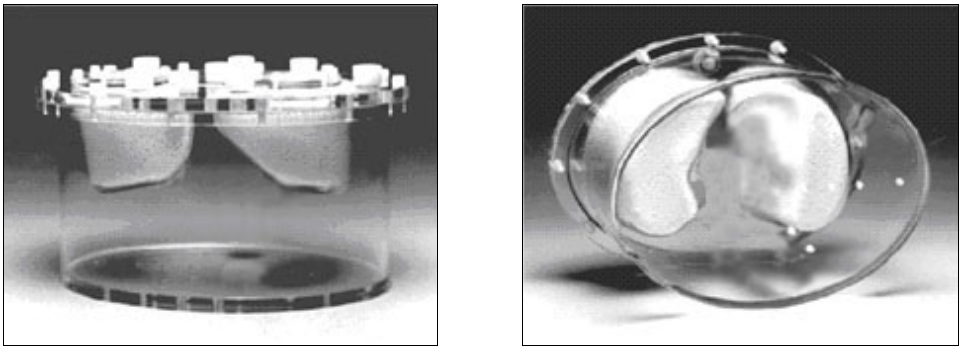

Figure 4.1 Elliptical Lung-Spine Body Phantom. On the left: the frontal view and on the right: the bottom view [75]. (Adapted from www.spect.com)

Compartment	Measured volume (liters)
Left lung (w/o Styrofoam beads)	0.9
Right lung (w/o Styrofoam beads)	1.1
Left lung (w/ Styrofoam beads)	0.36
Right lung (w/ Styrofoam beads)	0.44
Background (empty cylinder w/o inserts)	10.3
Cylinder with lung-spine insert	7.4

Table 4.1 Volumes of different compartments in phantom [75] (www.spect.com)

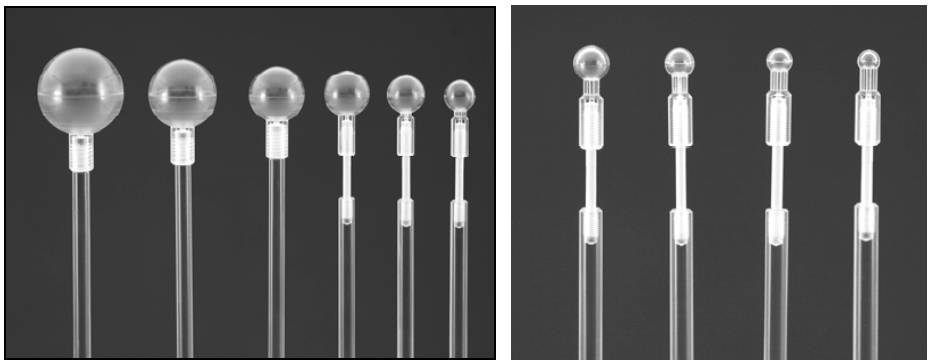

Figure 4.2 Left: Hollow Sphere Set (Model ECT/HS/SET6). Outer diameter: 33.27 mm, 26.82 mm, 21.79 mm, 17.69 mm, 14.43 mm, 11.89 mm. Spheres' volume: 16.0 mL, 8.0 mL, 4.0 mL, 2.0 mL, 1.0 mL, and 0.5 mL. Right: Micro Hollow Sphere Set Model ECT/MI-HS/SET4 Outer diameter: 5.94 mm, 6.95 mm, 8.23 mm, 9.86 mm. Spheres' volume: 31 μL, 63 μL, 125 μL, and 250 μL [75].

Phantom Experiment

One sphere representing a tumor was inserted into one of the lungs of the phantom after being filled with a predetermined amount of activity of ^{18}FDG. The movement of the sphere was driven by a stepper motor controlled by a PIC microcontroller that allows the user to select different tumor motion parameters, i.e., different frequency and different amplitude to simulate different respiratory periods and amplitudes [76]. Another stepper motor was used to simulate the motion of the chest. The simulated chest movement was monitored using Varian's Real-Time Position Management (RPM) (Varian Medical Systems, Palo Alto, CA) camera and RPM software generated the gating signals for the PET. The RPM camera is mounted at the end of the scanner table, and captures an infrared signal coming from a reflective block as described in Chapter 2.3.2. Detail parameters of the experiments can be found in Table 4.2.

Two concentrations of FDG were prepared. One concentration of FDG was first diluted into 1 liter water and then added to the hollow spheres to simulate tumor FDG concentration and another concentration of FDG was diluted into the phantom (10.3

Liter) to simulate background FDG concentration. In the experiments the body phantom was filled with approximately 0.11 *mCi/L* ^{18}FDG as background concentration and the sphere was filled with 0.7 *mCi/L* ^{18}FDG as tumor concentration, so the tumor to background ratio was approximately 6 to 1.

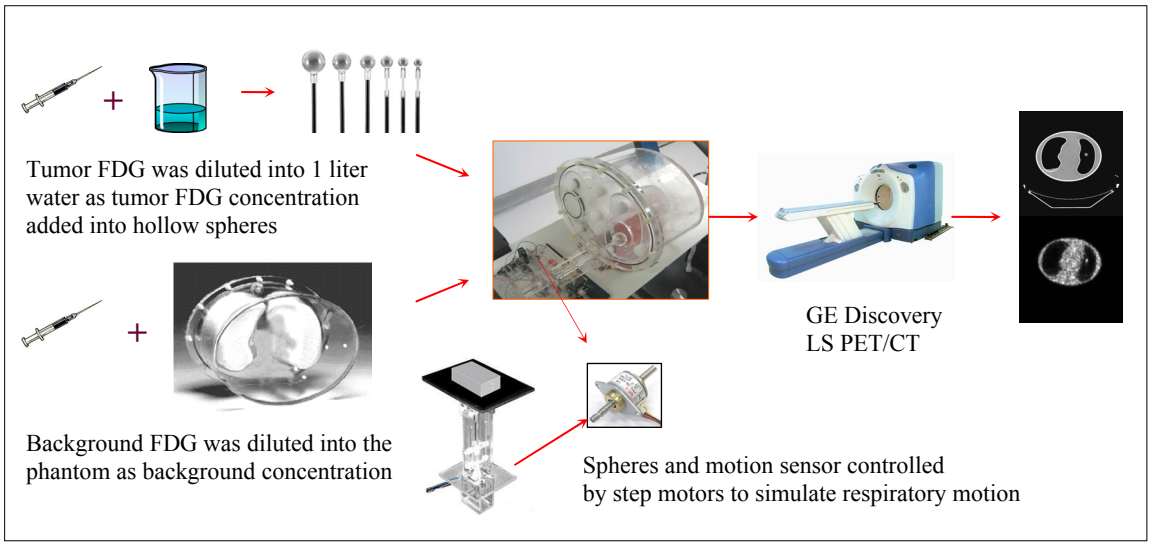

Figure 4.3 Diagram for physical phantom experiments. Tumor FDG was approximately 0.7 mCi/L in the hollow spheres to simulate tumor FDG concentration. Background FDG concentration was approximately 0.11 mCi/L to simulate background FDG concentration. Spheres simulating tumors were driven by a stepper motor controlled by a PIC microcontroller.

Sphere diameter (mm)	17.69, 14.43, 11.89, 9.86, 8.23
Sphere volume (ml)	2.00, 1.00, 0.50, 0.25, 0.13, 0.06
Sphere position	Left lung
Respiratory cycle (second)	4.0
Respiratory amplitude (mm)	20.0
Tumor/background ratio	(5.98, 6.35, 6.01, 5.80, 6.22) ≈ 6
Image Acquisition	Ungated & Static PET: 5.0 min Gated PET: 5.0 min for 10 gates

Table 4.2 Parameter settings in physical phantom experiments.

4.2 PET/CT Scans

All experiments with the dynamic physical phantom were done at Baptist Hospital of Miami using the Discovery LS PET/CT scan (GE Medical Systems) and Varian RPM Respiratory Gating System. This hybrid system incorporates the GE Light Speed multi-slice CT and the Advance Nxi PET scanner in the same instrument. Emission and transmission images are automatically registered and the CT map is used for attenuation correction of PET data. The images are acquired in the DICOM format, which is a standard file format used in storing and transferring medical data. The parameters for PET/CT configurations are shown in Table 4.3.

Discovery LS Advanced NXi PET Configuration	
Transverse field of view (mm)	550
Image dimension	128*128
Number of Image Planes	35
Slice Thickness (mm)	4.25
Mode	2D
Number of gates	10
Reconstruction Method	OSEM
Discovery LightSpeed multi-slice CT configuration	
Slice Thickness (mm)	5
Image dimension	512*512
Number of Image Planes	35
Acquisition mode	Snapshot CT (fast helical mode)
mA	90
KVP	140

Table 4.3 Selected parameters for Discovery LS PET/CT operation.

4.3 Develop Computerized Phantom

The 4D NCAT phantom is used to simulate different types of respiratory cycles, and to simulate PET/CT images with the tumor in different positions. The 4D NCAT phantom

has been developed for emission tomography studies. It integrates the anatomical data from the Visible Human dataset and the model of cardiac and respiratory motion to generate realistic and dynamic digital phantoms [9, 68-71].

By using the respiratory model of the NCAT phantom, 3D phantoms were generated at different times within the respiratory cycle as volume arrays of $128 \times 128 \times 128$ voxels, with pixel sizes and slice thickness equivalent to those obtained in clinical PET studies. Then, two sets of respiratory phantoms were created for each time bin. The first corresponds to a transmission phantom in which only soft tissue and lungs were differentiated. The value of the attenuation coefficient for lung at 511 keV (0.024 cm^{-1}) was assigned to lung voxels. The rest of the voxels had a value equal to the attenuation coefficient of soft tissue at 511 keV (0.097 cm^{-1}). The second set of phantoms represents the ^{18}FDG distribution in lung and other structures.

The parameters of the raw binary file simulated by 4D NCAT phantom are as following:

- Pixel width: 3.125 mm
- Lowest Image Pixel value: 0 (number of counts)
- Highest Image pixel value: 75 (number of counts)
- Rows: 128; Columns: 128

Lung tumors were simulated assuming a spherical shape. Different volume tumors were assessed (diameters of 6 mm, 8.5 mm, 10mm, 20 mm and 25 mm), with similar range of activities encountered in clinical studies. Tumor-to-background ratio was 2.5. The respiratory cycle period was 4.0 seconds with 8 equally spaced time frames. The detail parameters of the NCAT phantom experiments can be found in Table 4.4. Here the maximum amplitude of diaphragm motion during respiration was set to 20 mm and the

maximum amplitude of AP (anteroposterior diameter of the ribcage) expansion was 12 mm. These are normal values for normal tidal breathing [70, 71].

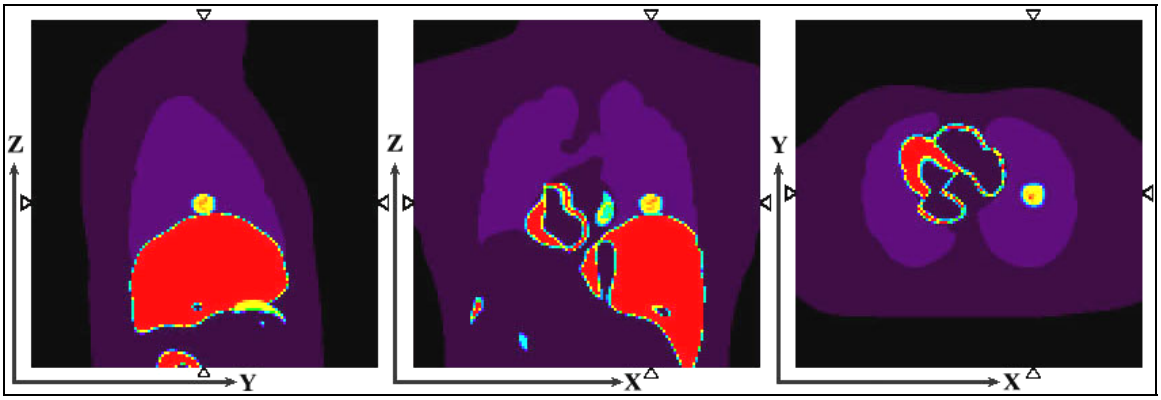

Figure 4.4 Sagittal, Coronal and Transverse view of the raw data simulated by NCAT including tumor file and torso file, before any noise is included, showing the direction of *X*, *Y*, *Z*. The motion of the tumor was modeled as two-way motion: *Y* and *Z*.

Sphere diameter (mm)	6.0, 8.5, 10.0*, 20.0, 25.0
Sphere position	Left lung
Respiratory cycle (second)	5.0
Respiratory amplitude (mm)	20.0
Tumor/background ratio	3.0

Table 4.4 Detail parameter settings of NCAT computer phantom experiments. * The experiments with 10.0 mm tumors (with Gaussian distributed noise) has been repeated three times to see if there are any statistic changes in the simulation.

4.3.1 Simulation with Gaussian Distributed Noise

The original NCAT phantom is noise free. To simulate practical data, two methods were implemented to add the noise to the original data. One is adding Gaussian distribution noise (Figure 4.5). The volume of the tumor was excluded from the lung region of interest in the studies with a tumor. By selecting regions of interest at different slices, the mean and standard deviation (*SD*) of counts could be determined for each structure of

interest (lung, soft tissue, liver). Simulated phantoms were created by assigning to the voxels *v(i)* of each structure the value:

$$v(i) = \frac{mean}{n} \pm \frac{RND(*) \times SD}{\sqrt{n}},$$

where mean is the average value of all the counts in each structure, $SD = \sqrt{mean}$, n is the number of time bins used to simulate respiration [40] and $RND(*)$ is a random number with Gaussian distribution (mean equal to zero and standard deviation equal to one).

Finally, the blurring effect due to the finite resolution of PET images was included by the convolution of each transaxial slice with a Gaussian filter in which the FWHM in the *X* and *Y* directions correspond to the transaxial resolution of a typical PET scan. The axial blurring was performed by the convolution of the images in the axial direction with a one-dimensional Gaussian filter. For FWHM in the *X*, *Y* and *Z* directions, the values of 5 mm was applied, which is the typical resolution of current PET scanners. In the NCAT phantom, data of pixel width = 3.125 mm, so the FWHM = 5/3.125 = 1.6 pixel was generated.

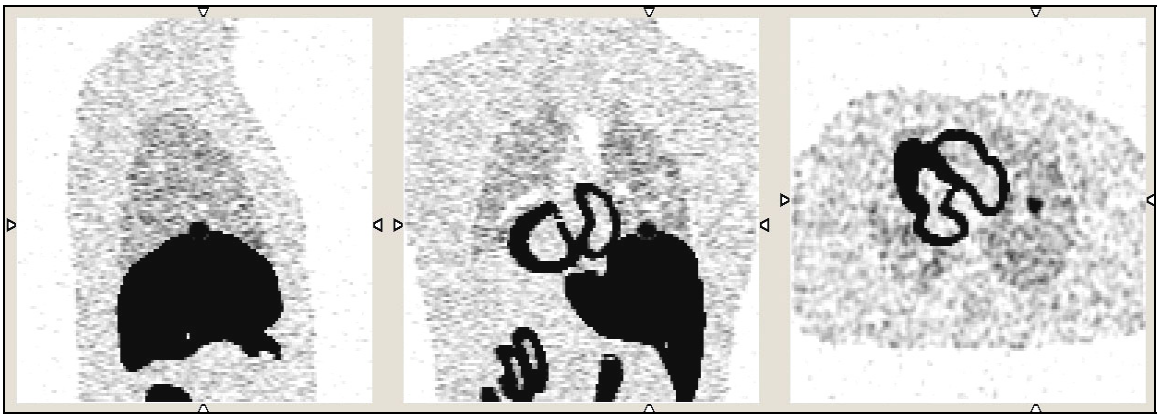

Figure 4.5 Simulated PET images from Figure 4.4 after applying noise by including Gaussian distributed noise and by including blurring effect.

4.3.2 Simulation with Poisson Distributed Noise

Another analytical method was implemented (Figure 4.6) using Matlab (The Mathworks, Natick, Massachusetts) to forward project the noise-free NCAT data to sonograms. Poisson distributed noise was added in the sonogram domain. And then the images were reconstructed with filtered-back-projection using Matlab's "iradon.m" routine [77]. Finally, the blurring effect due to the finite resolution of PET images was introduced by the convolution of each transaxial slice with a Point-spread-function with FWHM of 5 mm in the x and y directions, corresponding to the approximate resolution of the PET camera used. The axial blurring was performed by the convolution of the images in the axial direction with a one-dimensional Gaussian filter with 5 mm FWHM value.

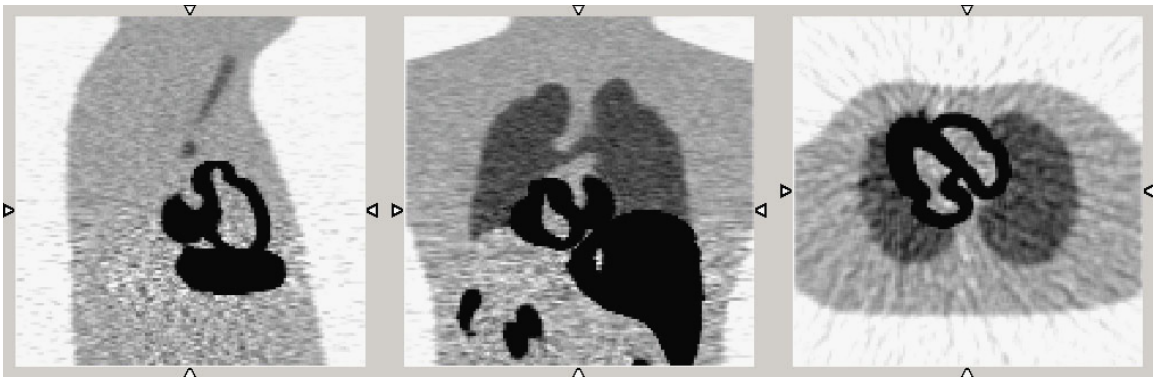

Figure 4.6 Simulated PET images from Figure 4.4 using analytical method to include Possion distributed noise and Point-spread-function.

4.4 Image Segmentation

GE's Discovery LS PET/CT system can produce high quality CT and PET images of the phantom in one study. These two image data sets are registered and fused to form a single data set that displays the anatomical and morphological information from CT along with the physiological information of PET. The set of DICOM files of PET and CT transaxial slices acquired from the hybrid PET/CT scanner were read into volume files. CT volume

files are used to segment lungs and PET volume files are used to identify the tumors and quantitate their activity.

All the code software for processing these images and calculating the parameters has been developed using the Interactive Data language (IDL), Research Systems, Inc. (Boulder, CO). IDL is a matrix-oriented interpreter language designed specifically for processing large and complex datasets. It can create powerful visualizations easily and quickly, including simple 2D plots and 3D graphic displays. IDL includes a rich library of proven image processing and signal processing routines to help analyze the data. Data access in IDL is flexible. It has built-in support for a wide variety of general file formats, including raw binary files, BMP, TIFF, JPEG and DICOM images.

4.4.1 CT Image Processing

Image Filtering

Since identifying lung tumors in PET images is the main objective of this research, and CT images are used only to define the lung region, the analysis of CT images was performed in a matrix size of 128 × 128 pixels. To remove the background and patient table from the image, the body was segmented by a threshold analysis on low resolution CT scans. Low resolution images were obtained by decomposing CT scans into five resolution levels using a wavelet analysis/synthesis filter bank based on the 2D Frazier-Javerth transform [13] derived by Laine et al. [78]. These filters are isotropic, orthonormal and can provide a perfect reconstruction. Furthermore in this model the analysis and synthesis of these filters are the same and relatively easy to implement for computer calculations. The following equations are the analysis filter functions in the

frequency domain for an L-level multi-resolution decomposition [78]. Here it is equivalent for the analysis and synthesis of the filters ($[F_i(v) = F_i^{-1}(v)]$).

For $2 \le i \le L-1$:

$$F_i(n) = \begin{cases} \left[0.5 \times \left(1 - \cos(p \log_2(2^{i-2} n / n_N))\right)\right]^{1/2} & \text{for } 2^{-i} n < n < 2^{-(i-2)} n_N \\ 0 & \text{otherwise} \end{cases};$$

For $i = 1$:

$$F_i(n) = \begin{cases} \left[1 - (F_2(n))^2\right]^{1/2} & \text{for } 2^{-1} n_N < n < n_N \\ 0 & \text{otherwise} \end{cases};$$

For $i = L$:

$$F_i(n) = \begin{cases} \left[1 - (F_{L-1}(n))^2\right]^{1/2} & \text{for } 0 < n < 2^{-(L-2)} n_N \\ 0 & \text{otherwise} \end{cases};$$

where $\boldsymbol{n}$ is the radial frequency and $\boldsymbol{n_N}$ is the Nyquist frequency of the projection.

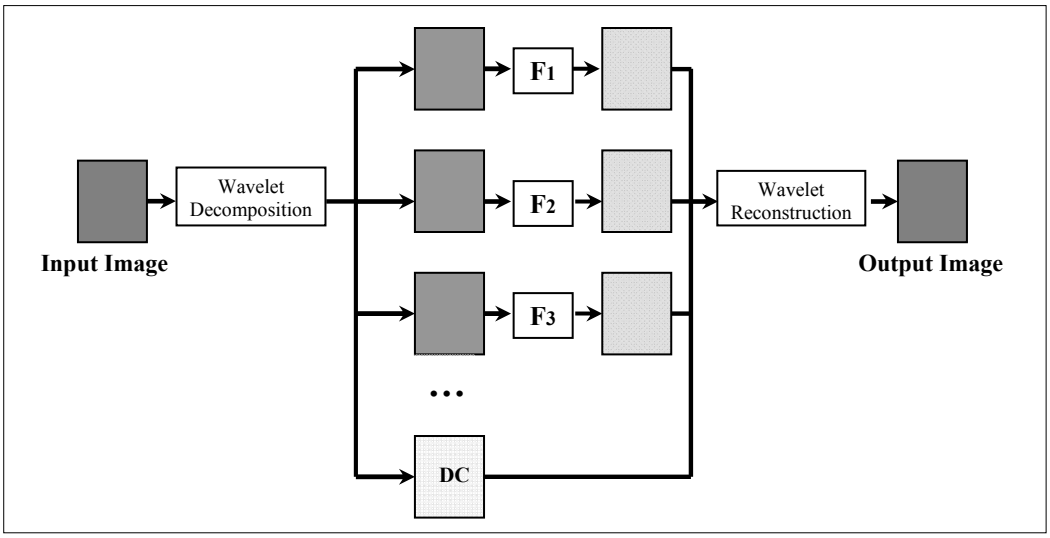

Figure 4.7 Framework of multi resolution analysis using discrete wavelet transforms. Here three level decompositions are shown.

Multi-resolution analysis decomposes an image into a coarse approximation and the image details for consecutive higher frequency bands or spatial resolutions. It was demonstrated by Mallat [8] that multi-resolution representations could be acquired by decomposing an image into orthogonal wavelet basis as shown in Figure 4.9. Multi-resolution wavelet representation provides orthonormal bases whose components have

good localization properties in both spatial and frequency domains. The following figure graphically shows the two dimensional analysis and synthesis functions in the frequency domain.

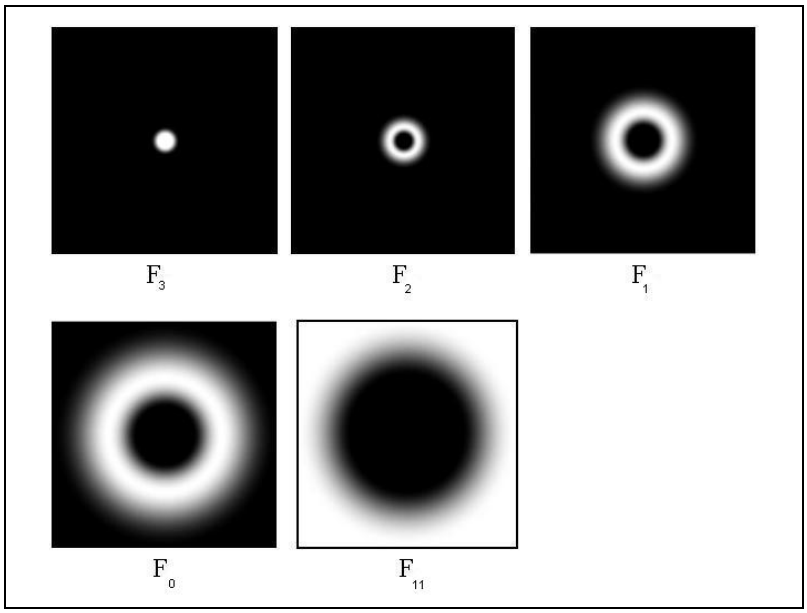

Figure 4.8 Analysis and synthesis functions (F_j=S_j) for five resolution levels shown in frequency domain.

After applying the multi-resolution filters, the threshold definition for segmentation is more reproducible and constant than the original CT images, as the CT (Hounsfield unit) number varies because of the calibration of different CT scanners and other characteristics of the x-ray beams. This is why it is not reliable to select only one constant threshold for segmenting CT images [13]. Segmentation on low resolution CT images makes the threshold selection easier and more robust than the original CT images.

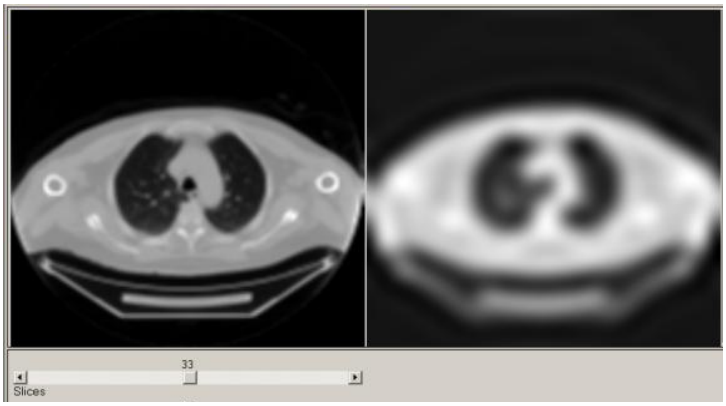

Figure 4.9 Original CT slice and its corresponding third resolution level derived from one analysis/synthesis filter bank based on the 2D Frazier-Javerth transform. The low resolution image is used to segment the body by defining a threshold.

Lung Segmentation

The algorithms to segment the tissue from the background are based on the continuity or discontinuity of the intensity values. Edge detection is based on continuity while region labeling and histogram thresholding are based on similarity and discontinuity measures. The CT image, which is characterized by two dominant modes (i.e. tissue and background), result in a bimodal histogram. In such a case, basic global thresholding which partitions the histogram of the image using a single global threshold "T" accurately differentiates body from background. The segmentation is accomplished by scanning the image pixel by pixel and labeling each pixel as object or background, depending on whether the gray level of that pixel is greater or less that the value of T. The success of this method depends on how well the histogram can be partitioned [79]. The algorithm of the thresholding is given in the steps listed below:

a) An initial estimate for the threshold (T) is selected to be midway between the maximum and minimum gray levels.

b) The image is then segmented using the global threshold T. Two groups of pixels will be created: *G1* consisting of all pixels with gray level values > *T* and *G2* consisting of pixels with values $\leq T$.

c) The mean gray level values μ_1 and μ_2 are calculated for the pixels in regions *G1* and *G2*.

d) The new threshold T is equal to the following value: $T = (\mu_1 + \mu_2)/2$.

e) Repeat steps b through d until the difference in *T* in successive iterations is smaller than a predefined parameter T_0.

Binary images of the CT volume slices were obtained by assigning zero to pixels below the threshold and one to pixels above the threshold. After segmenting the image using the global threshold, only body and background were retained in the binary templates. This was done by labeling the volume into different regions and blanking out all small regions except the two major regions, the body and the background. The function "label region" (IDL routine function) did the region labeling and sorted the regions in descending order of their size. Any tumors present in the lung were also blanked out during this process.

The lung regions in the resulting binary templates were closed (their pixel value was made equal to that of the tissue) to obtain binary templates of the entire extent of body region in the CT slices. Using these binary templates an iterative threshold to segment the lungs was again calculated, considering only the pixels that fall in the body region. After obtaining the extent of the body region in the images, it is important to determine the range of CT slices in which the lungs are present. This reduces the load of image processing and also allows accurate segmentation of lung regions.

To find the limits for the appearance and disappearance of lungs in the volume file of CT images, the count of total number of pixels, which are less than the threshold and belonging to lungs, was determined for each slice in the volume file. A plot of these counts vs. slices resulted in a peak where the lungs appear in the volume file. In order to find the inflection points, the curve was first smoothed by fitting a polynomial to the curve and finding its differential. The inflection point at which the peak starts signified the slice at which the lungs start appearing and the inflection point at which the peak ends signified the slice at which the lungs start disappearing. For all further image processing purposes only the slices containing the lungs were considered.

The lungs regions were extracted by applying the binary templates with closed lung region and the binary templates without closing the lung regions over the volume file of the original CT images. The iterative threshold determined for lung segmentation was applied to the extracted lung regions to obtain accurately segmented lung regions. The binary images of these lung regions cover the entire lung volume without distinguishing the tumor.

Determination of Background

The binary templates of CT slices without region labeling (in order to preserve the tumor region) and the binary templates with closed lung region were applied together to the original CT slices. This resulted in segmented lung regions which excluded the tumor regions. These masks of segmented lung slices excluding the tumors were applied on the PET images to calculate the average background activity. The flow diagram shown below explains the algorithm in further detail.

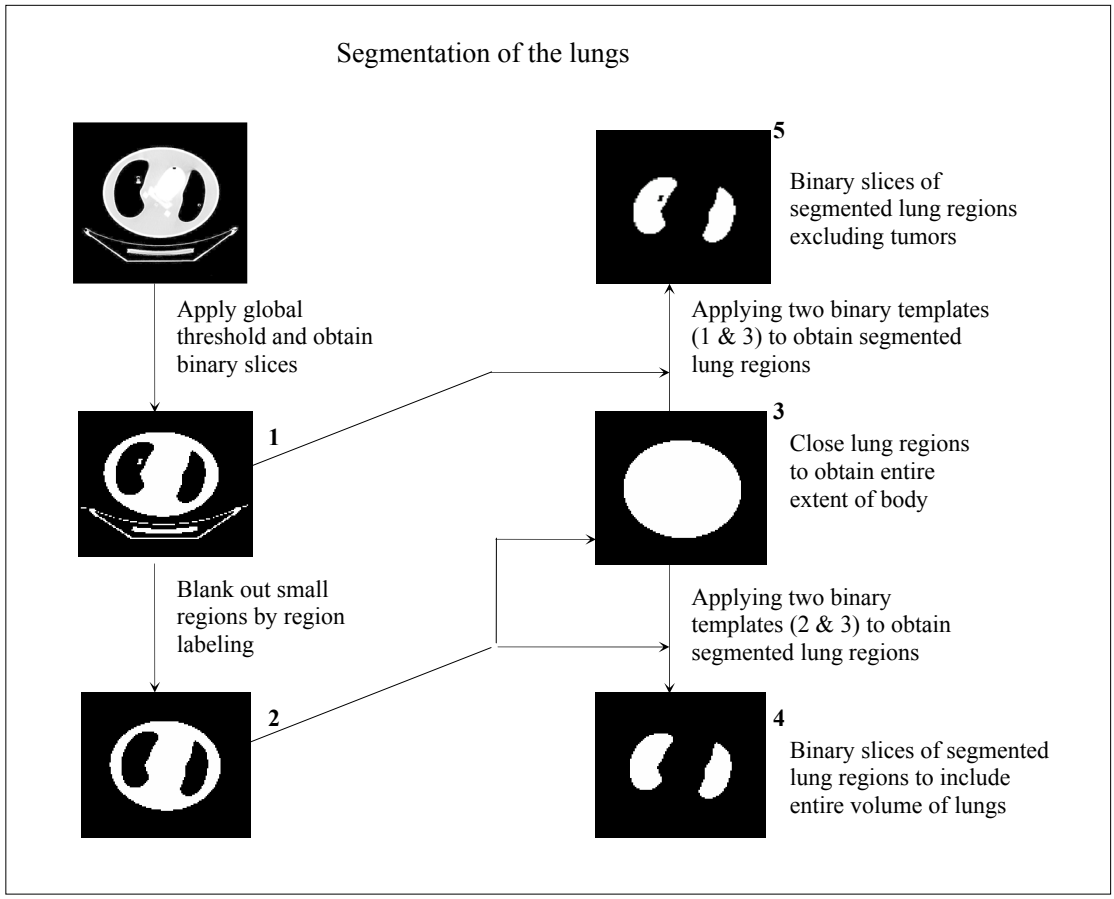

Figure 4.10 Flow diagram for CT volume image processing

4.4.2 Identification of PET Tumors

Segmenting Lung Regions in PET Images

The binary templates determined from the CT analysis were used to define the volume to search for the tumors in the electronically registered PET images. The CT binary templates were dilated by 3 pixels to account for the scatter of activity in PET images. The lung regions in PET images were segmented using these dilated binary templates of segmented lung CT regions.

Calculation of Background Intensity

Binary templates of segmented lung CT regions excluding the tumor (lung CT background) were used to define the background region in lung PET images. However

the PET tumors have spilled out activity around the tumor borders and result in a magnification of apparent tumor size. So the binary templates of lung CT background images were eroded further to exclude the entire tumor activity. The number of pixels needed to be eroded in order to remove the entire tumor and its spilled out activity was determined by comparing average background intensities with the number of pixels retained in the eroded lung region.

The eroded binary lung CT regions were used to extract the background lung regions of PET images. The average background intensity in PET images was found by taking an average of all the pixels in the PET lung volume excluding the tumor or tumors. The standard deviation of these pixels was also found. The background intensity was determined as the total of average background intensity and three times the standard deviation between the pixels.

Region Growing by Pixel Aggregation

Region growing is a procedure that groups pixels or sub-regions into larger regions. The simplest of these approaches is pixel aggregation, which starts with a set of "seed" points and from these grows regions by expanding to those neighboring pixels that have similar properties. Another problem in region growing is the formulation of a stopping rule. When no more pixels meet with the criteria to be grouped in that region, the growing region stops [80].

In order to identify the tumors, first the maximum counts voxel was found in the 3D volume. This became the seed voxel that was used in a region growing algorithm to define the three dimensional extension of the tumor. The stopping criteria for the region growth was the average background intensity + three times the standard deviation

between the pixels (average + 3*SD) of eroded lung regions of PET images. Another stopping criteria was also evaluated, by initially using 40% of the maximum counts, and then using the iterative thresholding method to find the optimal stop criterion of the region growing algorithm. “Search3D”, a user-defined function written in IDL is called to perform the region growth.

Voxels included in the tumor were defined as those connected with a number of counts higher than the background intensity of the lung regions in PET images. After determining the tumor volume, the total number of counts, volume and list of voxel coordinates with their corresponding number of counts, was saved into a text file. In cases there are more than one tumor, the first segmented tumor was “erased” from the PET images under analysis by replacing the number of counts of each voxel with the average lung background. After that, the search of a second local maximum was started again. The algorithm stopped searching for any new tumors if the new local maximum value was below 40% of the original maximum counts. The entire flow chart of this process can be viewed in Figure 4.10 below. The final output of the automatic localization algorithm was a binary file with the voxel coordinates and number of counts of each voxel for each respiratory time bin. This was the basic information that would be used in the registration/integration algorithm.

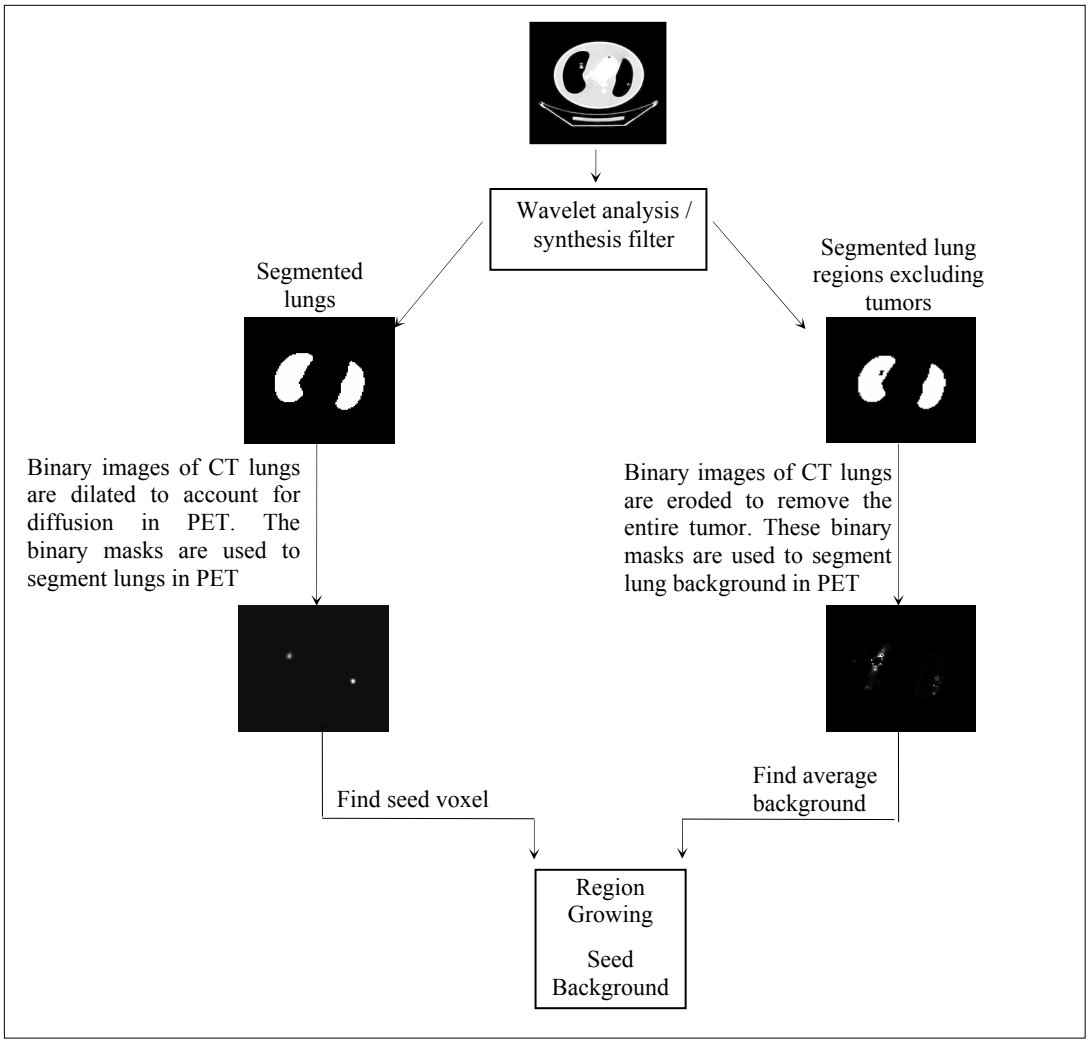

Figure 4.11 Flow diagram describing the detection of tumors

4.5 Motion Track and Registration Schemes

The basic idea is that, given a moved volume V_i at the bin i and a corresponding reference volume V_0 at the reference time bin, find a registration such that the registered volume $R[V_i]$ matches as well as possible the reference volume V_0. Since the number of voxels involved in each tumor is relatively small and all the voxels are compacted around a maximum value, only simple matching methods were considered. There are two integration schemes used in this work, one is to register directly the target bin to the reference bin as shown in Figure 4.14 left, and the other is to register each bin one by one

as shown in Figure 4.14 right. Assume *2n* is the total number of bins, the computational complexity for Direct Scheme is (*2n-1*) registrations and one addition while the computational complexity for Successive Scheme is *n*n* registrations and one addition (if the n^{th} bin is select as the reference bin), so the Successive process requires more computation time. For the Successive Scheme, the discrepancy between each bin is less compared to the Direct Scheme, which could reduce the error while calculating the registration matrix. However, it requires more interpolation steps and thus could blur the resulting image and increase the computational cost.

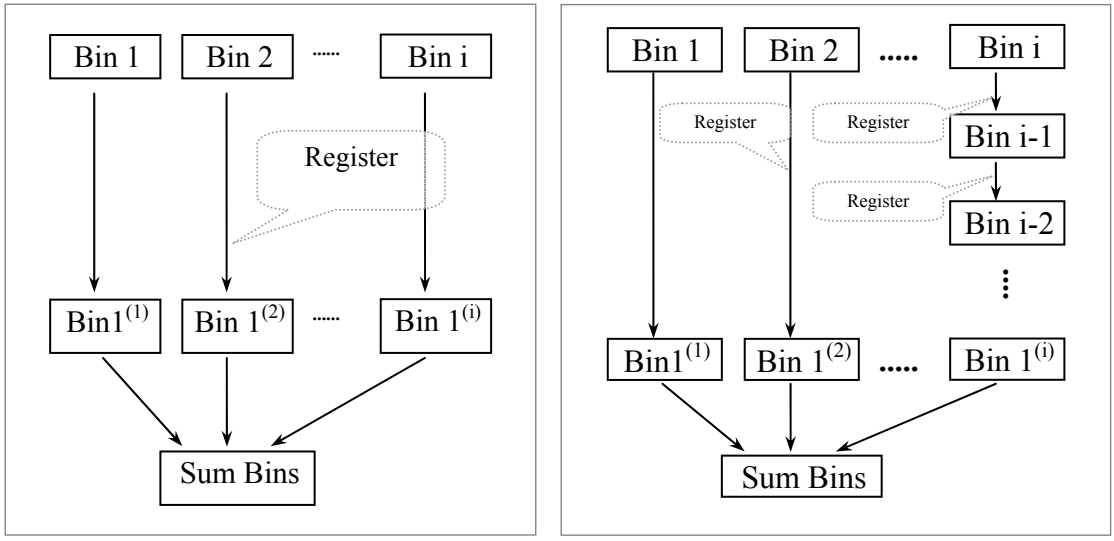

Figure 4.12 The process flow of two registration/integration schemes. On the left is the Direct Scheme and on the right is the Successive Scheme.

In order to reduce the radiation dose delivered to the patient, the snapshot CT was used instead of 4D CT. This could create the problem of a mismatch between the CT image and each gated PET image. To choose the "best" bin as the reference bin, the cross correlation values between segmented CT tumor and each gated PET tumors were evaluated so that the best match bin (with the highest correlation value) can be selected as the reference bin.

4.5.1 Noise before Correction vs. Noise after Correction

Ideally, the voxel value in a reconstructed nuclear medicine image indicates the underlying radioactive decay activity in each voxel. In real images these voxel values are subject to image noise, which is the degree of variation of pixel values caused by the statistical nature of the detection process, reconstruction algorithm limitations, and radiotracer activity itself. The precise form of such noise depends on many factors, in nuclear medicine images the counting noise is Poisson noise, so that the pixel noise variance is equal to the mean number of counts expected in a given region of the image. The standard deviation is the square-root of the mean number of counts.

The following equation assumes a simple voxel-by-voxel based model to simulate a realistic image by superimposing noise onto the original image.

real_I(x, y, z) = I(x, y, z) + g(0; I(x, y, z))

where the noise *g(0; I(x, y, z))* tends toward a Gaussian distribution with mean $\mu = 0$ and standard deviation $\delta = \sqrt{I(x,y,z)}$, *I(x, y, z)* is the number of radiotracer activities.

Before gating, we have signal *S* after time *T* in a particular region, where the standard deviation of the noise in this region is $\delta = \sqrt{S}$. After gating the signal *S* was divided into short time frames Δt_i, where $\sum(\Delta t_i) = T$, to generate signals and noise deviations at each time bin:

$$S_i = (\frac{\Delta t_i}{T})S,\ \delta_i = \sqrt{\frac{\Delta t_i}{T}}\delta$$

Since $\frac{\Delta t_i}{T} < 1$, in each gated bin, Signal-to-Noise Ratio (SNR) = $\frac{S_i}{\delta_i}$ < original SNR in ungated images = $\frac{S}{\delta}$

When the gated image bins are combined/registered together, $S_{\Sigma} \equiv \sum Si = S$, the standard deviation of the noise adds quadratically:

$$\delta_{\Sigma} = \sqrt{\sum \delta_i} = \sqrt{\sum (\frac{\Delta t_i}{T} \delta^2)} = \delta$$

This shows that after registration restore the SNR can be restored to the ungated scenario without prolonging the total PET acquisition time.

4.5.2 Intensity Based Registration

This method takes into account voxel values. The voxel with the maximum number of counts at V_i was registered with the voxel with the maximum number of counts at V_0. The same was performed for the second maximum and subsequent voxels. This is done by sorting all the voxels inside the tumor in descending order after segmenting the tumor and adding them one by one. The main inconvenience of this procedure is that V_i and V_0 include different number of voxels. Since respiratory motion is a continuous process, PET lung tumors within a discrete time bin can be blurred. In this case, some deformation in the extended volume is needed. One deformation that can be assessed is the compression of the peripheral voxels into the volume. That is to shrink the volume of the tumor by adding the peripheral pixels to their neighbors with lower counts. The shrinking process starts with those voxels of lowest activity. This process is applied previous to any other registration approach.

4.5.3 Centroid Based Registration

The centroid of each tumor volume was calculated from:

$$c(x, y, z) = \frac{\sum w_i a(x, y, z)}{\sum w_i}$$

where a is the x, y, or z coordinate of the *i-th* voxel and w_i is the number of counts. The motion vector calculated from the 3D distance between the two centroids determines the motion vector (dx, dy, dz) that moves voxels in V_i to V_o:

$$V_i(x+dx, y+dy, z+dz) = V_0(x, y, z)$$

The registered bins were evaluated with reference to the non-registered bins using the correlation coefficient. The correlation coefficient is defined as:

$$\text{correlation} = \frac{\sum_i [(V_{i0}(x,y,z) - u) \times (V_0(x,y,z) - v)]}{\sqrt{\sum_i (V_{i0}(x,y,z) - u)^2} \times \sqrt{\sum_i (V_0(x,y,z) - v)^2}}$$

Where $V_{i0}(x, y, z)$ and $V_i(x, y, z)$ are the values from two datasets in the comparison and u, v are the mean values from the same.

4.5.4 Optical Flow Based Registration

Optical flow is a concept for estimating the motion vector of each pixel in a digital image sequence [81], typically it is represented by vectors originating or terminating at pixels. Optical flow methods try to determine the motion between two image frames which are taken at times t and $t + \delta t$ at each pixel position. The method relied on two assumptions: (1) that corresponding pixels have constant grey values in the two images, and (2) that nearby points move in a similar manner.

In the following discussion, x, y and z are the coordinates of the 3D PET data set, and t represents the index of the bins. Let a PET data set be denoted as $f(x, y, z, t)$, where f is the grayscale intensity at position (x, y, z) at time t. After time δt, the corresponding position shifts to $(x + \delta x, y + \delta y, z + \delta z)$ and the function $f(x + \delta x, y + \delta y, z + \delta z, t + \delta t)$ can be expressed in a [82] series expansion as:

$$f(x+\delta x, y+\delta y, z+\delta z, t+\delta t)$$
$$= f(x,y,z,t) + \frac{\partial f(x,y,z,t)}{\partial x}\delta x + \frac{\partial f(x,y,z,t)}{\partial y}\delta y + \frac{\partial f(x,y,z,t)}{\partial z}\delta z + \frac{\partial f(x,y,z,t)}{\partial t}\delta t + H.O.T$$

where *H.O.T represent* second and higher order terms.

The first assumption that corresponding pixels have constant intensities yields: $f(x+\delta x, y+\delta y, z+\delta z, t+\delta t) = f(x,y,z,t)$. The second and higher-order terms in the equation can be ignored. Combining two equations and neglecting higher-order terms yields:

$\frac{\partial f}{\partial x}\delta x + \frac{\partial f}{\partial y}\delta y + \frac{\partial f}{\partial z}\delta z + \frac{\partial f}{\partial t}\delta t = 0$, or $\frac{\partial f}{\partial x}\frac{\delta x}{\delta t} + \frac{\partial f}{\partial y}\frac{\delta y}{\delta t} + \frac{\partial f}{\partial z}\frac{\delta z}{\delta t} + \frac{\partial f}{\partial t}\frac{\delta t}{\delta t} = 0$,

which results in the "optical flow equation": $\frac{\partial f}{\partial x}V_x + \frac{\partial f}{\partial y}V_y + \frac{\partial f}{\partial z}V_z + \frac{\partial f}{\partial t} = 0$

where V_x, V_y, V_z are the x, y and z components of the velocity or optical flow of $f(x,y,z,t)$ and $\frac{\partial f}{\partial x}$, $\frac{\partial f}{\partial y}$, $\frac{\partial f}{\partial z}$ and $\frac{\partial f}{\partial t}$ are the derivatives of the image at (x,y,z,t) in the corresponding directions. The derivatives of f_x, f_y, f_z and f_t are as follows:

Thus: $f_x V_x + f_y V_y + f_z V_z + f_t = 0$, or $\nabla f \cdot \vec{V} = -f_t$.

This is an equation in three unknowns. To solve this equation an additional constraint is needed.

Lucas-Kanade Method

The solution as given by Lucas and Kanade [83, 84] is a non-iterative method which assumes a locally constant flow. Assuming that the flow V_x, V_y, V_z is constant in a small window of size $m \times m \times m$ with $m > 1$ which is centered at voxel (x,y,z) and numbering the pixels as $1...n$ results in a set of equations:

$$f_{x_1}V_x + f_{y_1}V_y + f_{z_1}V_z = -f_{t_1}$$
$$f_{x_2}V_{x_2} + f_{y_2}V_y + f_{z_2}V_z = -f_{t_2}$$
$$\vdots$$
$$f_{x_n}V_{x_n} + f_{y_n}V_y + f_{z_n}V_z = -f_{t_n}$$

This system results in more than three equations for the three unknowns and thus an over-determined system:

$$\begin{bmatrix} f_{x_1} & f_{y_1} & f_{z_1} \\ f_{x_2} & f_{y_2} & f_{z_2} \\ \vdots & \vdots & \vdots \\ f_{x_n} & f_{y_n} & f_{z_n} \end{bmatrix} \begin{bmatrix} V_x \\ V_y \\ V_z \end{bmatrix} = \begin{bmatrix} -f_{t_1} \\ -f_{t_2} \\ \vdots \\ -f_{t_n} \end{bmatrix} \text{ or } A\vec{v} = -b$$

To solve the over-determined system of equations the least squares method is used:

$$A^T A\vec{v} = A^T(-b) \text{ or } \vec{v} = \left(A^T A\right)^{-1} A^T(-b)$$

$$\text{or } \begin{bmatrix} V_x \\ V_y \\ V_z \end{bmatrix} = \begin{bmatrix} \Sigma f_{x_i}^2 & \Sigma f_{x_i} f_{y_i} & \Sigma f_{x_i} f_{z_i} \\ \Sigma f_{x_i} f_{y_i} & \Sigma f_{y_i}^2 & \Sigma f_{y_i} f_{z_i} \\ \Sigma f_{x_i} f_{z_i} & \Sigma f_{y_i} f_{z_i} & \Sigma f_{z_i}^2 \end{bmatrix}^{-1} \begin{bmatrix} -\sum f_{x_i} f_{t_i} \\ -\sum f_{y_i} f_{t_i} \\ -\sum f_{z_i} f_{t_i} \end{bmatrix}$$

Thus the optical flow can be determined by computing the derivatives of the image in all four dimensions: x, y, z and t.

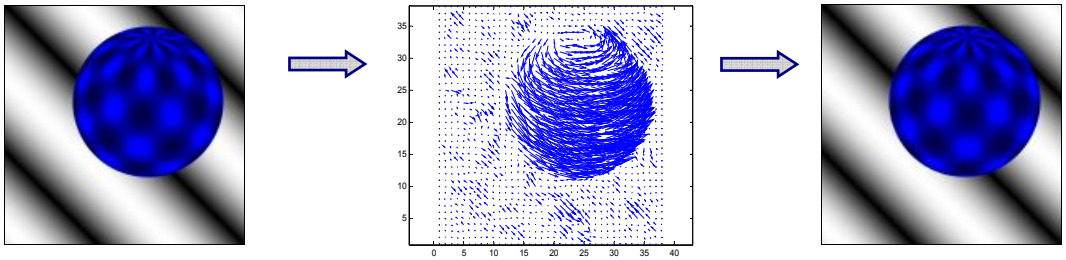

Figure 4.13 One example illustrating the optical flow method. The sphere is rotating from left to right, in the center is the generated optical flow field.

Horn-Schunck method

Another iterative solution used in this project is the Horn-Schunck method [85]. The Horn-Schunck method combines the gradient constraint with a global smoothness term to constrain the estimate velocity field $V = (V_x, V_y, V_z)$, minimizing:

$$\sum_R \left(I_x V_x + I_y V_y + I_z V_z + I_x\right) + \alpha^2 \left[\left(\frac{\delta V_x}{\delta x}\right)^2 + \left(\frac{\delta V_x}{\delta y}\right)^2 + \left(\frac{\delta V_x}{\delta z}\right)^2 + \left(\frac{\delta V_y}{\delta x}\right)^2 + \left(\frac{\delta V_y}{\delta y}\right)^2 + \left(\frac{\delta V_y}{\delta z}\right)^2 + \left(\frac{\delta V_z}{\delta x}\right)^2 + \left(\frac{\delta V_z}{\delta y}\right)^2 + \left(\frac{\delta V_z}{\delta z}\right)^2 \right]$$

where I_x, I_y, I_z are the derivatives of the image intensity values along the X, Y and Z dimensions, I_t is the derivative in the t (time-) direction, $V_x = dx/dt$, $V_y = dy/dt$, $V_z = dz/dt$ is the optical flow vector in X, Y and Z directions, which describe the spatial change rate of the voxel with respect to time. The parameter α is a regularization constant, larger values of α lead to a smoother flow. This function can be solved by calculating the Euler-Lagrange equations corresponding to the solution of the above equation. These are given as follows:

$$\Delta V_x - \frac{1}{\alpha} I_x \left(I_x V_x + I_y V_y + I_z V_z + I_t\right) = 0,$$
$$\Delta V_y - \frac{1}{\alpha} I_y \left(I_x V_x + I_y V_y + I_z V_z + I_t\right) = 0,$$
$$\Delta V_z - \frac{1}{\alpha} I_z \left(I_x V_x + I_y V_y + I_z V_z + I_t\right) = 0.$$

Solving these equations with Gauss-Seidel for the flow components V_x, V_y, V_z gives an iterative scheme:

$$V_x^{(k+1)} = V_x^{(k)} - I_x \cdot \frac{\left(I_x V_x^{(k)} + I_y V_y^{(k)} + I_z V_z^{(k)} + I_t\right)}{\left(\alpha^2 + I_x^{\,2} + I_y^{\,2} + I_z^{\,2}\right)},$$

$$V_y^{(k+1)} = V_y^{(k)} - I_y \cdot \frac{\left(I_x V_x^{(k)} + I_y V_y^{(k)} + I_z V_z^{(k)} + I_t\right)}{\left(\alpha^2 + I_x{}^2 + I_y{}^2 + I_z{}^2\right)},$$

$$V_z^{(k+1)} = V_z^{(k)} - I_z \cdot \frac{\left(I_x V_x^{(k)} + I_y V_y^{(k)} + I_z V_z^{(k)} + I_t\right)}{\left(\alpha^2 + I_x{}^2 + I_y{}^2 + I_z{}^2\right)},$$

where the superscript *k+1* denotes the next iteration, which is to be calculated and *k* is the last calculated result.

Multi-Resolution Algorithm

The limitation of the optical flow algorithm is that it becomes inaccurate in calculating the deformations with increasing movement (greater than 1 voxel difference). Thus it is necessary to extend the algorithm to accommodate larger displacements by implementing a Multi-Resolution algorithm [65, 73]. With a larger voxel size at a lower resolution, the magnitude of the displacement between two image sets decreases. Using a 2D image for example: two images each contain 512×512 pixels with resolution of 1×1 mm per pixel, a displacement of 4 mm in the lateral direction for a given region in the two images is therefore represented by 4 pixels at the given resolution level. After reducing the image size to 256×256 pixels, the resolution becomes 2×2 mm per pixel. The 4 mm displacement is now represented by 2 pixels. At a resolution of 4×4 mm per pixel (128×128 pixels per image), the displacement becomes only 1 pixel. If the optical flow program is used to estimate the two images, the resulting motion field can be very accurate in a short calculation time. After this calculation at a coarse resolution level, linear interpolation is used to expand the resulting 128×128 displacement matrix to 256×256. The optical flow program resumes the calculation at the 256×256 resolution level, starting with the expanded matrix representing the corrected and expanded images. The initial displacement at this resolution level is within 1 pixel instead of 2 pixels if the

lower-level registration is lacking. This procedure continues until the finest resolution level is completed as shown in Figure 4.16. In this example, the initial displacement at the finest resolution is within 1 pixel after the pre-calculation at coarser levels. The estimation with a multi-resolution feature is much more accurate and converges to the solution much faster.

The multi-resolution feature implemented in this project was 3D, and thus it can start with fewer CT slices. The registration starts at a user-specified resolution level that is a $2^{n\text{th}}$ multiple multiple of the original resolution and increases hierarchically until the finest resolution is achieved. Figure 4.16 shows a flow chart of the multi-resolution feature. For the NCAT phantom data, the dimension was reduced from 128×128×128 to 64×64×64 and then to 32×32×32, for the physical phantom data, the dimension was reduced from 128×128×36 to 64×64×18 and then to 32×32×9. Further reduction of the image dimension was not meaningful for image resolution lower than 32×32×32 or 32×32×9. The initial $V_x^{(0)}$, $V_y^{(0)}$ and $V_z^{(0)}$ were set to 0, and the value of α was set at 5. Bin 4 was chosen as reference bin, iteration number was set to 50 for the first resolution lever, and less iteration were required as the resolution level increased.

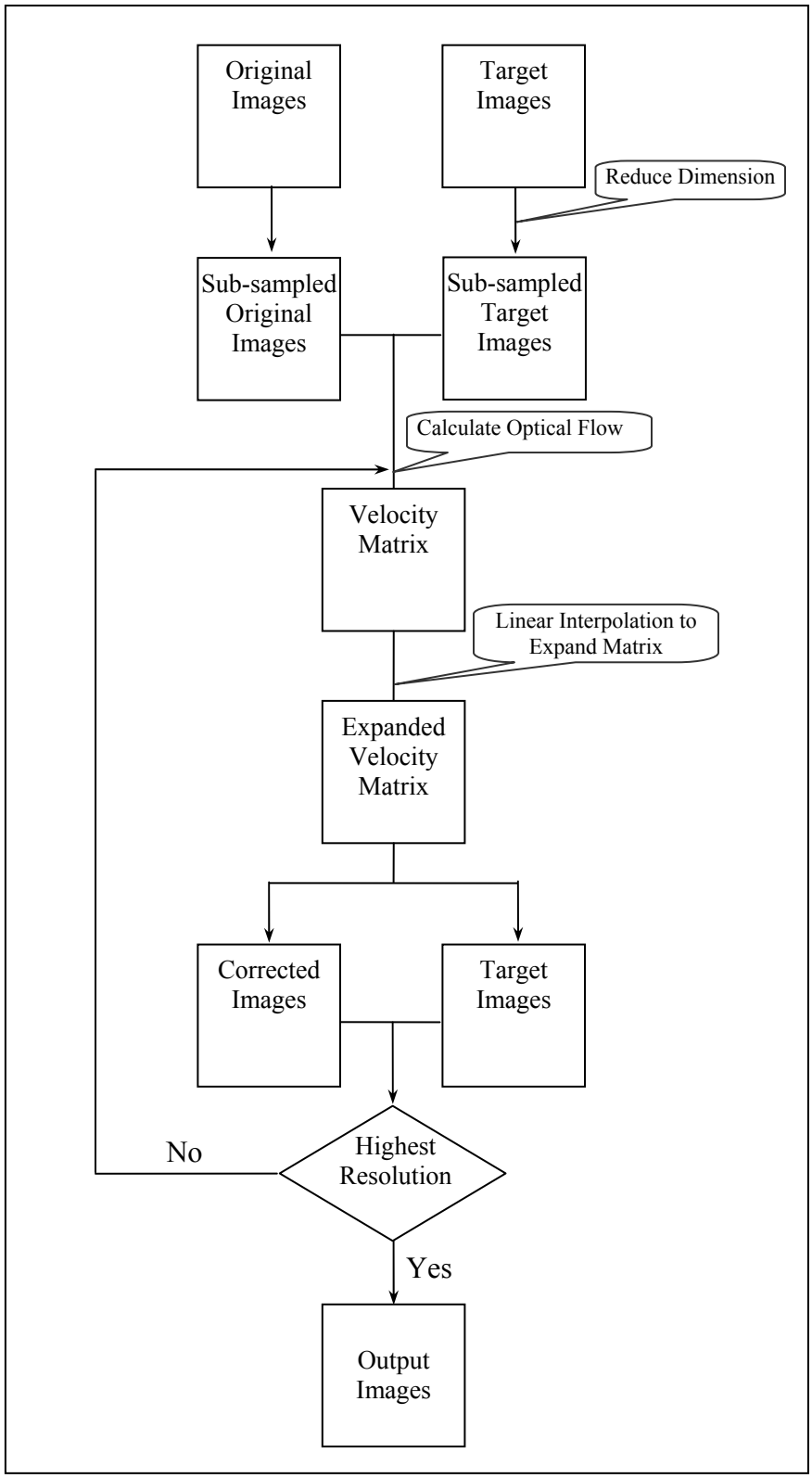

Figure 4.14 Flow chart of Multi-resolution algorithm used in estimating optical flow between two image data sets.

4.5.5 Rigid Body Registration

In this project, 3D rigid body registration was modeled as rotations around and translations along each of the three major coordinate axes (X, Y, Z), and scaling. For each point (x_1, y_1, z_1) in a data set, an affine mapping is defined into the co-ordinates of another space (y_1, y_2, y_3) [86], expressed as:

$$\begin{aligned} y_1 &= m_{11}x_1 + m_{12}x_2 + m_{13}x_3 + m_{14} \\ y_2 &= m_{21}x_1 + m_{22}x_2 + m_{23}x_3 + m_{24} \\ y_1 &= m_{31}x_1 + m_{32}x_2 + m_{33}x_3 + m_{34} \end{aligned},$$

which is expressed by a simple matrix multiplication $(y = Mx)$:

$$\begin{bmatrix} y_1 \\ y_2 \\ y_3 \\ 1 \end{bmatrix} = \begin{bmatrix} m_{11} & m_{12} & m_{13} & m_{14} \\ m_{21} & m_{22} & m_{23} & m_{24} \\ m_{31} & m_{32} & m_{33} & m_{34} \\ 0 & 0 & 0 & 1 \end{bmatrix} \begin{bmatrix} x_1 \\ x_2 \\ x_3 \\ 1 \end{bmatrix}$$

Translations

If a point x is translated by L units, then the translation can be expressed by:

$$y = x + L \text{ or } \begin{bmatrix} y_1 \\ y_2 \\ y_3 \\ 1 \end{bmatrix} = \begin{bmatrix} 1 & 0 & 0 & L_1 \\ 0 & 1 & 0 & L_2 \\ 0 & 0 & 1 & L_3 \\ 0 & 0 & 0 & 1 \end{bmatrix} \begin{bmatrix} x_1 \\ x_2 \\ x_3 \\ 1 \end{bmatrix}$$

Rotations

A rotation of θ_1 angles around the X axis is represented via:

$$\begin{bmatrix} y_1 \\ y_2 \\ y_3 \\ 1 \end{bmatrix} = \begin{bmatrix} 1 & 0 & 0 & 0 \\ 0 & \cos(\theta_1) & \sin(\theta_1) & 0 \\ 0 & -\sin(\theta_1) & \cos(\theta_1) & 0 \\ 0 & 0 & 0 & 1 \end{bmatrix} \begin{bmatrix} x_1 \\ x_2 \\ x_3 \\ 1 \end{bmatrix}.$$

Rotations around the Y and Z axes are performed by the following equations:

$$\begin{bmatrix} \cos(\theta_2) & 0 & \sin(\theta_2) & 0 \\ 0 & 1 & 0 & 0 \\ -\sin(\theta_2) & 0 & \cos(\theta_2) & 0 \\ 0 & 0 & 0 & 1 \end{bmatrix} \text{ and } \begin{bmatrix} \cos(\theta_3) & \sin(\theta_3) & 0 & 0 \\ -\sin(\theta_3) & \cos(\theta_3) & 0 & 0 \\ 0 & 0 & 1 & 0 \\ 0 & 0 & 0 & 1 \end{bmatrix}.$$

Multiplying the three matrices together in an appropriate order generates the rotation matrix R.

Scaling

Scaling is needed to change the image size along orthogonal axes. The equation is expressed as:

$$\begin{bmatrix} y_1 \\ y_2 \\ y_3 \\ 1 \end{bmatrix} = \begin{bmatrix} S_1 & 0 & 0 & 0_1 \\ 0 & S_2 & 0 & 0 \\ 0 & 0 & S_3 & 0 \\ 0 & 0 & 0 & 1 \end{bmatrix} \begin{bmatrix} x_1 \\ x_2 \\ x_3 \\ 1 \end{bmatrix}$$

Parameterizing a Rigid-body Registration

When performing rigid body registration, nine parameters ($L_1, L_2, L_3, \theta_1, \theta_2, \theta_3, S_1, S_2, S_3$) of the registration matrix M need to be estimated: $M = L \times R \times S$, where

$$R = \begin{bmatrix} 1 & 0 & 0 & 0 \\ 0 & \cos(\theta_1) & \sin(\theta_1) & 0 \\ 0 & -\sin(\theta_1) & \cos(\theta_1) & 0 \\ 0 & 0 & 0 & 1 \end{bmatrix} \times \begin{bmatrix} \cos(\theta_2) & 0 & \sin(\theta_2) & 0 \\ 0 & 1 & 0 & 0 \\ -\sin(\theta_2) & 0 & \cos(\theta_2) & 0 \\ 0 & 0 & 0 & 1 \end{bmatrix} \times \begin{bmatrix} \cos(\theta_3) & \sin(\theta_3) & 0 & 0 \\ -\sin(\theta_3) & \cos(\theta_3) & 0 & 0 \\ 0 & 0 & 1 & 0 \\ 0 & 0 & 0 & 1 \end{bmatrix},$$

$$L = \begin{bmatrix} 1 & 0 & 0 & L_1 \\ 0 & 1 & 0 & L_2 \\ 0 & 0 & 1 & L_3 \\ 0 & 0 & 0 & 1 \end{bmatrix} \text{ and } S = \begin{bmatrix} S_1 & 0 & 0 & 0_1 \\ 0 & S_2 & 0 & 0 \\ 0 & 0 & S_3 & 0 \\ 0 & 0 & 0 & 1 \end{bmatrix}.$$

In this project, to simplify the algorithm of calculating the rigid body registration matrix, the three translation parameters are determined from two centroids in two tumors. The

three rotation parameters are determined from the angles between two vectors: centroid points to the maximum points. The three scaling parameters are also determined from the magnitude of two vectors: centroid points to the maximum points. The flow chart of this algorithm is shown in Figure 4.15 below.

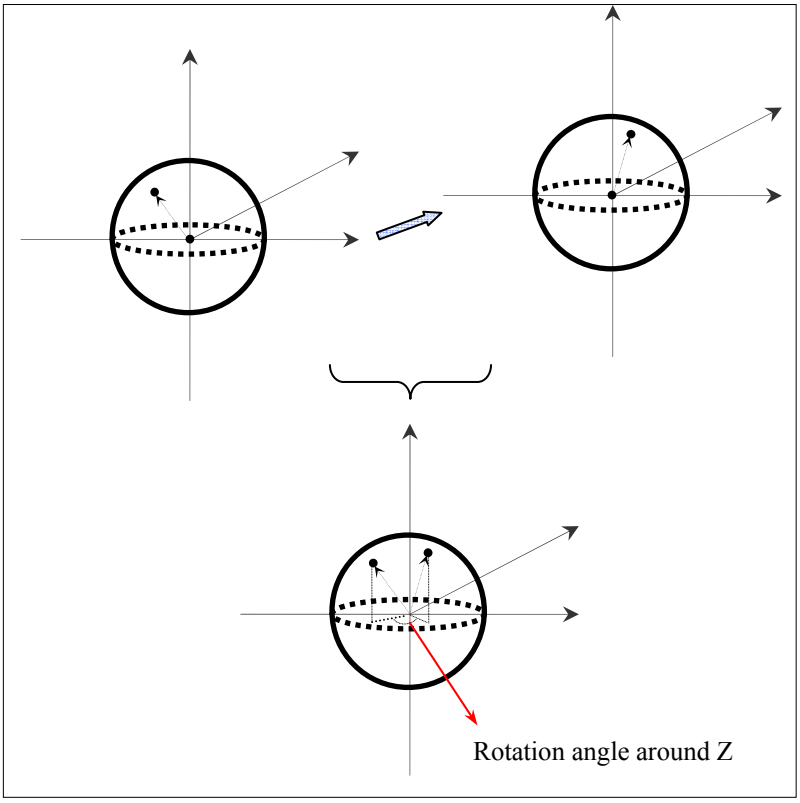

Figure 4.15 Calculation of the Rigid Body registration matrix: two centroid points determine the translation parameters, two vectors: centroid points to maximum points determine the rotation and scaling parameters.

5. RESULT

5.1 Image Acquisition

The PET and CT DICOM images obtained from the hybrid PET/CT scanner were read into respective volume files. CT images, PET images and fused images of the physical phantom in Coronal, Sagittal and Transaxial views are displayed in Figure 5.1.

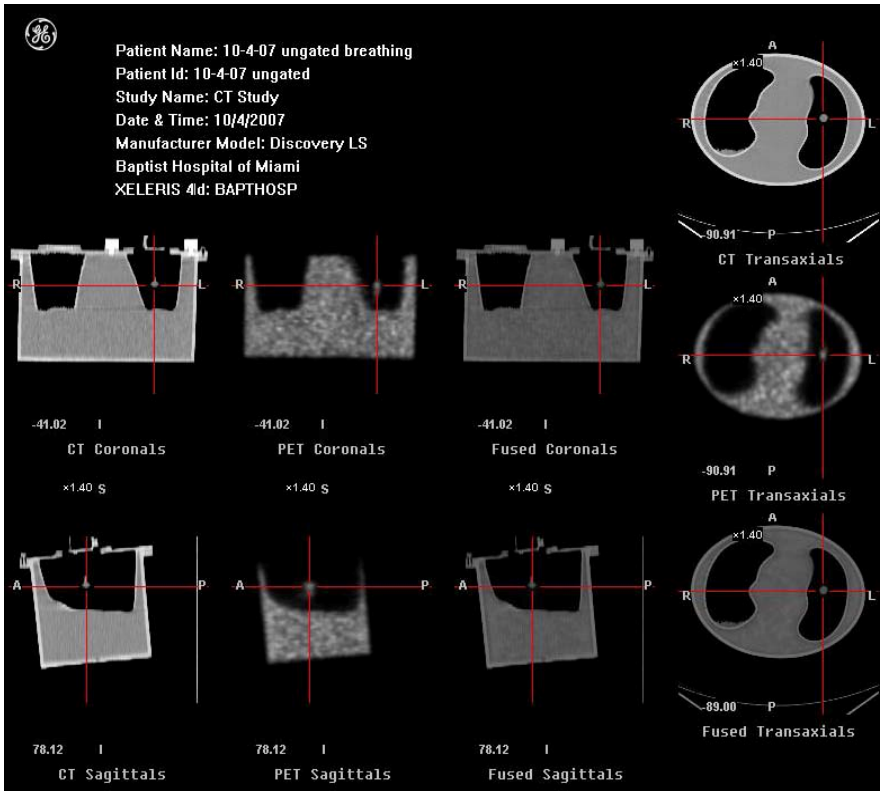

Figure 5.1 Coronal, Sagittal and Transaxial view of the Physical phantom for CT images, PET images and fused images.

5.2 Image Segmentation

5.2.1 CT Image Processing

The results of processing the CT volume file of the physical phantom to segment lung regions are shown below. The first step of segmenting dominant regions of the images, like body region and background was accomplished by the method of global thresholding, which partitions the histogram of the image using a single global threshold

T. Figures 5.2a and 5.2b illustrate the effect of global thresholding of a CT image on its histogram

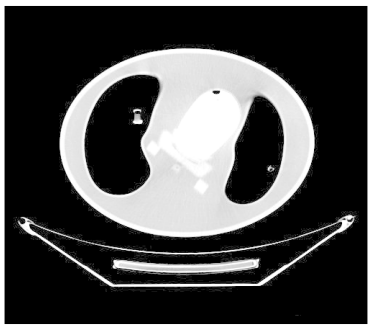
(a)

(b)

Figure 5.2 Original CT Slice on the left and Binary CT slice on right

After segmenting the major regions (i.e. body and background) all the other small regions were blanked out by means of region labeling. Figure 5.3a shows the same CT slice in Figure 5.2b but with all the small regions (including tumors) blanked out. Figure 5.3b illustrates the step of closing the lung regions in-order to obtain the entire extent of body.


(a)
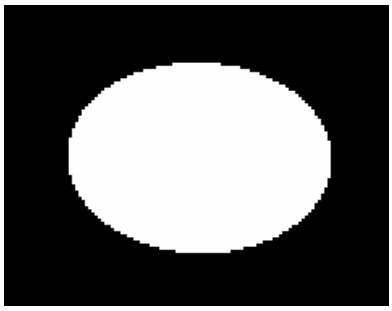
(b)

Figure 5.3 Left: binary CT slice with only tissue and lungs. Right: binary CT slice with closed lung regions.

After obtaining the extent of the body region in the images, the next step of determining the range of CT slices containing lungs was accomplished by plotting the total number of pixels falling below the threshold for each slice of the CT volume file (Figure 5.4). The plot can be divided into four distinct regions. The first region shows a plateau with an average of zero. This region corresponds to the CT slices in the volume file, which consist of purely tissue regions and have very few pixels below the iterative threshold.

The second region shows a constant increase till it reaches the peak. This region correlates with the appearance of the lungs (which have the maximum number of pixels falling below the threshold). The third region shows a constant decrease in the magnitude of the plot. This region correlates with the disappearance of lungs in the CT volume file. The fourth region is again a plateau consisting of purely tissue regions

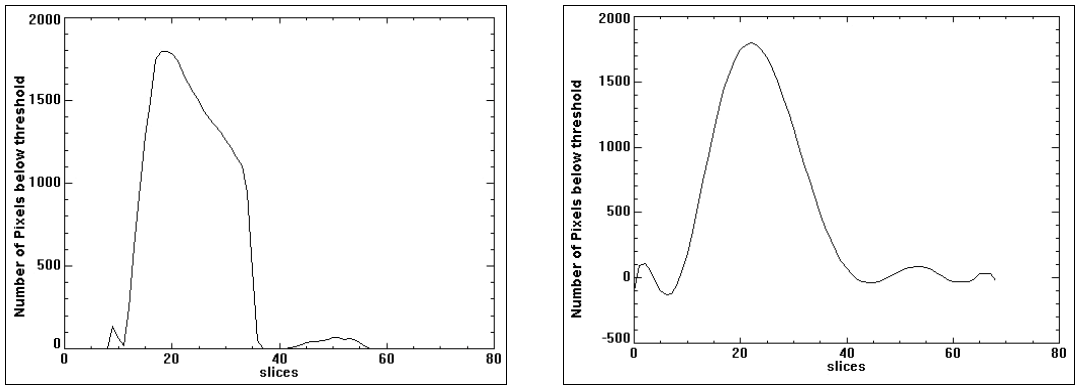

Figure 5.4 Left: plot of number of pixels less than the iterative threshold vs. total number pixels and right: plot on the right was smoothed by cubic spline interpolation.

The curve on the right in Figure 5.4 was smoothed by fitting a polynomial of order 10, and its differential was obtained to determine the inflection points. The lungs first appear in the slice where the plot begins its constant increase towards the peak. The lungs completely disappear starting with the slice where the curve returns to an average value of zero. In the sample case of the physical phantom, the inflection points were calculated and it was determined that the lung appears at the 7^{th} slice, lung disappears at the 45th slice and can be viewed very clearly at slice 22. All further image processing was done using the CT slices containing the lungs.

The next step was to segment the lung regions in the CT volume file. Figure 5.5a shows the binary template of segmented lung regions obtained from Figured 5.2 and 5.3. This binary template does not differentiate the tumor that can be seen in Figure 5.2a. Figure

5.5b shows the binary template of the lung regions excluding the tumor, obtained using binary templates seen in Figures 5.5a, 5.2b and 5.3.

 (a)  (b)

Figure 5.5 (a) binary templates of segmented CT lungs, (b) binary Templates of segmented lungs excluding tumor

5.2.2 Identification of PET Tumors

The binary templates of segmented CT slices are used to segment lung regions from PET slices of the physical phantom. As PET images only depict functional activity and because of the lower consumption of FDG in the lung, the exact delineation of the lung regions cannot be seen in the PET slices. It can be seen from the Figure 5.5 that only the tumors with the highest activity are clear. The rest of the region is filled with a background activity and appears black.

Figure 5.6 Segmented lung regions in PET images

The results comparing the actual tumor size with the computed size of the segmented tumors are shown in Table 5.1 for static tumors. We can see that the NCAT computer phantom gives very good results. For the physical phantom, the volume of one voxel is calculated as: *Volume of one voxel* = $x \times y \times z$

where x and y are the pixel spacing in the horizontal and vertical directions respectively and z is the slice thickness. The segmented tumor volume is calculated by *single voxel volume* × *total voxels in the tumor*. The 6.95 mm size tumor is too small for the PET

scanner to identify. The mismatch between the segmented tumor and the true volume for the physical phantom is due to the partial-volume and spillover effects, and also the limitation of the spatial resolution of the PET scanner.

Tumor diameter (mm)		True Tumor Volume	Segmented Tumor Size	Percentage Difference
NCAT Phantom (w/Poisson Noise)	6.0	17 pixels	20 pixels	17.6%
	8.5	33 pixels	38 pixels	15.2%
	10.0	44 pixels	48 pixels	9.1%
	20.0	230 pixels	244 pixels	6.1%
	25.0	409 pixels	422 pixels	3.2%
NCAT Phantom (w/Random Noise)	6.0	17 pixels	18 pixels	11.7%
	8.5	33 pixels	36 pixels	9.1%
	10.0	44 pixels	48 pixels	9.1%
	20.0	230 pixels	239 pixels	3.9%
	25.0	409 pixels	415 pixels	1.4%
Physical Phantom	8.23	0.13 ml	/	/
	9.86	0.25 ml	0.46 ml	84.0 %
	11.89	0.50 ml	0.72 ml	64.0%
	14.43	1.00 ml	1.13 ml	13.0%
	17.69	2.00 ml	2.21 ml	10.5%

Table 5.1 Results comparing the true tumor volume with the segmented tumor volume. Here the segmentation was performed on the static PET images so that we can compare our result with the true tumor volume (gold standard). / means the tumor is too small for the algorithm to identify.

5.3 Motion Track and Registration Schemes

The results after applying the registration/integration algorithm has been validated using the computer simulated NCAT phantom data and the physical phantom for different size tumors. Figure 5.7 shows one example of the PET images from the physical phantom after intensity based registration. Comparing the centered and right images in the figure, the blurring effect of the tumor due to motion has been reduced.

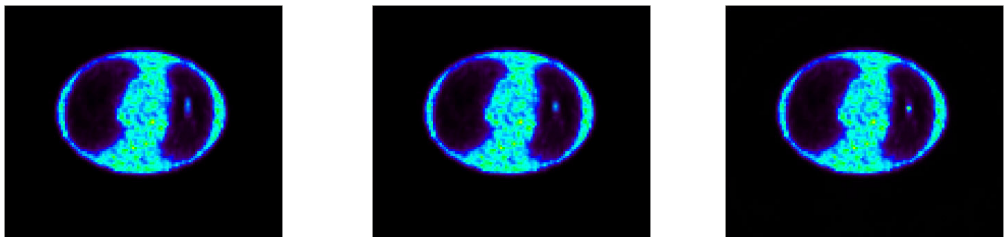

Figure 5.7 Left: Ungated PET image of the physical phantom. Center: original gated PET image (one of the gated images). Right: motion corrected PET image after applying Intensity Registration.

5.3.1 Intensity Based Registration

The following results show the correlation between the original tumor and the registered tumor. As intensity based registration algorithm automatically combined all other bins into a single bin, each bin was not compared one by one. Comparisons were carried out for different tumor sizes. Figure 5.8 shows the cross-correlation results of two NCAT phantoms (with Gaussian noise and with Poisson noise) and the physical phantom. Here the cross-correlation values refer to the correlation between the un-corrected data with the static PET data (gold standard) and the corrected data (after registration) with the static data. For the NCAT phantom with Gaussian Noise, the simulation of the 10 mm tumors was repeated three times to simulate experimental variability, and the error bars in the figures represents standard deviation, There isn't much change in the correlation coefficients, activity concentrations and relative noise levels (less than 3% deviation from the mean value) using intensity based registration as seen from Figure 5.8 (a), 5.9 (a) and 5.10 (a), and similar results were obtained using other registration methods showing no difference between each simulations as can be seen in the following chapters.

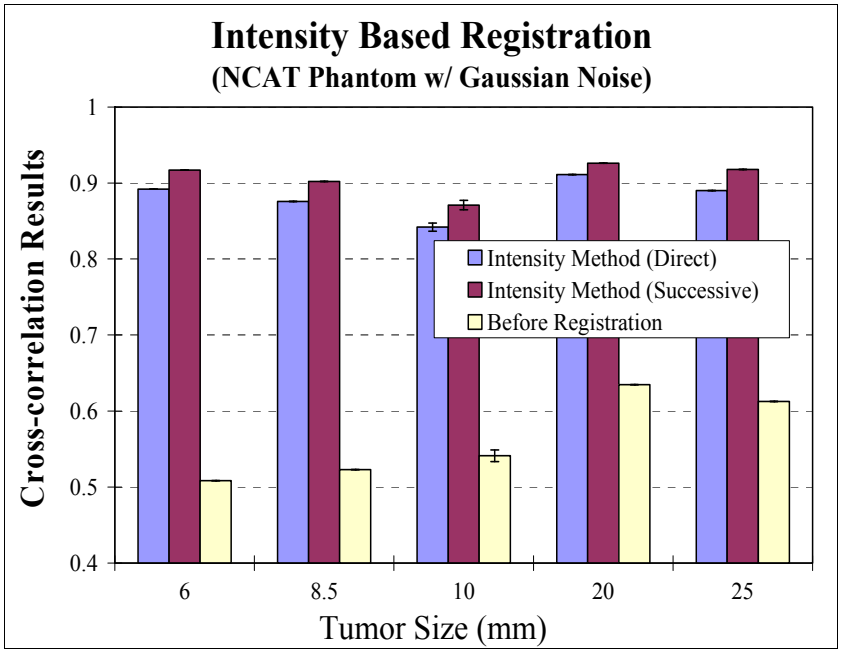
Intensity Based Registration
(NCAT Phantom w/ Gaussian Noise)
Cross-correlation Results
1
0.9
0.8
0.7
0.6
0.5
0.4
Intensity Method (Direct)
Intensity Method (Successive)
Before Registration
6
8.5
10
20
25
Tumor Size (mm)

(a)

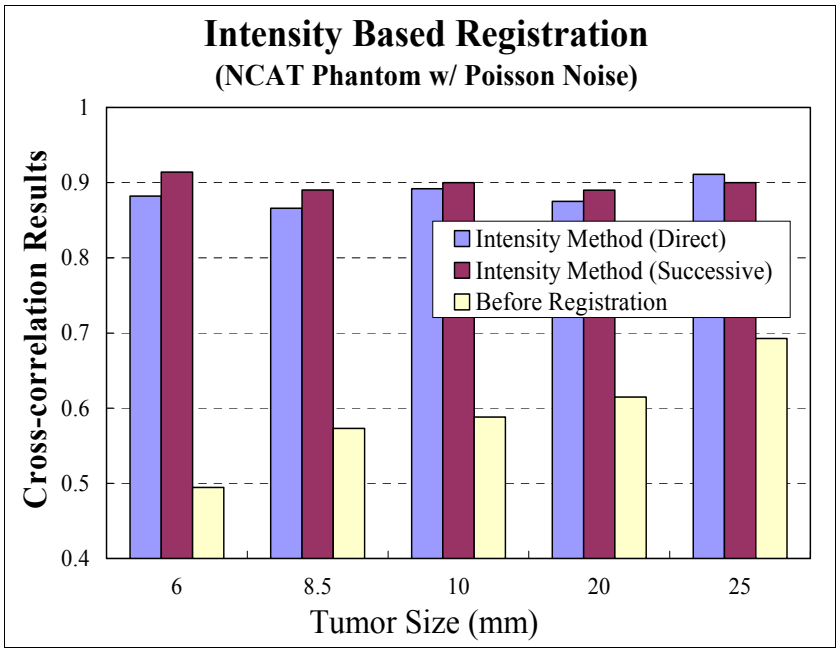
Intensity Based Registration
(NCAT Phantom w/ Poisson Noise)
Cross-correlation Results
1
0.9
0.8
0.7
0.6
0.5
0.4
Intensity Method (Direct)
Intensity Method (Successive)
Before Registration
6
8.5
10
20
25
Tumor Size (mm)

(b)

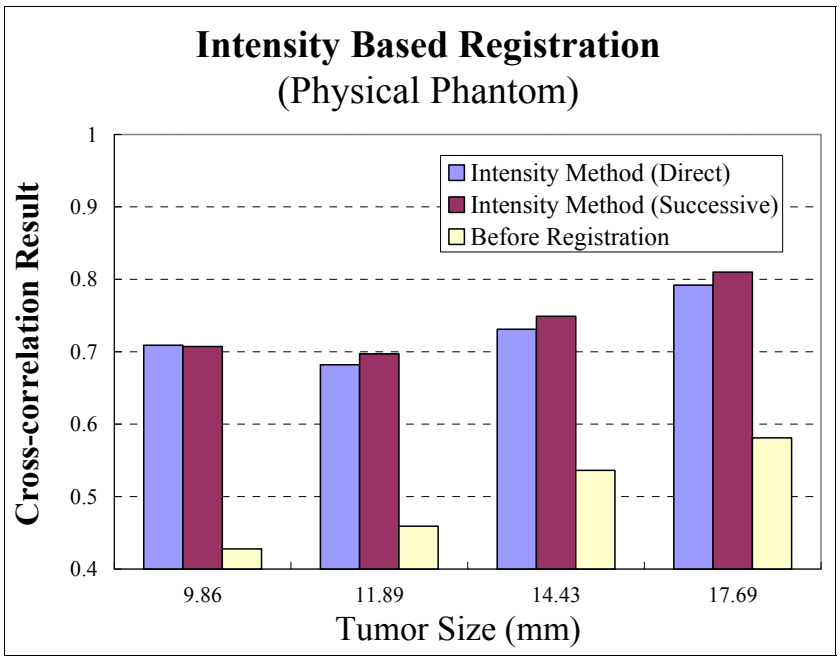

(c)

Figure 5.8 (a) Cross-correlation results of NCAT phantom with Gaussian noise simulated for 5 different size tumors using intensity based registration algorithm, before registration compared to after Direct Scheme and Successive Scheme. (b) Cross-correlation results of NCAT phantom with Poisson noise simulated (c) Cross-correlation results of physical phantom for 4 different size tumors. The 5th tumor of the physical phantom is too small for the algorithm to identify.

The quantitative results of activity concentration are evaluated with reference to the static PET, ungated PET and gated PET as shown in Figure 5.9. Here the activity concentration is calculated as the average activity over the entire tumor region. Next the values were normalized to the static PET value (which is the gold standard for comparison). It can be seen that the activity concentrations after registration are closer to the true values.

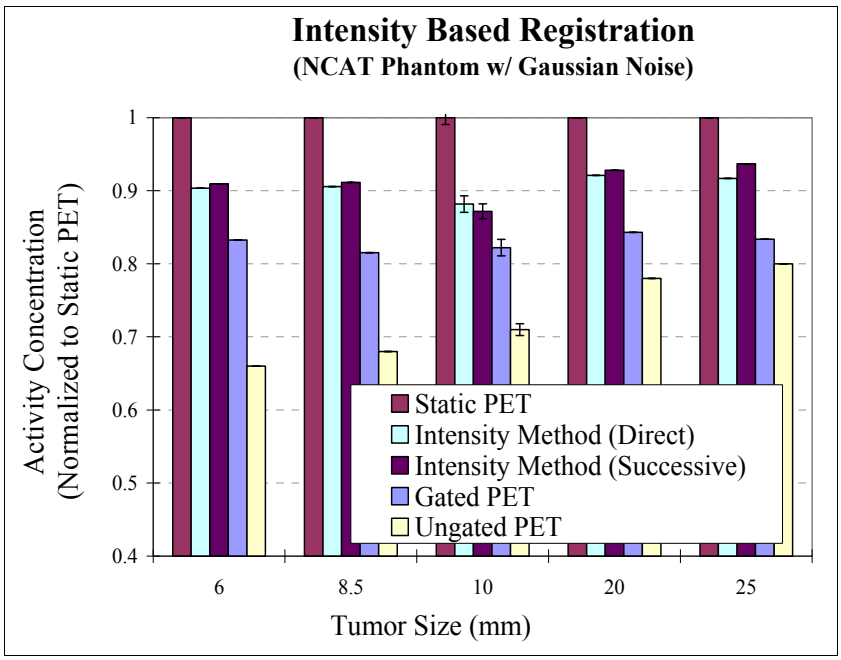
Intensity Based Registration
(NCAT Phantom w/ Gaussian Noise)
Activity Concentration
(Normalized to Static PET)
1
0.9
0.8
0.7
0.6
0.5
0.4
6
8.5
10
20
25
Tumor Size (mm)
Static PET
Intensity Method (Direct)
Intensity Method (Successive)
Gated PET
Ungated PET

(a)

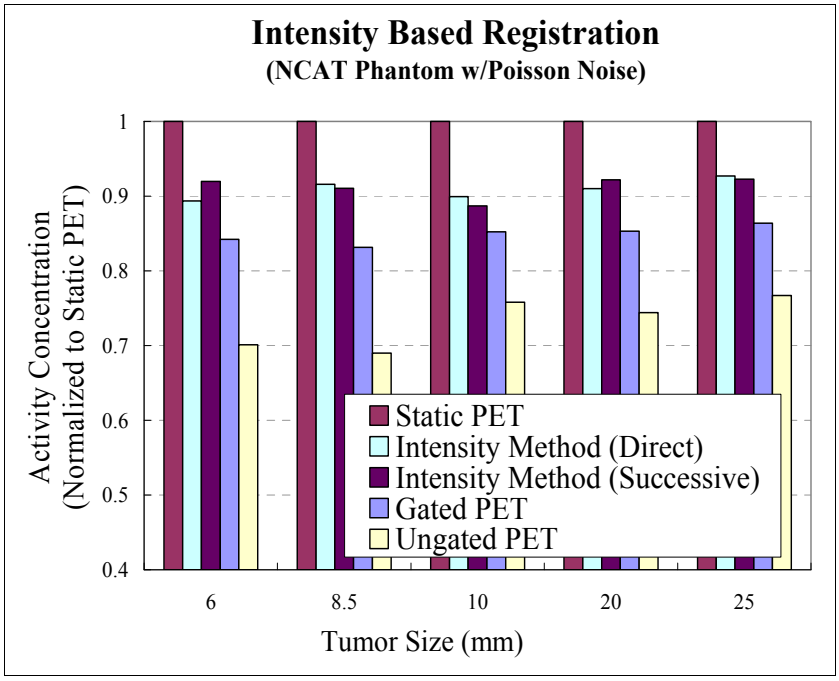
Intensity Based Registration
(NCAT Phantom w/Poisson Noise)
Activity Concentration
(Normalized to Static PET)
1
0.9
0.8
0.7
0.6
0.5
0.4
6
8.5
10
20
25
Tumor Size (mm)
Static PET
Intensity Method (Direct)
Intensity Method (Successive)
Gated PET
Ungated PET

(b)

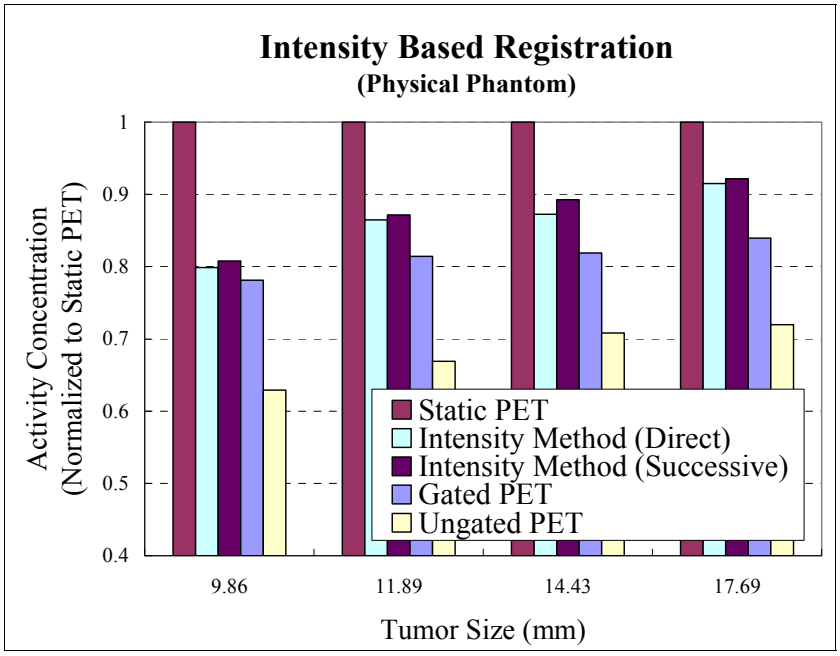

(c)

Figure 5.9 (a) NCAT phantom with Gaussian noise results, error bars with 10 mm tumor simulations are for standard deviation, N=3 (b) NCAT phantom with Poisson noise results and (c) physical phantom results, activity concentration of Intensity registration algorithms with Direct and Successive Scheme, static PET, gated PET and ungated PET images, here gated PET means the average of all of the individual gates. All of the values are normalized to the static PET (gold standard). Here gated PET values come from the average value of all gated bin.

The results of the actual tumor size with the computed size of segmented tumors are shown in Table 5.1, to compare gated tumors (average of all of the individual gates) with registered tumors (with Intensity Direct Scheme and Intensity Successive Scheme). After registration/combining of all gates, the tumor size doesn't increase much compared with the gated tumor; some even became smaller compared with the gated tumor. This is due to the shrinking process before registration.

Tumor diameter (mm)		**True Tumor Volume**	**Segmented Tumor Size**		
			Gated Tumor	**Intensity (Direct)**	**Intensity (Successive)**
NCAT Phantom (w/Poisson Noise)	6.0	17 pixels	20 pixels	18 pixels	18 pixels
	8.5	33 pixels	38 pixels	36 pixels	36 pixels
	10.0	44 pixels	48 pixels	45 pixels	45 pixels
	20.0	230 pixels	241 pixels	237 pixels	237 pixels

	25.0	409 pixels	424 pixels	420 pixels	420 pixels
NCAT Phantom (w/Gaussian Noise)	6.0	17 pixels	19 pixels	19 pixels	19 pixels
	8.5	33 pixels	38 pixels	39 pixels	39 pixels
	10.0	44 pixels	48 pixels	46 pixels	46 pixels
	20.0	230 pixels	244 pixels	244 pixels	240 pixels
	25.0	409 pixels	422 pixels	418 pixels	418 pixels
Physical Phantom	8.23	0.13 ml	/	/	/
	9.86	0.25 ml	0.48 ml	0.49 ml	0.49 ml
	11.89	0.50 ml	0.76 ml	0.79 ml	0.78 ml
	14.43	1.00 ml	1.17 ml	1.17 ml	1.19 ml
	17.69	2.00 ml	2.29 ml	2.31 ml	2.33 ml

Table 5.2 Results comparing the true tumor volume with the segmented tumor volume. / means the tumor is too small for the algorithm to identify.

Relative noise levels are also compared. Lower noise is achieved after registration as shown in Figure 5.10 for both the NCAT phantom and the physical phantom. Here the relative noise level is estimated by the standard deviation of the tumor region over the average value of the tumor region.

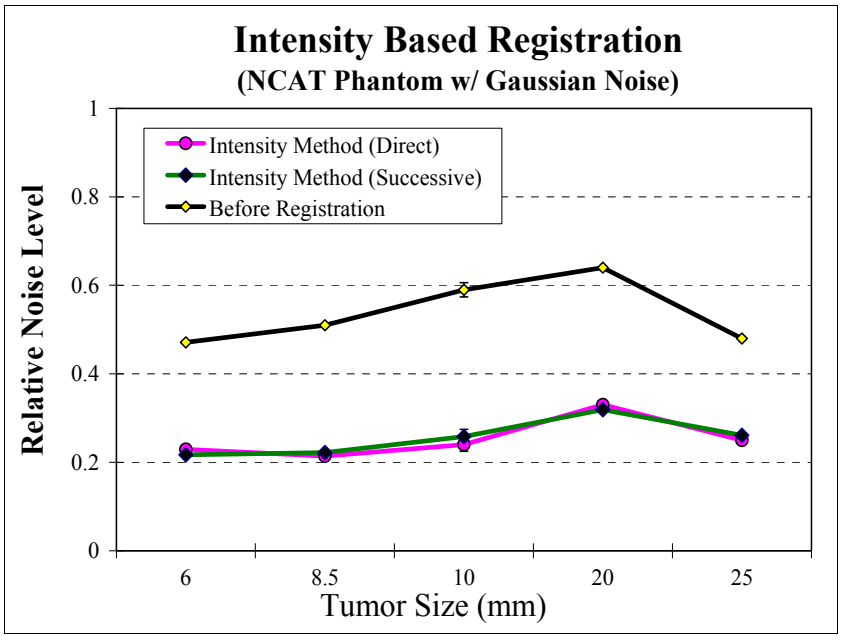

(a)

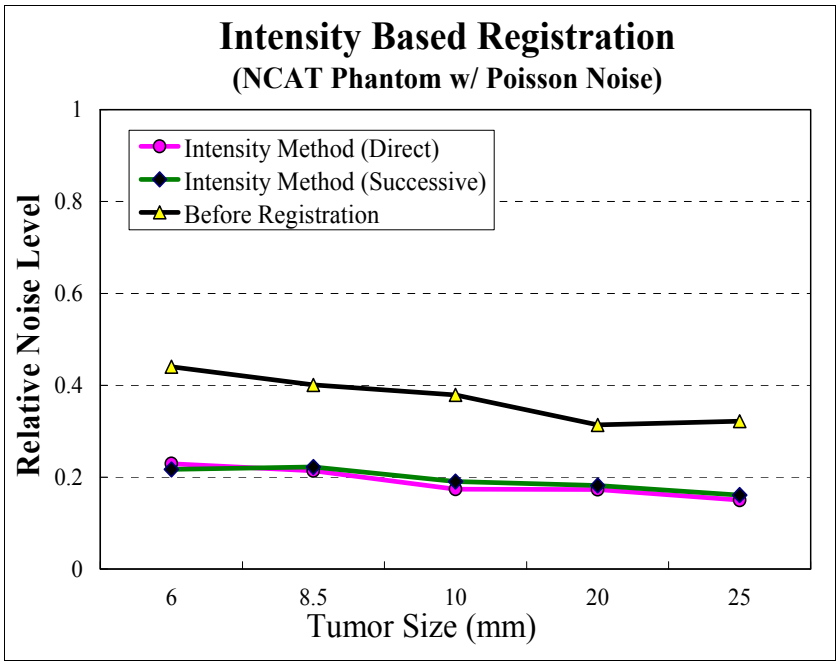

(b)

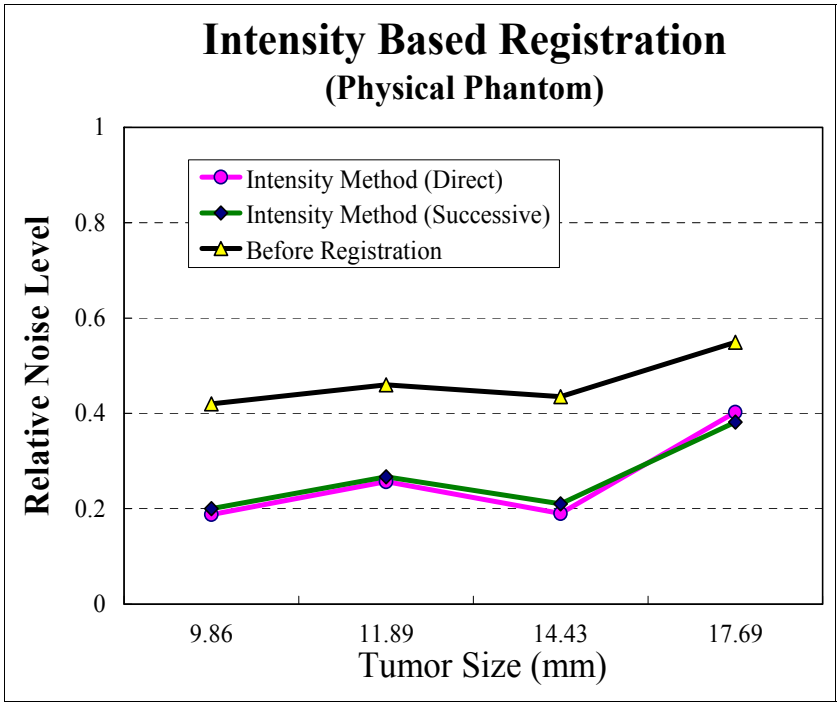

(c)

Figure 5.10 Comparing relative noise level before registration and after Intensity registration with direct and Successive Scheme: (a) NCAT phantom with Gaussian noise, error bars with 10 mm tumor simulations are for standard deviation, N=3 (b) NCAT phantom with Poisson noise, (c) Physical phantom.

5.3.2 Centroid Based registration

Figure 5.11 shows the cross-correlation results of NCAT phantom and physical phantom using Centroid Based registration with Direct and Successive Schemes; similar results as Intensity registration were obtained.

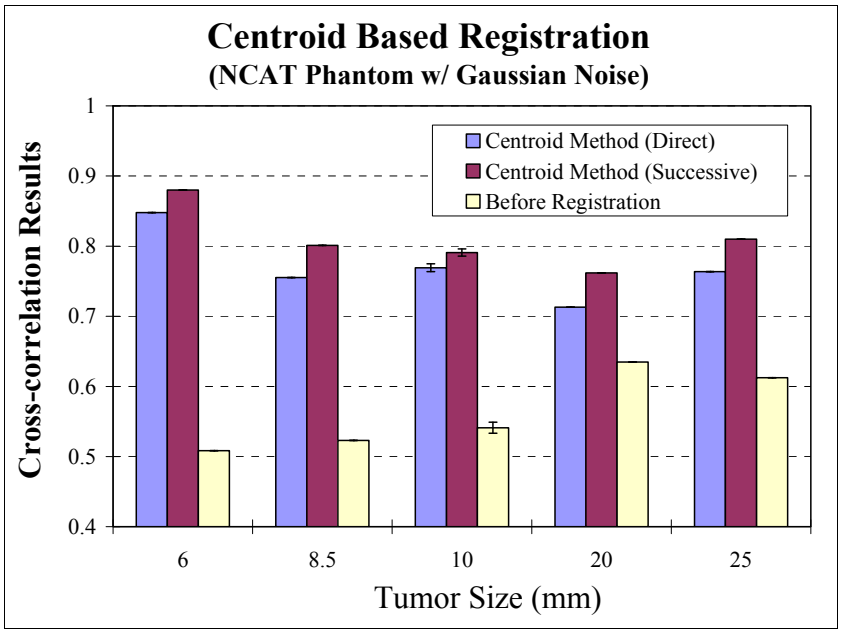

(a)

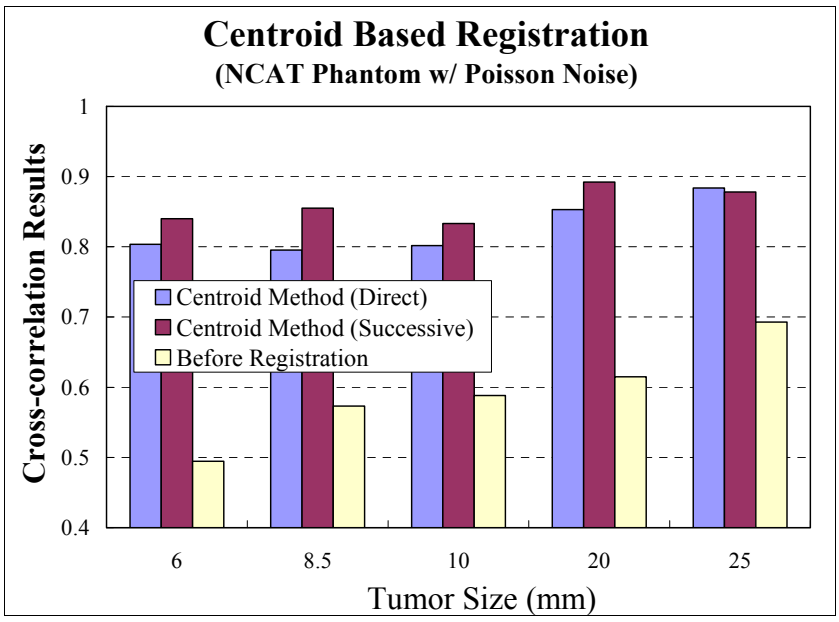

(b)

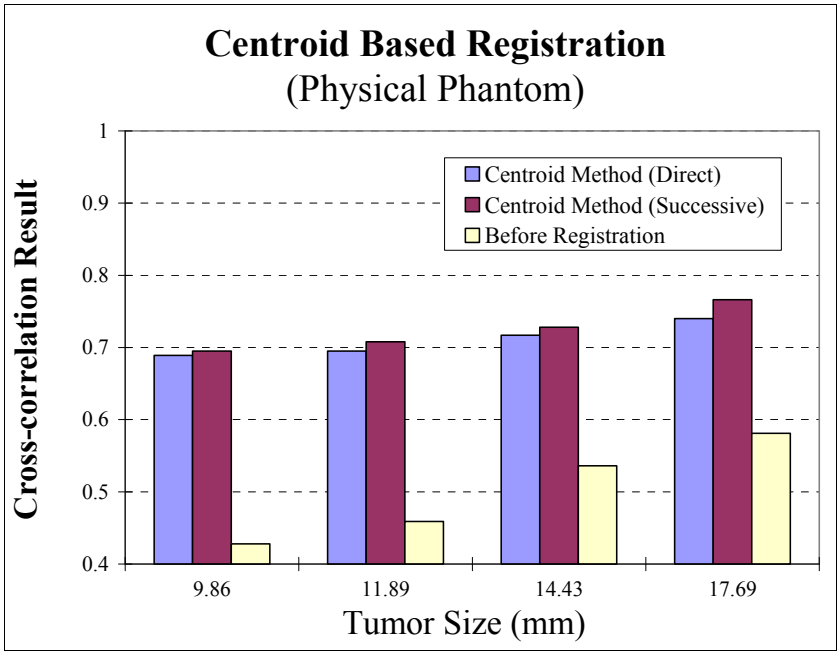

(c)

Figure 5.11 (a) Cross-correlation results of NCAT phantom with Gaussian noise simulated for 5 different size tumors using Centroid based registration algorithm, before registration compared to after Direct Scheme and Successive Scheme. The error bars with 10 mm tumor simulations are for standard deviation, N=3 (b) Cross-correlation results of NCAT phantom with Poisson noise simulated (c) Cross-correlation results of physical phantom for 4 different size tumors.

The quantitative results of activity concentration are also evaluated with reference to the static PET, non-gated PET and non-registered gated PET as shown in Figure 5.12 below. Here the activity concentration is calculated as the average activity over the entire tumor region then the values are normalized to the static PET value (which is the gold standard for comparison).

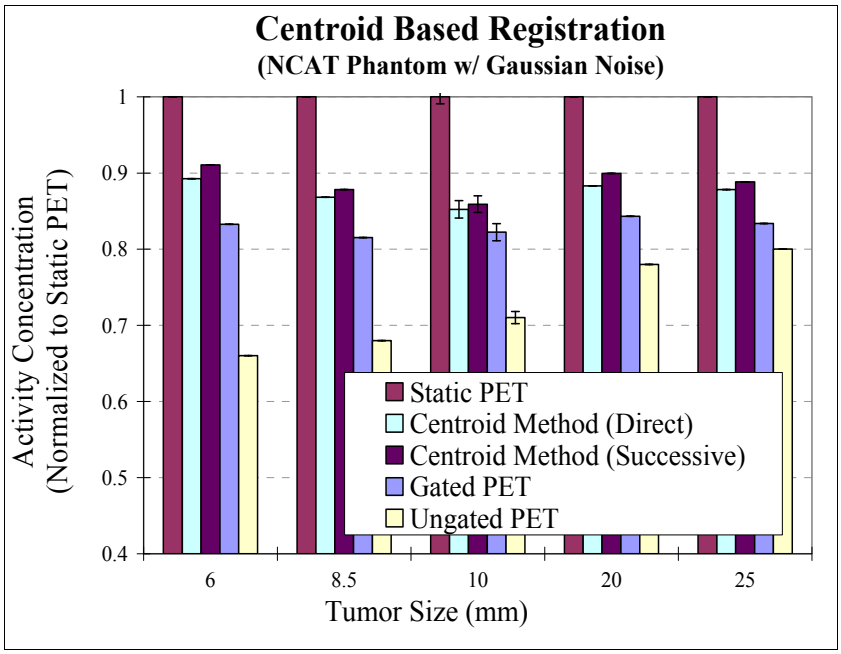
Centroid Based Registration
(NCAT Phantom w/ Gaussian Noise)
Activity Concentration
(Normalized to Static PET)
1
0.9
0.8
0.7
0.6
0.5
0.4
6
8.5
10
20
25
Tumor Size (mm)
Static PET
Centroid Method (Direct)
Centroid Method (Successive)
Gated PET
Ungated PET

(a)

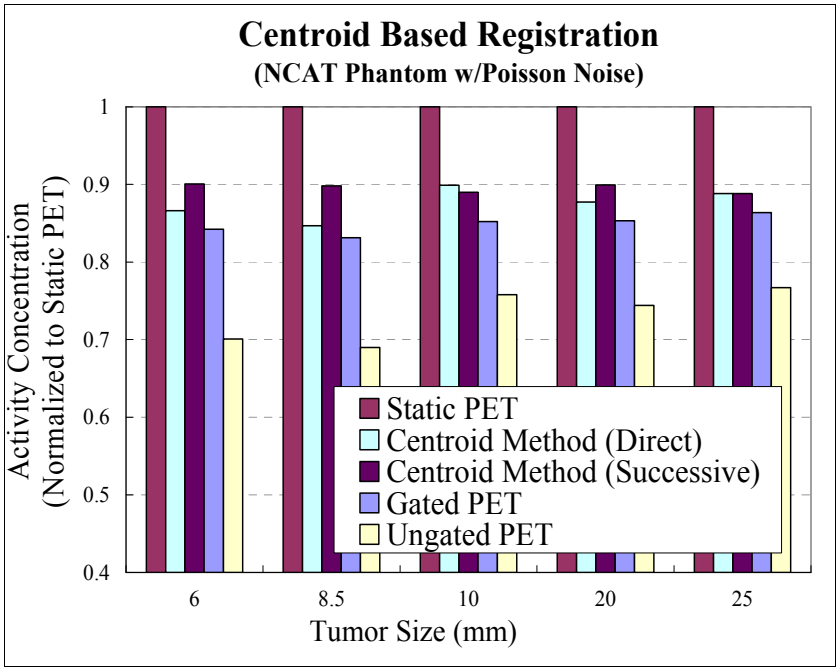
Centroid Based Registration
(NCAT Phantom w/Poisson Noise)
Activity Concentration
(Normalized to Static PET)
1
0.9
0.8
0.7
0.6
0.5
0.4
6
8.5
10
20
25
Tumor Size (mm)
Static PET
Centroid Method (Direct)
Centroid Method (Successive)
Gated PET
Ungated PET

(b)

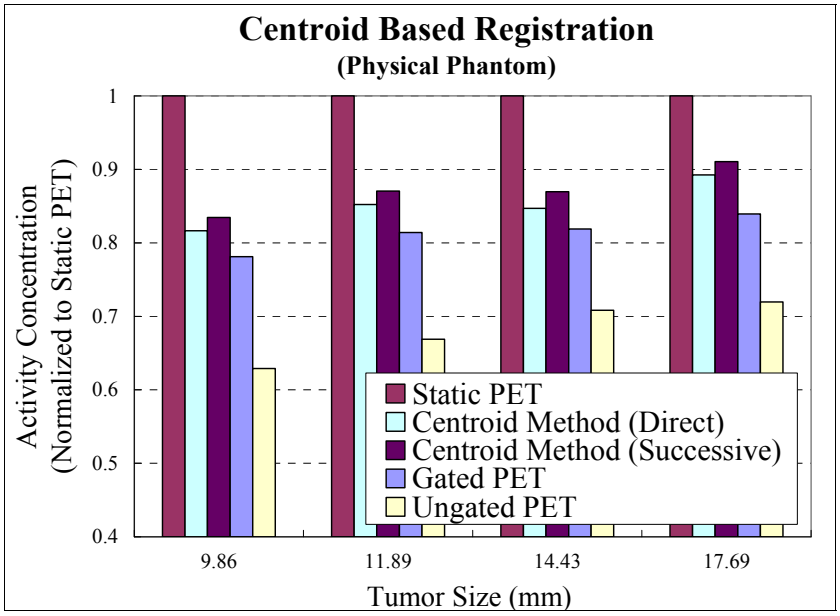

(c)

Figure 5.12 (a) NCAT phantom with Gaussian noise results, the error bars with 10 mm tumor simulations are for standard deviation, N=3, (b) NCAT phantom with Poisson noise results and (c) physical phantom results, activity concentration of Centroid registration algorithms with Direct and Successive Scheme, static PET, gated PET and ungated PET images. All of the values are normalized to the static PET (gold standard). Here gated PET values come from the average value of all of the gated bins.

The results of the actual tumor size with the computed size of segmented tumors are shown in Table 5.2, to compare gated tumors (average of all gates) with registered tumors (with Centroid Direct Scheme and Centroid Successive Scheme).

Tumor diameter (mm)		**True Tumor Volume**	**Segmented Tumor Size**		
			Gated Tumor	**Centroid (Direct)**	**Centroid (Successive)**
NCAT Phantom (w/Poisson Noise)	6.0	17 pixels	20 pixels	22 pixels	20 pixels
	8.5	33 pixels	38 pixels	41 pixels	41 pixels
	10.0	44 pixels	48 pixels	51 pixels	53 pixels
	20.0	230 pixels	241 pixels	252 pixels	255 pixels
	25.0	409 pixels	424 pixels	426 pixels	430 pixels
NCAT Phantom (w/Gaussian Noise)	6.0	17 pixels	18 pixels	19 pixels	20 pixels
	8.5	33 pixels	36 pixels	37 pixels	38 pixels
	10.0	44 pixels	48 pixels	50 pixels	51 pixels
	20.0	230 pixels	239 pixels	238 pixels	244 pixels
	25.0	409 pixels	415 pixels	416 pixels	423 pixels
Physical	8.23	0.13 ml	/	/	/

Phantom	9.86	0.25 ml	0.48 ml	0.55 ml	0.58 ml
	11.89	0.50 ml	0.76 ml	0.82 ml	0.82 ml
	14.43	1.00 ml	1.17 ml	1.21 ml	1.26 ml
	17.69	2.00 ml	2.29 ml	2.31 ml	2.32 ml

Table 5.3 Results comparing the true tumor volume with the segmented tumor volume. / means the tumor is too small for the algorithm to identify.

Relative noise levels are also compared. Lower noise is achieved after registration as shown in Figure 5.13 for both NCAT phantom and physical phantom.

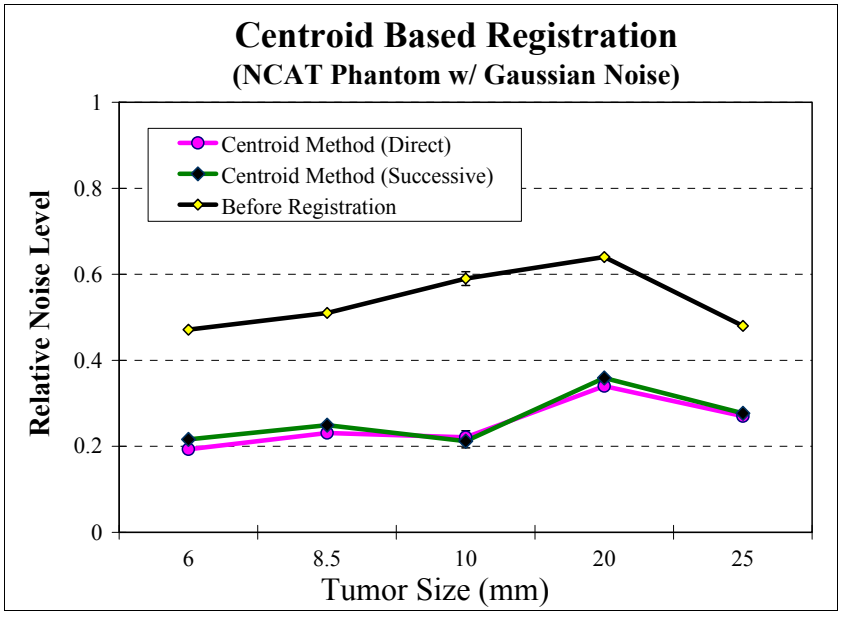

(a)

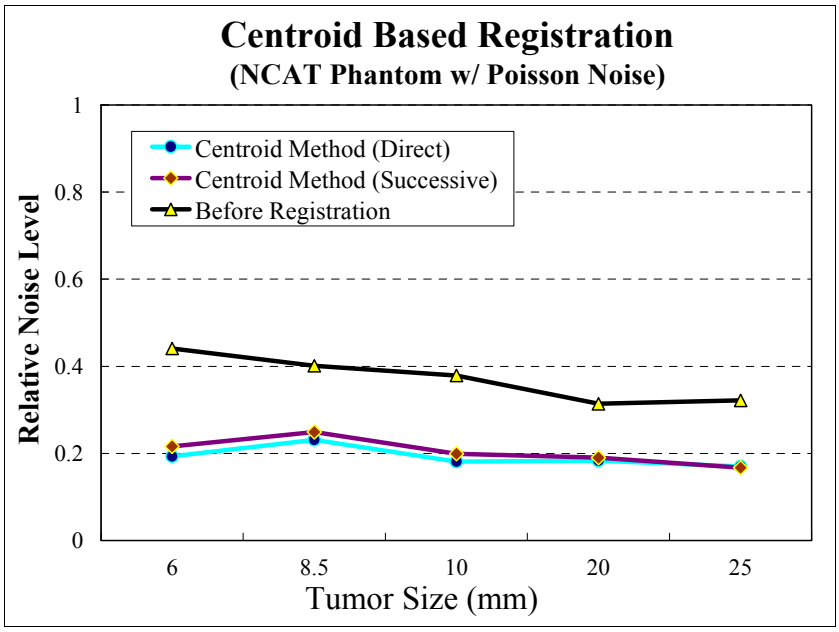

(b)

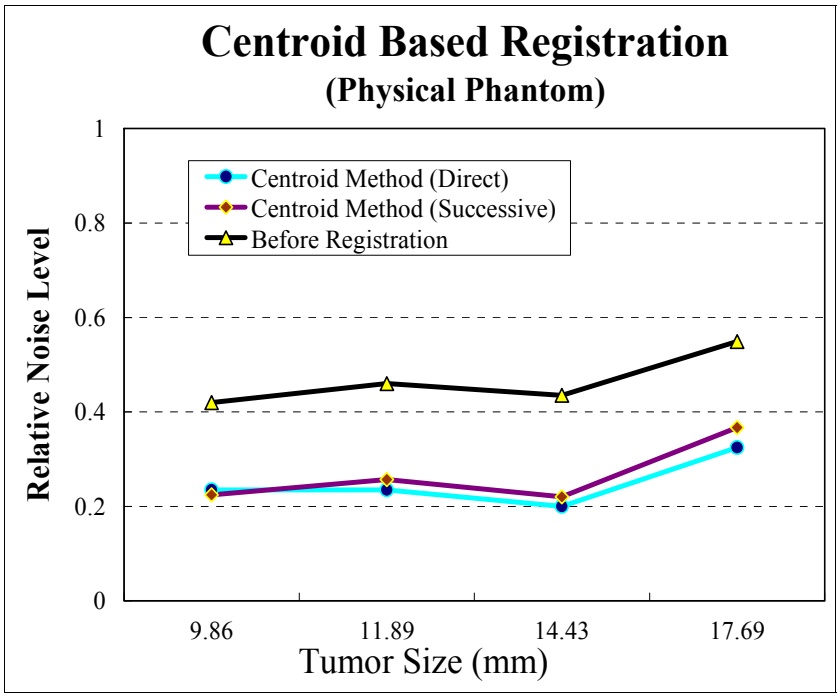

(c)

Figure 5.13 Comparing relative noise level before registration and after Intensity registration with direct and Successive Scheme: (a) NCAT phantom with Gaussian noise, the error bars with 10 mm tumor simulations are for standard deviation, N=3, (b) NCAT phantom with Poisson noise, (c) Physical phantom.

5.3.3 Rigid Body Registration

Figure 5.14 shows the cross-correlation results of the NCAT phantom and the physical phantom using Rigid Body registration with Direct and Successive Schemes; similar results as the two other registration methods before were obtained. The error bars of standard deviation indicating the variations of three simulations with 10 mm tumor are displayed in each figure, the standard deviation are within 3%.

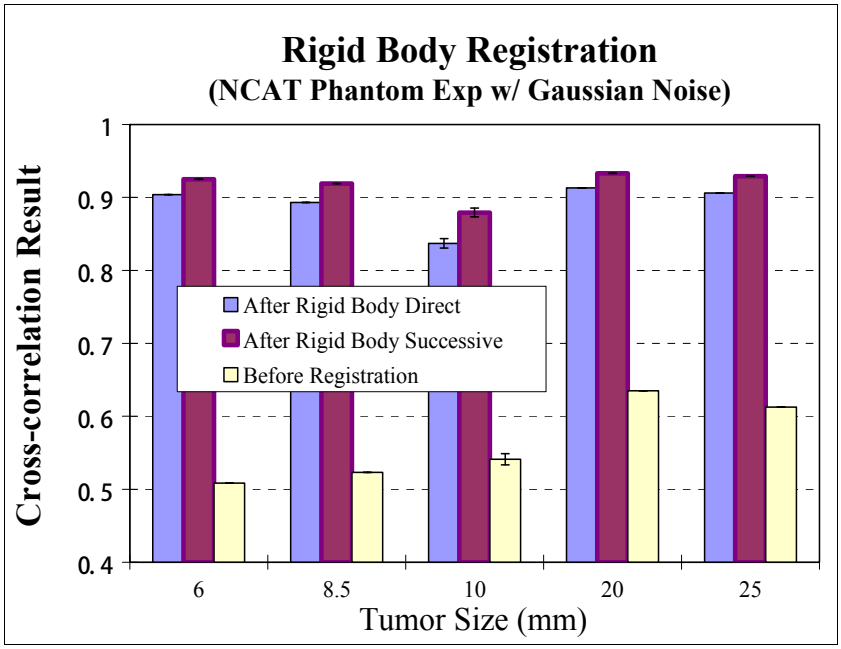
Rigid Body Registration
(NCAT Phantom Exp w/ Gaussian Noise)
Cross-correlation Result
1
0.9
0.8
0.7
0.6
0.5
0.4
After Rigid Body Direct
After Rigid Body Successive
Before Registration
6
8.5
10
20
25
Tumor Size (mm)

(a)

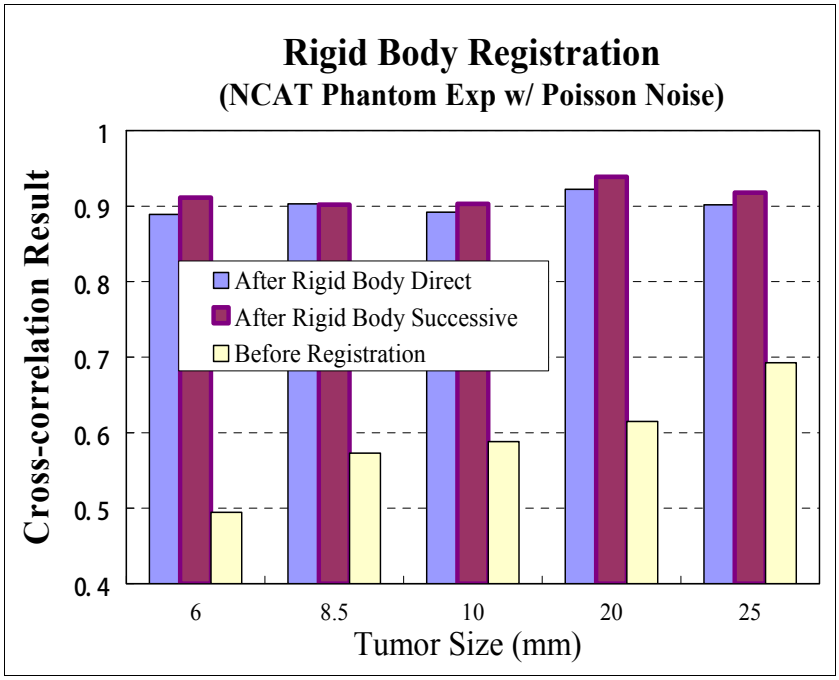
Rigid Body Registration
(NCAT Phantom Exp w/ Poisson Noise)
Cross-correlation Result
1
0.9
0.8
0.7
0.6
0.5
0.4
After Rigid Body Direct
After Rigid Body Successive
Before Registration
6
8.5
10
20
25
Tumor Size (mm)

(b)

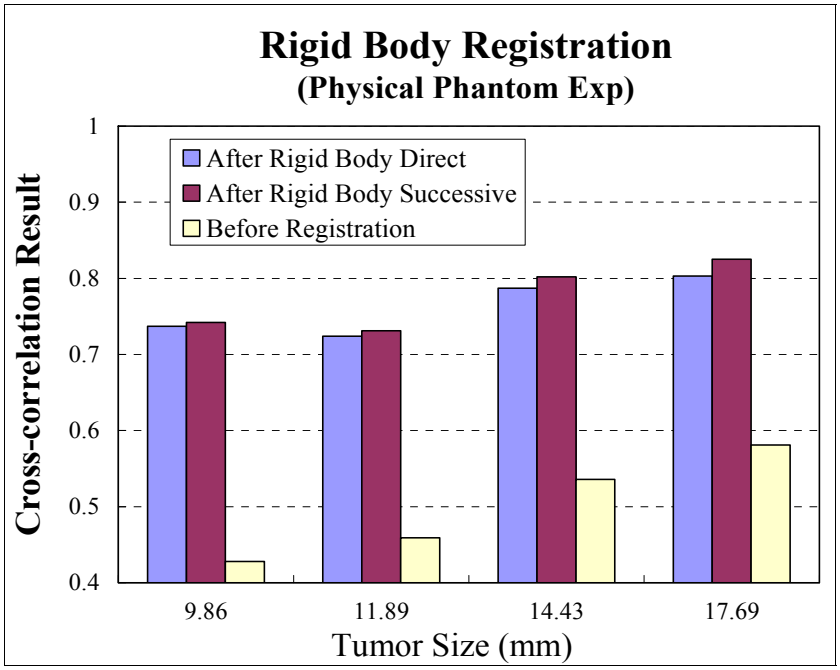

(c)

Figure 5.14 (a) Cross-correlation results of NCAT phantom with Gaussian noise simulated for 5 different size tumors using Rigid Body registration algorithm, before registration comparing to after Direct Scheme and Successive Scheme. The error bars with 10 mm tumor simulations are for standard deviation, N=3. (b) Cross-correlation results of NCAT phantom with Poisson noise simulated (c) Cross-correlation results of physical phantom for 4 different size tumors.

The quantitative results of activity concentration are also evaluated with reference to the static PET, non-gated PET and non-registered gated PET as shown in Figure 5.15 below. Here the activity concentration is calculated as the average activity over the entire tumor region, then the values are normalized to the static PET value (which is the gold standard for comparison).

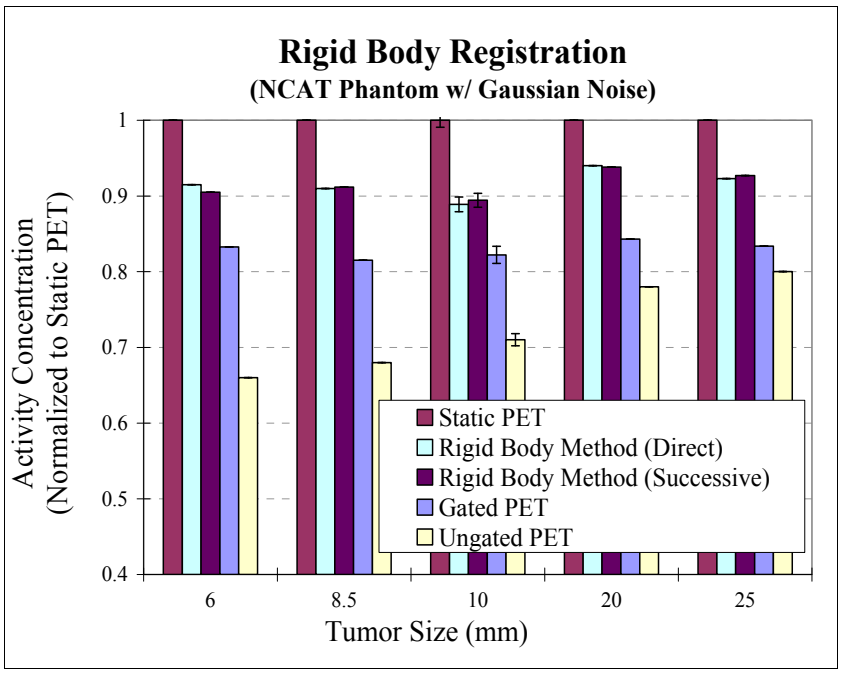
Rigid Body Registration
(NCAT Phantom w/ Gaussian Noise)
Activity Concentration
(Normalized to Static PET)
1
0.9
0.8
0.7
0.6
0.5
0.4
6
8.5
10
20
25
Tumor Size (mm)
Static PET
Rigid Body Method (Direct)
Rigid Body Method (Successive)
Gated PET
Ungated PET

(a)

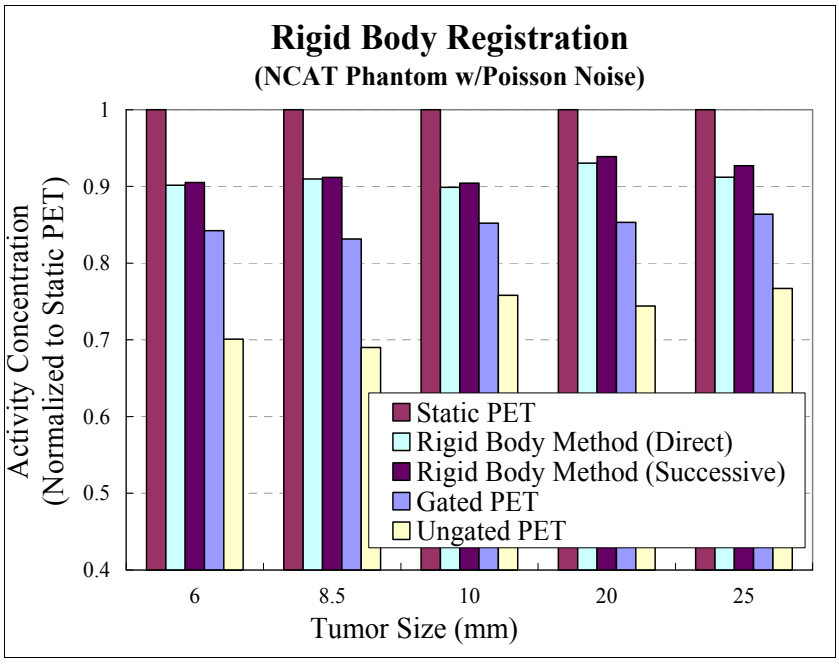
Rigid Body Registration
(NCAT Phantom w/Poisson Noise)
Activity Concentration
(Normalized to Static PET)
1
0.9
0.8
0.7
0.6
0.5
0.4
6
8.5
10
20
25
Tumor Size (mm)
Static PET
Rigid Body Method (Direct)
Rigid Body Method (Successive)
Gated PET
Ungated PET

(b)

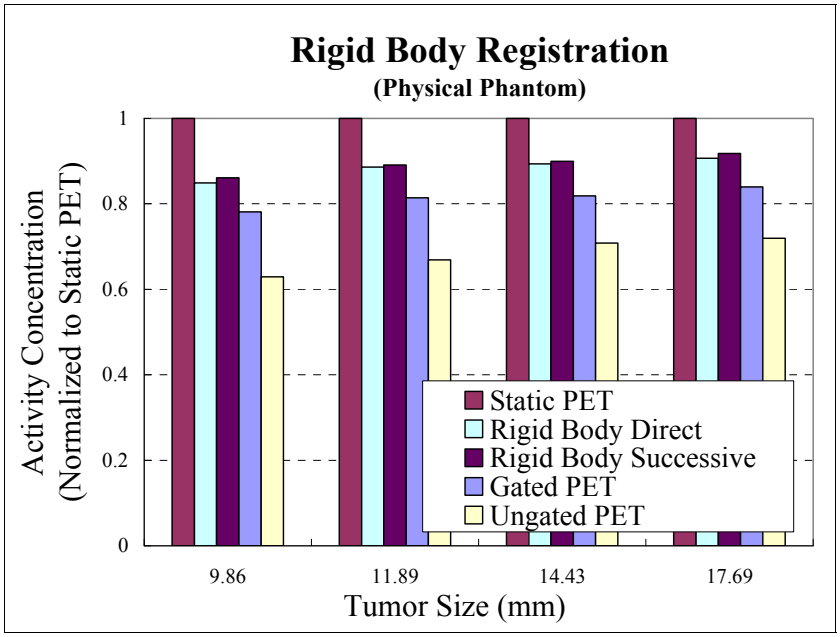

(c)

Figure 5.15 (a) NCAT phantom results with random noise, the error bars with 10 mm tumor simulations are for standard deviation, N=3. (b) NCAT phantom results with Poisson noise and (c) physical phantom results. Activity concentration of Rigid Body registration algorithms with Direct and Successive Scheme, static PET, gated PET and ungated PET images. All of the values are normalized to the static PET (gold standard). Here gated PET values come from the average value of all gated bin.

The results of the actual tumor size with the computed size of segmented tumors are shown in Table 5.4, to compare gated tumors (average of all gates) with registered tumors (with Rigid Body Direct Scheme and Rigid Body Successive Scheme).

Tumor diameter (mm)		**True Tumor Volume**	**Segmented Tumor Size**		
			Gated Tumor	**Rigid Body (Direct)**	**Rigid Body (Successive)**
NCAT Phantom (w/Poisson Noise)	6.0	17 pixels	20 pixels	20 pixels	20 pixels
	8.5	33 pixels	38 pixels	39 pixels	41 pixels
	10.0	44 pixels	48 pixels	46 pixels	48 pixels
	20.0	230 pixels	241 pixels	246 pixels	240 pixels
	25.0	409 pixels	424 pixels	420 pixels	424 pixels
NCAT Phantom (w/Gaussian Noise)	6.0	17 pixels	18 pixels	18 pixels	19 pixels
	8.5	33 pixels	36 pixels	34 pixels	38 pixels
	10.0	44 pixels	48 pixels	47 pixels	49 pixels
	20.0	230 pixels	239 pixels	237 pixels	240 pixels
	25.0	409 pixels	415 pixels	413 pixels	415 pixels

Physical Phantom	8.23	0.13 ml	/	/	/
	9.86	0.25 ml	0.48 ml	0.46 ml	0.44 ml
	11.89	0.50 ml	0.76 ml	0.76 ml	0.78 ml
	14.43	1.00 ml	1.17 ml	1.19 ml	1.22 ml
	17.69	2.00 ml	2.29 ml	2.26 ml	2.23 ml

Table 5.4 Results comparing the true tumor volume with the segmented tumor volume. / means the tumor is too small for the algorithm to identify.

Relative noise levels are also compared. Lower noise is achieved after registration as shown in Figure 5.16 for both the NCAT phantom and the physical phantom.

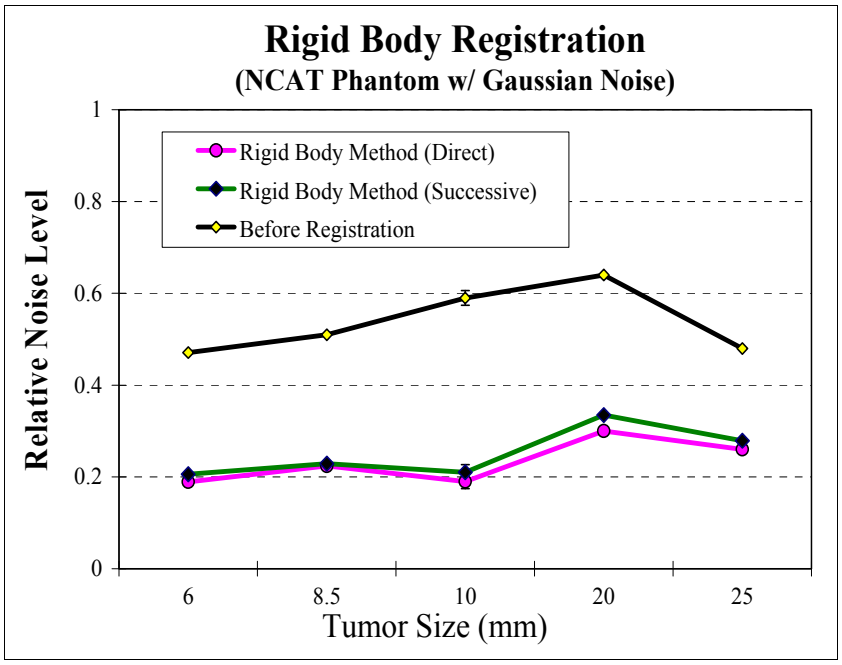

(a)

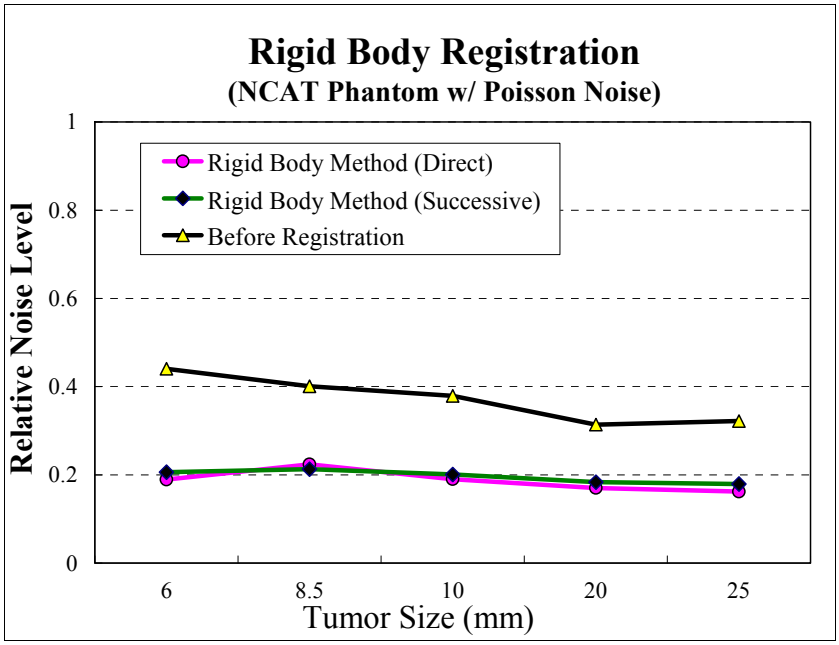

(b)

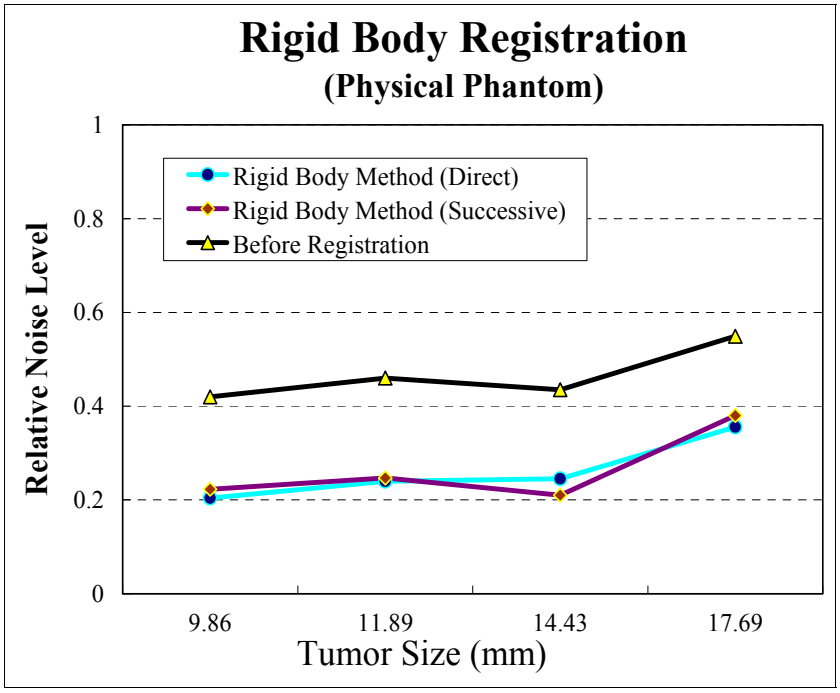

(c)

Figure 5.16 Comparing relative noise level before registration and after Intensity registration with direct and Successive Scheme: (a) NCAT phantom with Gaussian noise, the error bars with 10 mm tumor simulations are for standard deviation, N=3. (b) NCAT phantom with Poisson noise, (c) Physical phantom.

5.3.4 Optical Flow Based Registration

Figure 5.14 shows the cross-correlation results of the NCAT phantom and the physical phantom using Optical Flow registration with Direct and Successive Schemes; similar results as the two other registration methods before were obtained.

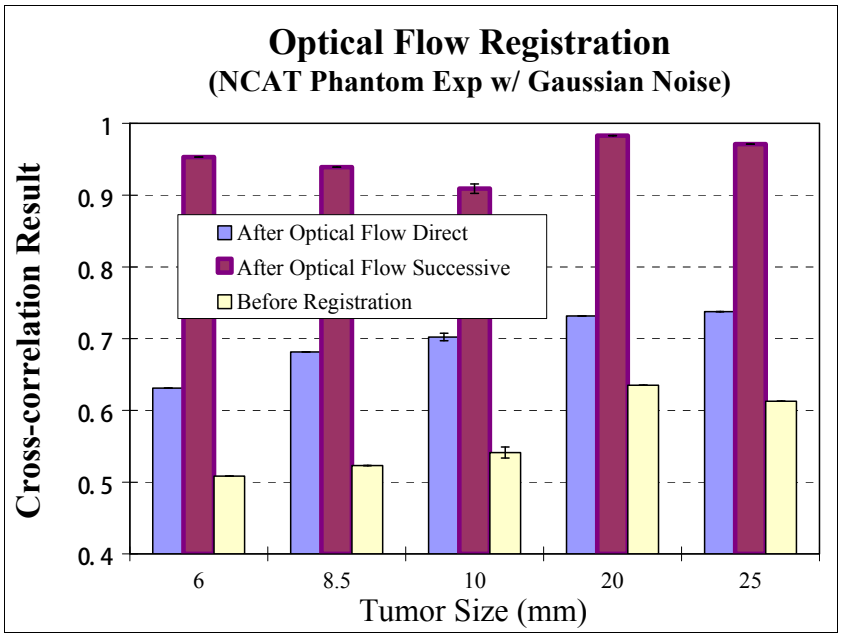

(a)

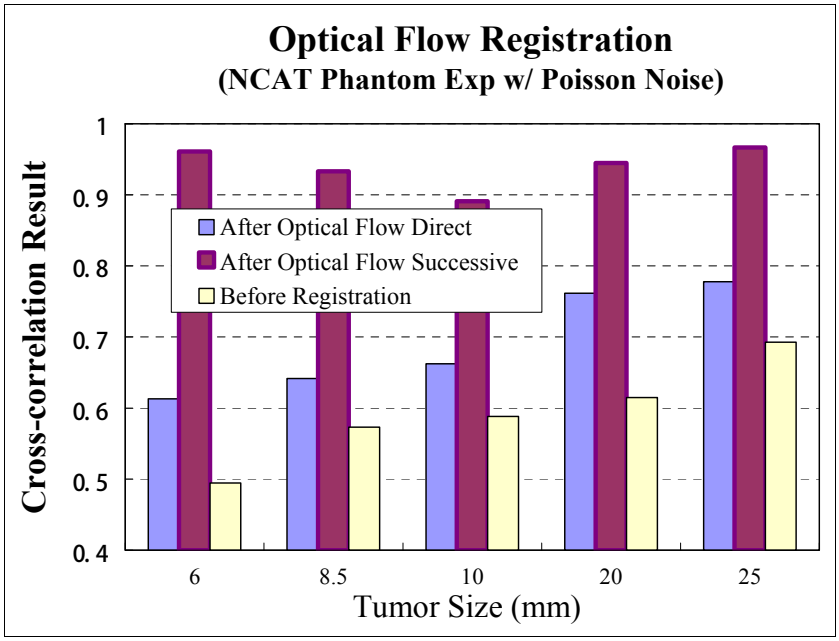

(b)

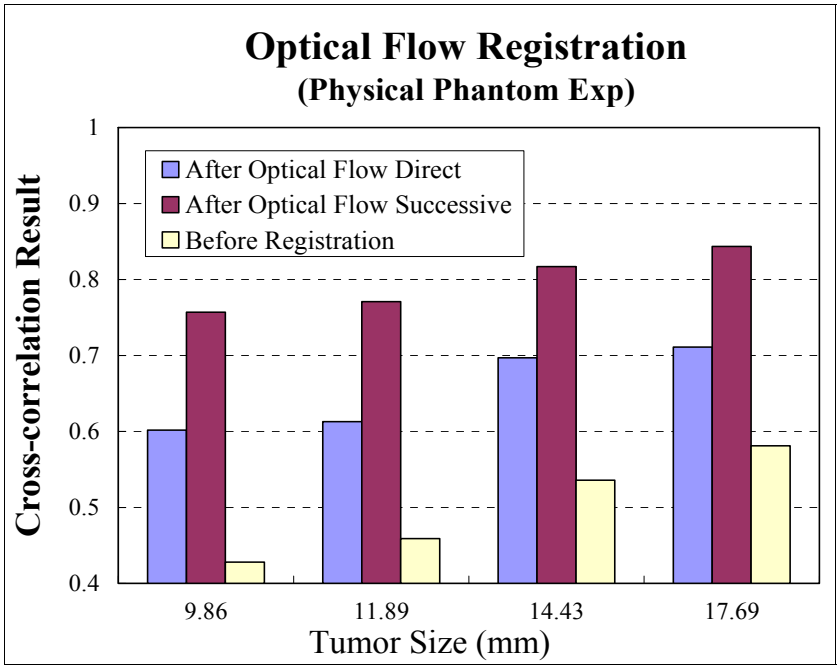

(c)

Figure 5.17 (a) Cross-correlation results of NCAT phantom with Gaussian noise simulated for 5 different size tumors using Optical Flow registration algorithm, before registration comparing to after Direct Scheme and Successive Scheme. The error bars with 10 mm tumor simulations are for standard deviation, N=3. (b) Cross-correlation results of NCAT phantom with Poisson noise simulated (c) Cross-correlation results of physical phantom for 4 different size tumors.

The quantitative results of activity concentration are also evaluated with reference to the static PET, non-gated PET and non-registered gated PET as shown in Figure 5.18 below. Here the activity concentration is calculated as the average activity over the entire tumor region, and then the values are normalized to the static PET value (which is the gold standard for comparison).

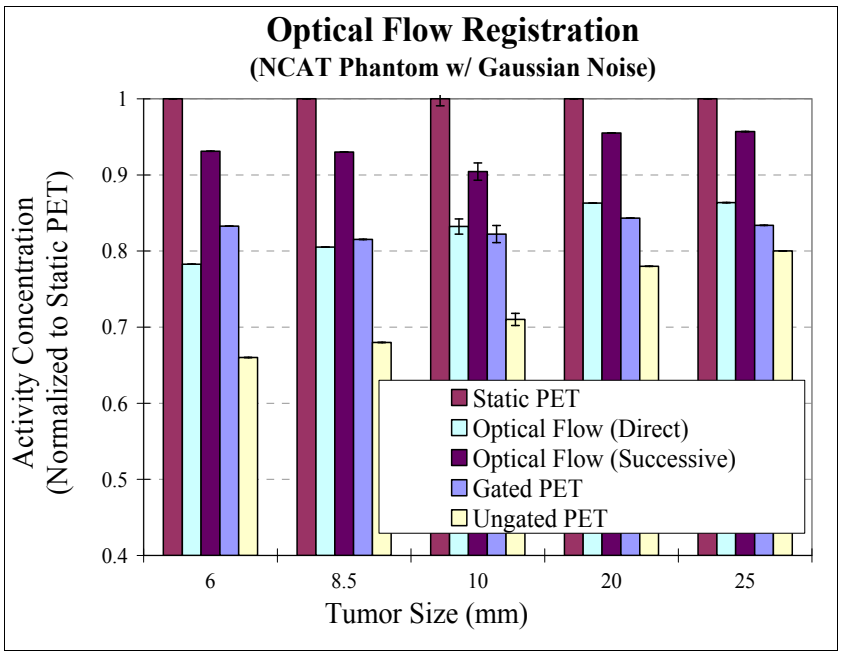
Optical Flow Registration
(NCAT Phantom w/ Gaussian Noise)
Activity Concentration
(Normalized to Static PET)
1
0.9
0.8
0.7
0.6
0.5
0.4
6
8.5
10
20
25
Tumor Size (mm)
Static PET
Optical Flow (Direct)
Optical Flow (Successive)
Gated PET
Ungated PET

(a)

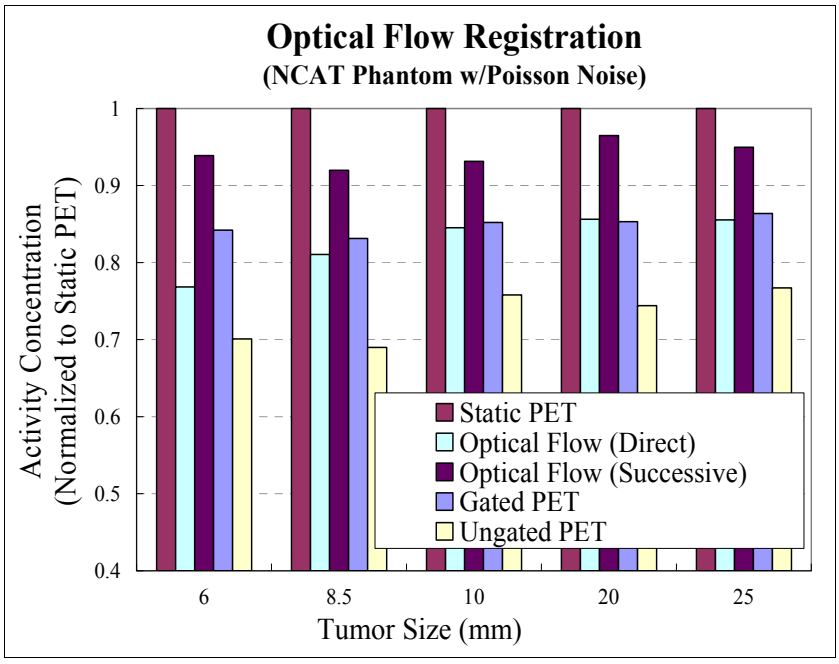
Optical Flow Registration
(NCAT Phantom w/Poisson Noise)
Activity Concentration
(Normalized to Static PET)
1
0.9
0.8
0.7
0.6
0.5
0.4
6
8.5
10
20
25
Tumor Size (mm)
Static PET
Optical Flow (Direct)
Optical Flow (Successive)
Gated PET
Ungated PET

(b)

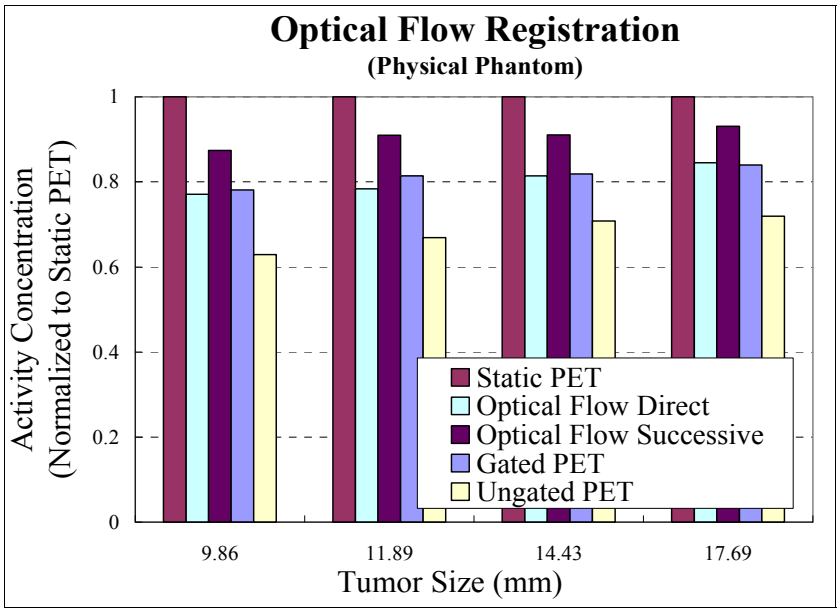

(c)

Figure 5.18 (a) NCAT phantom with Gaussian noise results, the error bars with 10 mm tumor simulations are for standard deviation, N=3. (b) NCAT phantom with Poisson noise results and (c) physical phantom results, activity concentration of Rigid Body registration algorithms with Direct and Successive Scheme, static PET, gated PET and ungated PET images. All of the values are normalized to the static PET (gold standard). Here gated PET values come from the average value of all gated bin.

The results of the actual tumor size with the computed size of segmented tumors are shown in Table 5.5, which compares gated tumors (average of all gates) with registered tumors (with Optical Flow Direct Scheme and Optical Flow Successive Scheme).

Tumor diameter (mm)		**True Tumor Volume**	**Segmented Tumor Size**		
			Gated Tumor	**Optical Flow (Direct)**	**Optical Flow (Successive)**
NCAT Phantom (w/Poisson Noise)	6.0	17 pixels	20 pixels	23 pixels	20 pixels
	8.5	33 pixels	38 pixels	43 pixels	38 pixels
	10.0	44 pixels	48 pixels	56 pixels	50 pixels
	20.0	230 pixels	241 pixels	267 pixels	247 pixels
	25.0	409 pixels	424 pixels	438 pixels	420 pixels
NCAT Phantom (w/Gaussian Noise)	6.0	17 pixels	18 pixels	22 pixels	19 pixels
	8.5	33 pixels	36 pixels	40 pixels	34 pixels
	10.0	44 pixels	48 pixels	52 pixels	48 pixels
	20.0	230 pixels	239 pixels	253 pixels	233 pixels
	25.0	409 pixels	415 pixels	431 pixels	410 pixels
Physical	8.23	0.13 ml	/	/	/

Phantom	9.86	0.25 ml	0.48 ml	0.50 ml	0.46 ml
	11.89	0.50 ml	0.76 ml	0.81 ml	0.76 ml
	14.43	1.00 ml	1.17 ml	1.27 ml	1.20 ml
	17.69	2.00 ml	2.29 ml	2.36 ml	2.21 ml

Table 5.5 Results comparing the true tumor volume with the segmented tumor volume. / means the tumor is too small for the algorithm to identify.

Relative noise levels are also compared. Lower noise is achieved after registration as shown in Figure 5.19 for both NCAT phantom and physical phantom.

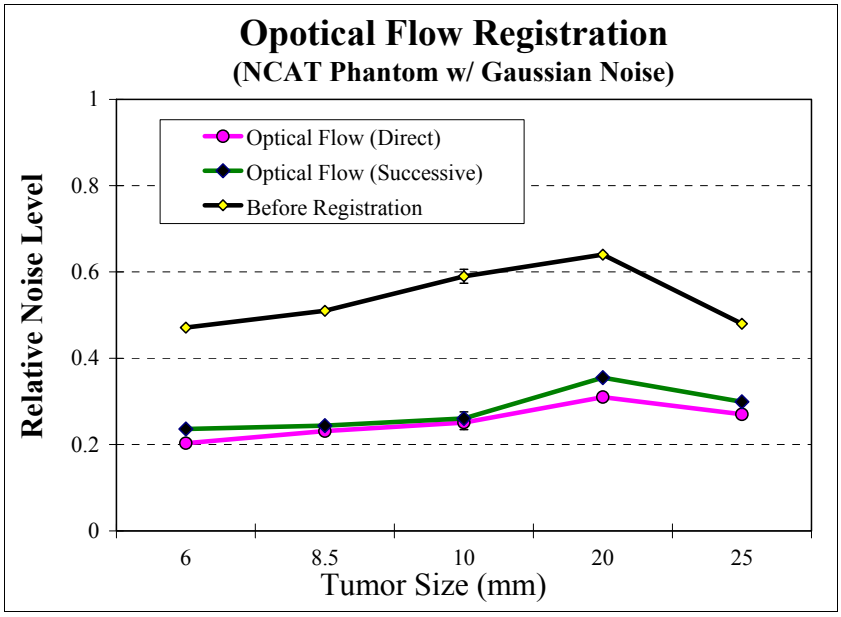

(a)

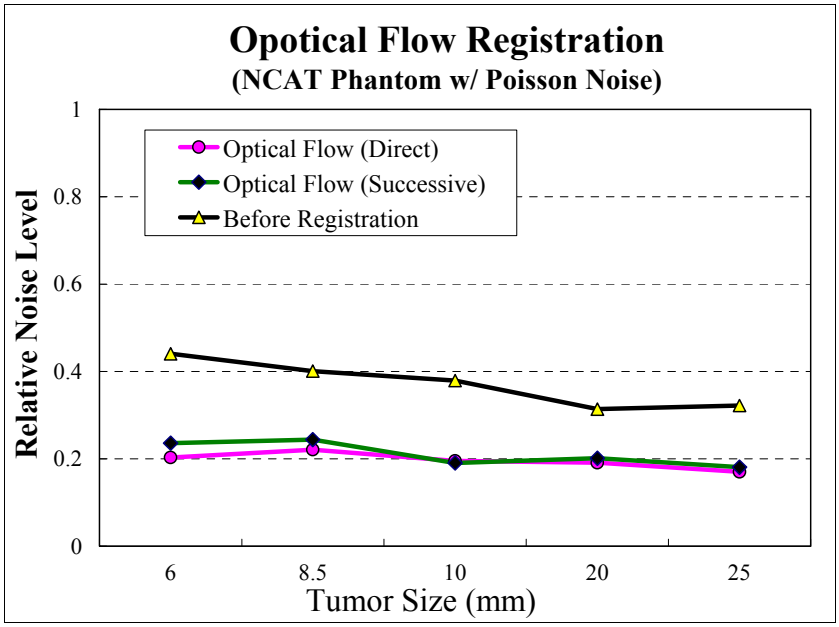

(b)

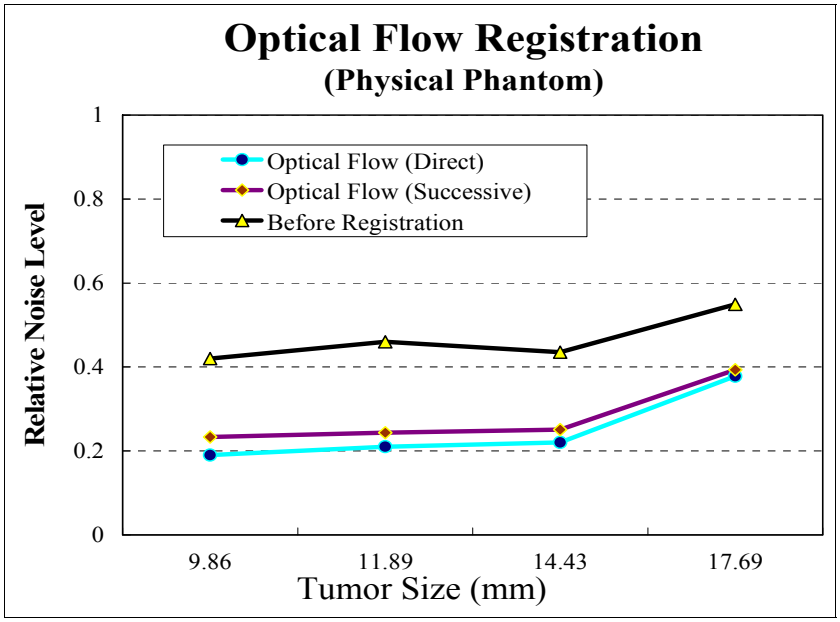

(c)

Figure 5.19 Comparing relative noise level before registration and after Intensity registration with direct and Successive Scheme: (a) NCAT phantom with Gaussian noise, the error bars with 10 mm tumor simulations are for standard deviation, N=3. (b) NCAT phantom with Poisson noise, (c) Physical phantom.

5.3.5 Comparison of Four Registration Methods

The comparison of four registration methods and two registration schemes are displayed in Figure 5.20 below for cross-correlation coefficient results. The difference in improvement after all these motion correction algorithms can be seen.

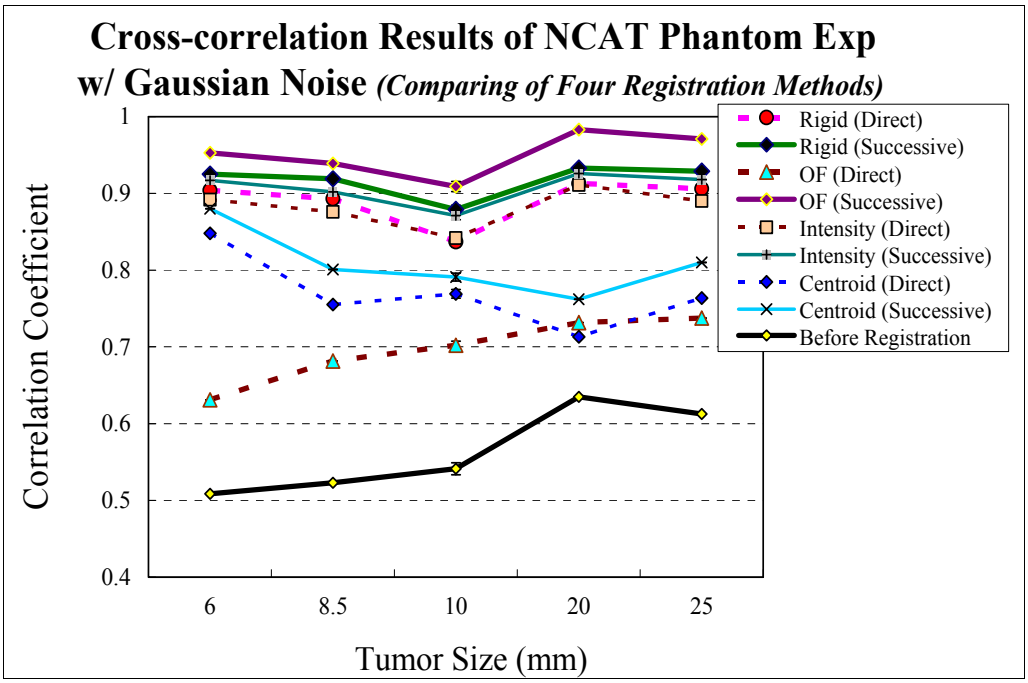
Cross-correlation Results of NCAT Phantom Exp
w/ Gaussian Noise (Comparing of Four Registration Methods)
Correlation Coefficient
1
0.9
0.8
0.7
0.6
0.5
0.4
6
8.5
10
20
25
Tumor Size (mm)
Rigid (Direct)
Rigid (Successive)
OF (Direct)
OF (Successive)
Intensity (Direct)
Intensity (Successive)
Centroid (Direct)
Centroid (Successive)
Before Registration

(a)

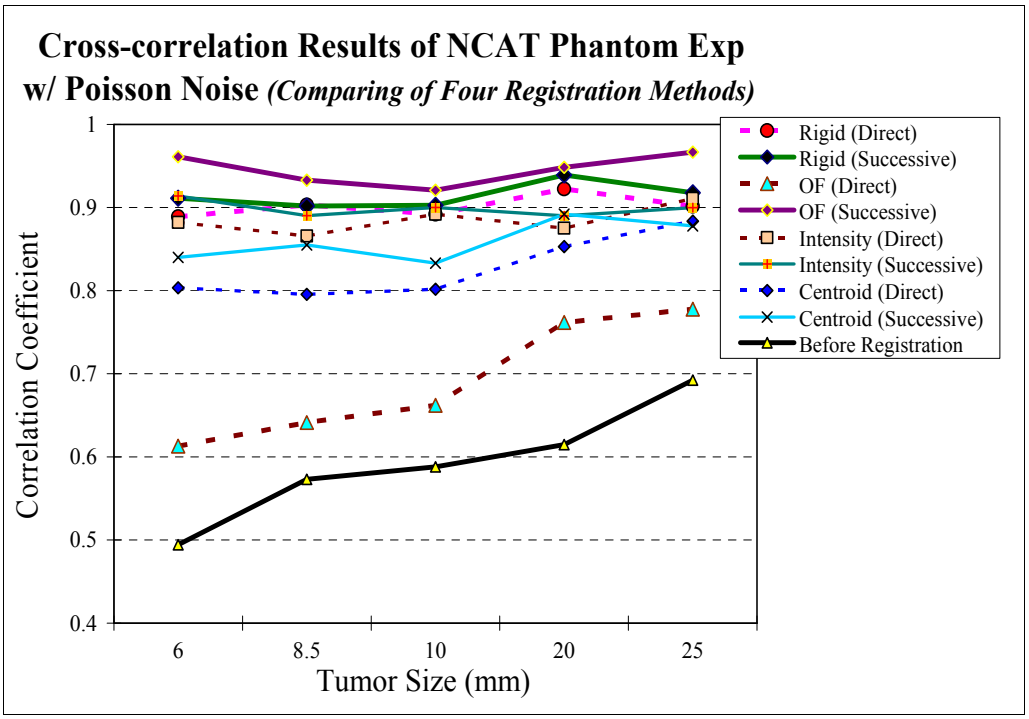
Cross-correlation Results of NCAT Phantom Exp
w/ Poisson Noise (Comparing of Four Registration Methods)
Correlation Coefficient
1
0.9
0.8
0.7
0.6
0.5
0.4
6
8.5
10
20
25
Tumor Size (mm)
Rigid (Direct)
Rigid (Successive)
OF (Direct)
OF (Successive)
Intensity (Direct)
Intensity (Successive)
Centroid (Direct)
Centroid (Successive)
Before Registration

(b)

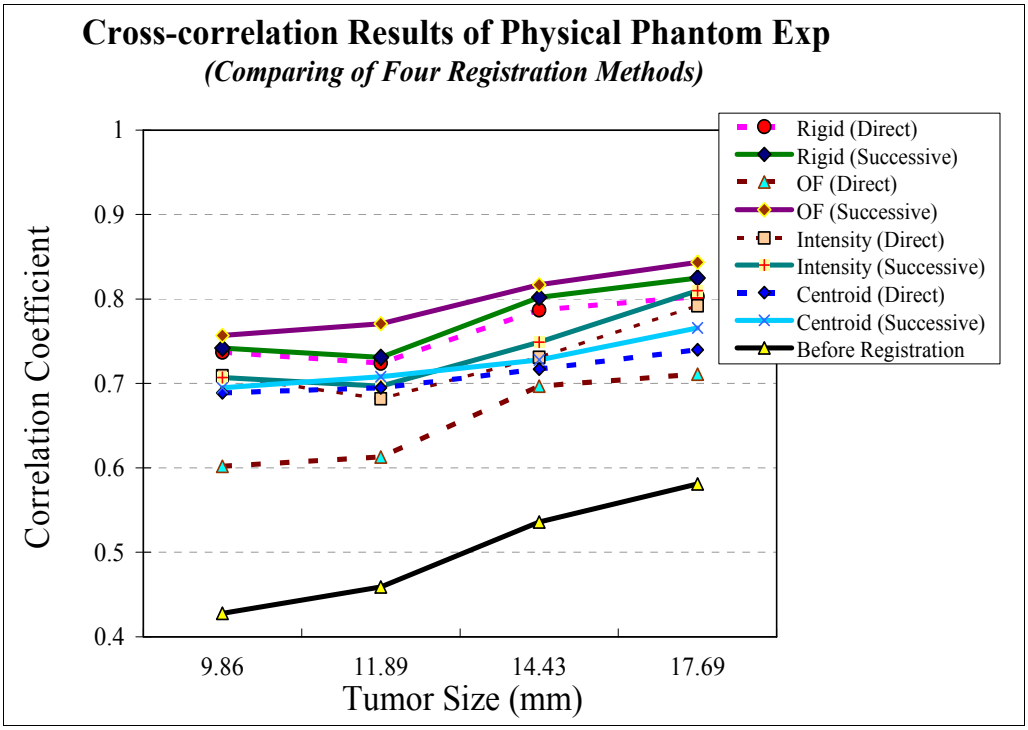

(c)

Figure 5.20 Cross-correlation results comparing four registration methods and two registration schemes, (a) NCAT phantom with Gaussian noise, the error bars with 10 mm tumor simulations are for standard deviation, N=3. (b) NCAT phantom with Poisson noise. (c) physical phantom. Here OF is the short of Optical Flow.

The comparison of all four registration methods and two registration schemes in average activity concentrations are displayed in Figure 5.21 below.

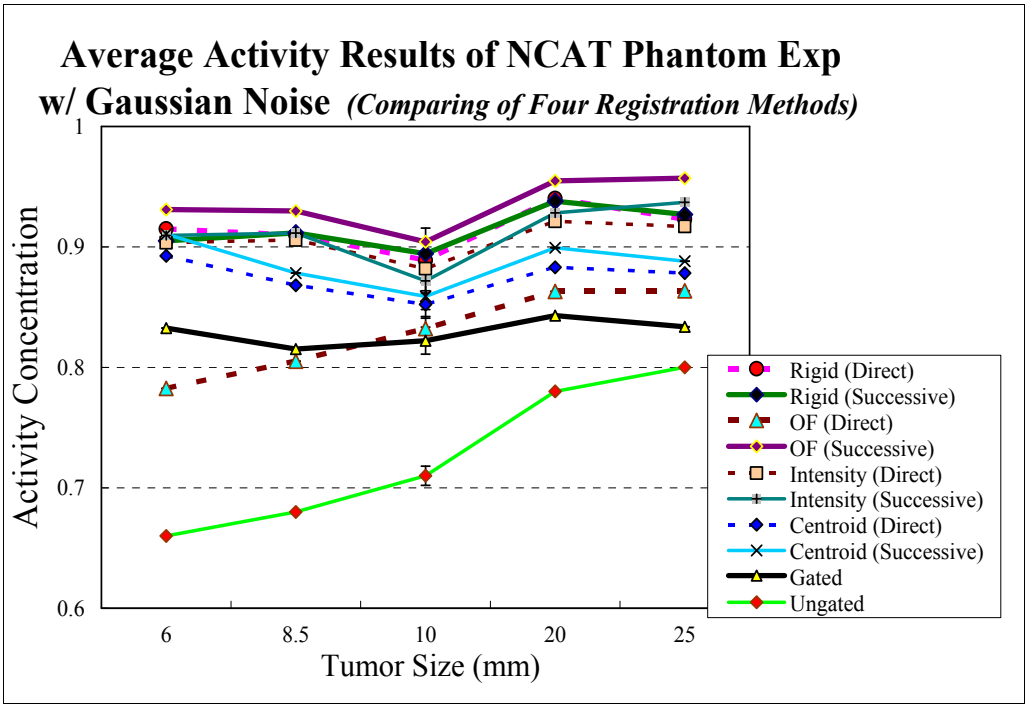
Average Activity Results of NCAT Phantom Exp
w/ Gaussian Noise (Comparing of Four Registration Methods)
Activity Concentration
1
0.9
0.8
0.7
0.6
6
8.5
10
20
25
Tumor Size (mm)
Rigid (Direct)
Rigid (Successive)
OF (Direct)
OF (Successive)
Intensity (Direct)
Intensity (Successive)
Centroid (Direct)
Centroid (Successive)
Gated
Ungated

(a)

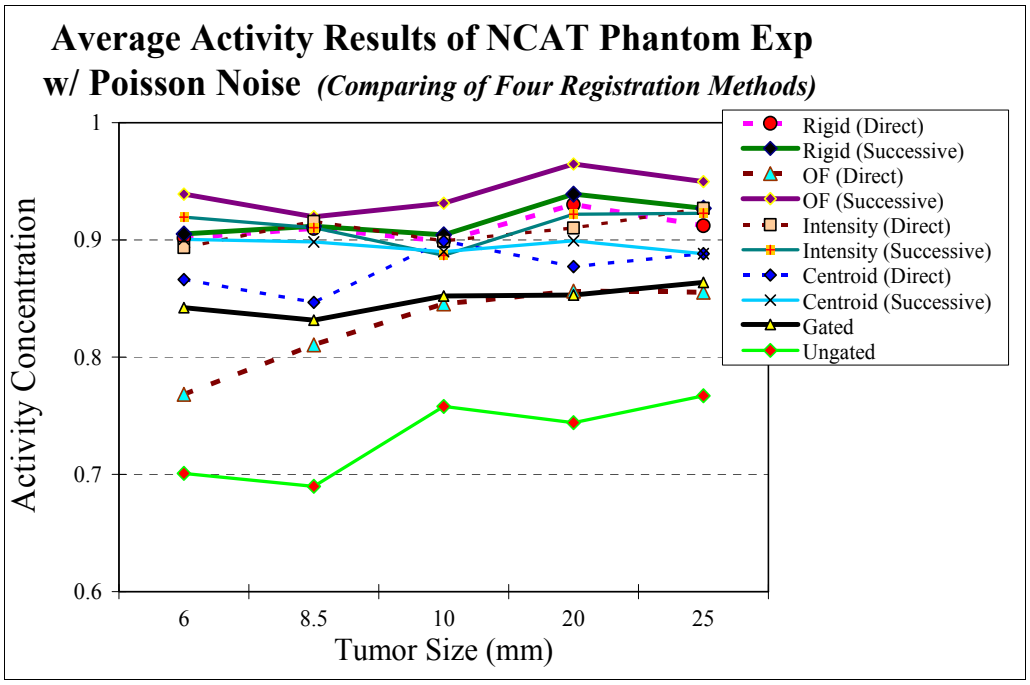
Average Activity Results of NCAT Phantom Exp
w/ Poisson Noise (Comparing of Four Registration Methods)
Activity Concentration
1
0.9
0.8
0.7
0.6
6
8.5
10
20
25
Tumor Size (mm)
Rigid (Direct)
Rigid (Successive)
OF (Direct)
OF (Successive)
Intensity (Direct)
Intensity (Successive)
Centroid (Direct)
Centroid (Successive)
Gated
Ungated

(b)

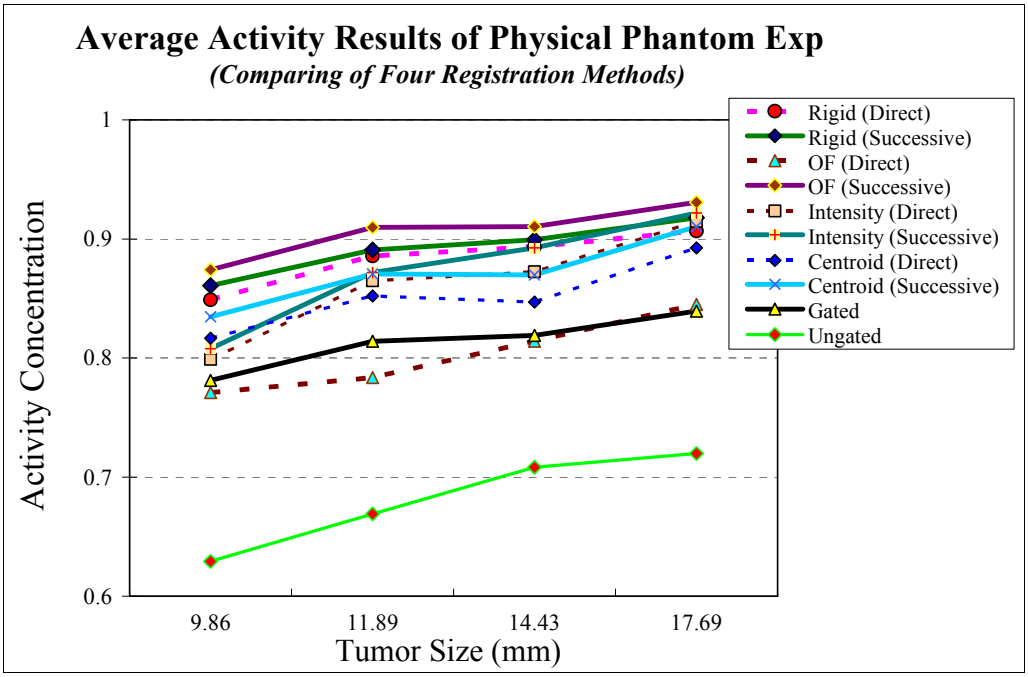

(c)

Figure 5.21 Average activity concentration results comparing four registration methods and two registration schemes, (a) NCAT phantom with Gaussian noise, the error bars with 10 mm tumor simulations are for standard deviation, N=3. (b) NCAT phantom with Poisson noise, (c) physical phantom. Here OF is the short of Optical Flow.

Relative noise levels are compared for four registration methods and two registration schemes in Figure 5.22. In terms of noise reduction, all these eight methods appear to be similar.

The computation time of four registration methods and two registration schemes are shown in Table 5.6. The computer to run all these algorithms is Intel Core 2 Duo @ 1.40 GHz, 2GB memory. It can bee seen that Centroid and Intensity methods require the least processing time, while the Optical Flow with Successive Scheme is most time consuming.

Computation Time (Second)	Centroid	Intensity	Rigid Body	Optical Flow
Direct	10.3	10.1	29.5	195.0
Successive	28.6	28.1	81.9	541.4

Table 5.6 Comparing of processing time for four registration methods and two registration schemes.

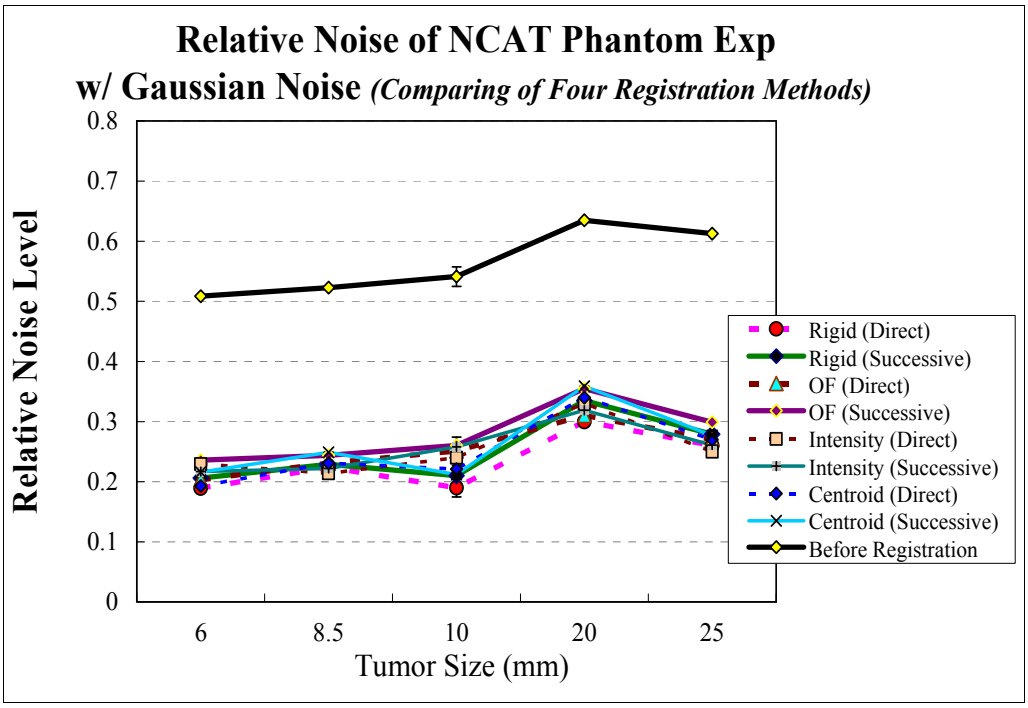

(a)

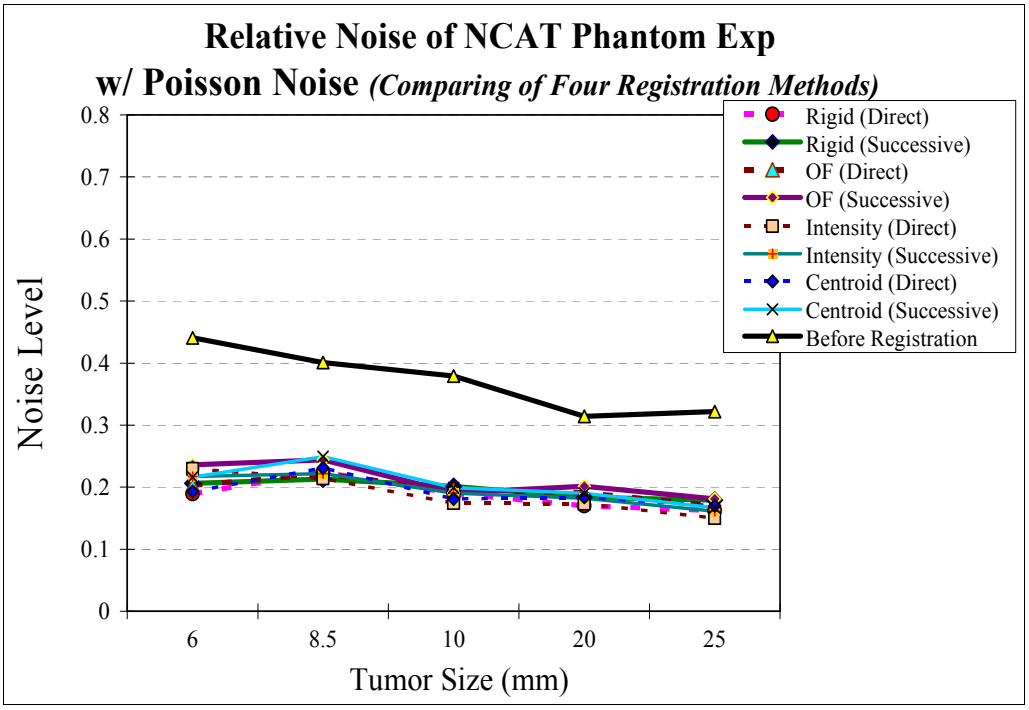

(b)

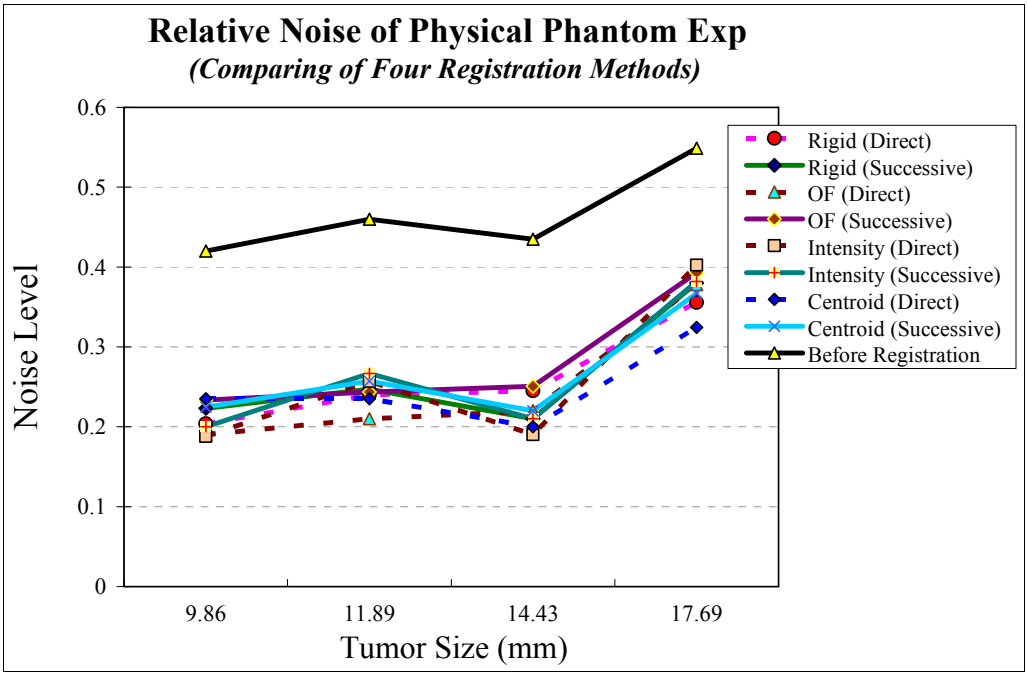

(c)

Figure 5.22 Results of relative noise comparing four registration methods and two registration schemes, (a) NCAT phantom with Gaussian noise, the error bars with 10 mm tumor simulations are for standard deviation, N=3. (b) NCAT phantom with Poisson noise , (c) physical phantom.

The sensitivity of noise for the four registration methods was tested by applying twice and three times noise level on NCAT phantom with random noise, and the results of percentage degradation in the cross-correlation result after noise are shown in Figures 5.23 below.

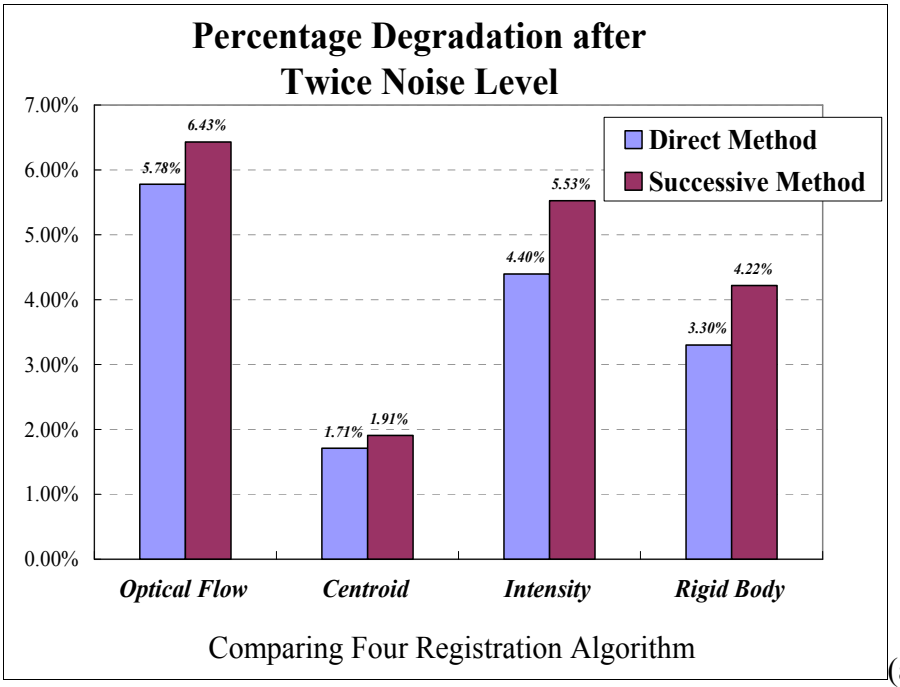

(a)

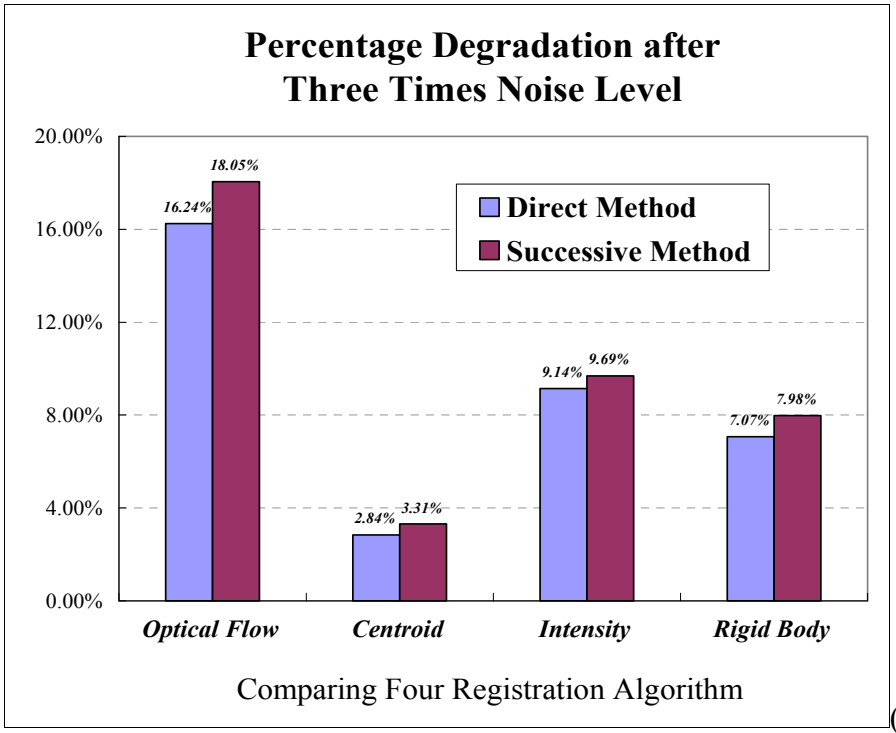

(b)

Figure 5.23 Percentage degradation in cross-correlation result after (a) applying twice noise and (b) applying three times noise with NCAT phantom

6. DISCUSSIONS

Improving the detectability of a malignant lung tumor in its initial stage will positively impact lung cancer patient care, which is a major health problem in the United States. For lung cancer detection, ^{18}FDG-PET has been proven to have a higher sensitivity than CT [2]. However, because of the long duration of whole body PET scans, tumor and organ motion due to respiration can be a major challenge for accurate localization and quantification of ^{18}PET-FDG images as the image will be blurred and the tumor smeared. The long-term goal of this research is to increase the sensitivity and prognostic value of molecular imaging with ^{18}FDG-PET/CT of small malignant lung tumors that move significantly during respiration, and to improve the identification and accuracy of ^{18}FDG uptake quantitation of small tumors. The overall goal of this study is to develop and validate a simple and practical solution to the problem of respiratory motion for the precise interpretation and quantitation of ^{18}FDG uptake of lung PET images.

Several papers appeared in recent years describing different image processing algorithms compensating for motion artifacts. There are comprehensive review papers of motion correction methods in PET by Rahmim [58], Nehmeh et al[87] and by Visvikis et al[44]. Qiao et al [62] achieved motion correction by successfully applying non-rigid motion compensation to computer simulated list-mode PET data; similarly, Lamare et al [61], Livieratos et al [88] also apply affine transformation to list-mode PET data. These correction approaches are performed during reconstruction process based on the list mode raw data, which is also a very promising area, however, as list mode collection is not generally implemented on clinical cameras, it is probably a limiting obstacle, also it requires more memory storage and processing time while our method is a post-

reconstruction algorithm (in image domain), applicable to existing clinical reconstructions and is likely more computationally feasible. Deconvolution has been reported to correct lung motion artifact with positive results [63]. An accurate estimation of respiratory motion from 4D CT images is required before performing the deconvolution, which is one limitation; also deconvolution itself tends to amplify the noise in real noisy PET data. Another attempt to solve to problem proposed by Dawood et al [66] utilizes a global optical flow algorithm for motion correcting images in individual gates. The method uses four assumptions to perform the deformable registration: intensity similarity, incremental transformation, smoothness, and error minimization, which could suffer from inaccuracy in the presence of high noise. Also the work from Thorndyke et al [67] corrects motion through retrospective stacking, where the entire data is stacked on top of one another to form a composite image. Most of these current correction approaches derive registration information from the entire image sequence of the moving object. Due to the elastic nature of the chest region, an elastic/deformable motion model is often required to characterize the respiratory movement. These elastic image registration approaches generally involve an optimization process over a large number of parameters, which could lead to lengthy computation time. In addition, the complexity of the movement within the chest and abdomen region often makes it difficult to achieve accurate registration for each image voxel position. It is often the case when applying deformable image registration to a large image region that, although the overall structures of the registered images can be reasonably aligned, some mis-matches at local detail levels are still present even after a lengthy optimization process. These mis-matches would then cause inaccurate motion compensation for the

corresponding image features, and would have adverse effects if those features are of interest.

Different from these "whole-image" approaches, our algorithm intends to improve the speed and accuracy in estimating respiratory motion. We aim at a more general and practical solution to this problem by limiting our efforts to the "local region": the segmented tumor part only, which is the region of most interest. Our work has some similarity to another paper by Qiao et al [64] using region of interest (ROI) motion compensation by incorporating motion information within that region into the system model, this will enable faster extraction of motion information, but they require manually selecting the ROI, while in our algorithm the tumor region can be automatically localized and identified. Unlike registering the entire image set, the "local" image registration only requires a simplified model to describe the motion (e.g., a centroid-based model, rigid body model with a few number of degrees of freedom). The fewer free parameters associated with the motion model and the reduced number of image voxels to be considered both contribute to the speedup of the image registration process compared with entire image registration methods. The local image registration method also has the potential to improve registration accuracy within the "local" region when considering the following aspects: the registration algorithm only focuses on the alignment of image contents within the tumor region, and would not be disturbed by other irrelevant image features; the optimization process would be more robust due to the reduced dimensions of the parameter space.

The innovative aspect of this project is to develop a computer-assisted motion track and integration algorithm that includes all the counts collected in the respiratory cycle into

solely one reference bin. This method has the advantages: (1) the automatic track algorithm would simplify the calculations as the following integration algorithm will only be performed on the segmented tumor region; (2) PET scan time doesn't need to be increased as the integration process will reduce statistical noise and increase signal-to-noise ratio. The integration of the information of different time bins into one set of tomographic slices would facilitate the 3D quantitation of activity and the introduction of the procedure to the clinical practice. It could make the clinical interpretation of lung tumor ^{18}FDG-PET scans easier, faster and more reproducible.

The validation of the algorithm was performed on a simulated NCAT computer phantom and a dynamic physical phantom. One assumption about the simulated tumor is that the tumor is rigid and will move as a whole, there will be no deformation or change inside the tumor between each gated bins. Phantom studies often provide insight that is difficult or impossible to obtain, by using pre-defined, controlled parameters, and avoiding any un-controlled scanner- or patient-specific variability. Moreover, we know the "gold standard" in these cases, so that algorithm results can be compared to optimal goals under a wide range of well-defined conditions. In the future, these phantoms can also be implemented into related imaging research studies such as respiratory gating hardware design and acquisition protocol development.

The experiments with both the NCAT software phantoms (with Gaussian noise and with Poisson noise) as well as with the physical phantom showed significant improvement in motion corrected data. Several independent criteria were selected to assess the improvement. For tumor activity concentration, the activity values are closer to the static tumor (real value) with reference to the ungated PET after all four registration methods

(except Optical Flow with Direct Scheme) (Figure 5.21), with improvements of 9.2%, 6.5%, 10.1% and 0.1% for Intensity Registration, Centroid Registration, Rigid Body Registration and Optical Flow Registration with Direct Scheme respectively, and improvements of 9.7%, 7.9%, 10.3% and 12.8% for Intensity Registration, Centroid Registration, Rigid Body Registration and Optical Flow Registration with Successive Scheme respectively. For cross-correlation coefficient as shown in Figure 5.20, with Direct Scheme the average improvements of 27.7%, 19.2%, 29.6% and 13.8% were achieved with Intensity, Centroid, Rigid Body and Optical Flow method respectively. With Successive Scheme the average improvements of 29.4%, 22.3%, 31.8% and 36.6% were achieved with Intensity, Centroid, Rigid Body and Optical Flow method respectively. In the Optical Flow method, Successive Scheme improved 22.8% comparing with Direct Scheme, while for the other methods the improvements of the Successive Scheme were very small.

Figure 5.22 demonstrates the analysis of noise reduction on the PET data, which is an indicator of the image quality and supports the conclusion from Chapter 4.5.1, that motion correction improves the SNR to ungated PET Data. For example, the average noise level in the NCAT phantom gated images is 0.518, and that for the data after Rigid Body registration it is 0.241, which is similar to the ungated data, 0.225. There is not a large difference between these four methods. An average reduction of 25.6%, 25.1%, 23.9% and 24.8% in noise level was achieved for Intensity Registration, Centroid Registration, Rigid Body Registration and Optical Flow Registration with the Direct Scheme respectively, and an average of 24.1%, 23.7%, 23.1% and 21.9% in noise level reduction was achieved for Intensity Registration, Centroid Registration, Rigid Body

Registration and Optical Flow Registration with Successive Scheme respectively. The slightly higher noise level with the Successive Scheme compared with the Direct Scheme is probably due to more interpolation steps performed during motion correction.

The simulation of NCAT phantom with Gaussian noise using the 10 mm tumors was repeated three times to simulate statistical experiment variability. The changes is minimal as can be seen from the results of cross coefficients, activity concentration and relative noise levels, the standard deviations between these results are within 3%.

Two registration schemes were also compared: Direct Scheme vs. Successive Scheme. For Intensity Registration, Centroid Registration and Rigid Body Registration, average improvement of 1.7%, 3.1% and 2.2% in correlation coefficient after applying the Successive Scheme were observed, respectively. Similar small improvements of activity concentration of 0.5%, 1.4% and 0.3%, respectively, were observed. The improvement of the Successive Scheme compared with the Direct Scheme is minimal but it requires much more computational time and more interpolation steps, so it appears unnecessary to use the Successive Scheme for these three methods. For the Optical Flow method, it is obvious that the Successive Scheme is superior to the Direct Scheme, as there is a 21.1% improvement in the cross correlation coefficient and a 12.7% improvement in the activity concentration. This is because the optical flow algorithm can calculate the motion field with smaller displacement much more accurately than large displacement.

The optical flow algorithm differs from other deformable registration methods in its ease of use as no user intervention is required to select matching control pixels and its precision in mapping the images. The Horn-Schunk method [85] uses spatio-temporal derivatives of the evolving image brightness function to determine the optical flow, the

assumption is made that the brightness of any part of the image changes very slowly and smoothly, which makes the algorithm very vulnerable when the images are very noisy. The comparison of all of the methods' sensitivity to noise is demonstrated in Figures 5.23 and 5.24 showing that the Optical Flow method is most sensitive to noise, while the other methods perform better in case of high noise level.

In all the experiments with the NCAT computer phantom and the physical phantom, the tumors are always simulated as sphere shape. Possible degradation in the results could occur when implementing the algorithms with real irregular shaped tumors, as the rough boundaries are more sensitive to noise, and it will become more difficult for the algorithm to distinguish the tumor voxels from noise voxels. It is noticed that the results from the NCAT computer phantom are much better than the results from the physical phantom. Even after the Gaussian/Poisson distributed noise was added into the NCAT phantom data, it is still too ideal compared with real physical phantom data. Scattering events, random coincidence events and attenuation are not included into the NCAT phantom. Also no correction was made for the partial volume effect. Another possible reason for the better NCAT results compared with physical phantom results is that the spatial resolution of the NCAT phantom images is 3.125 mm per pixel, which is much higher than the spatial resolution of physical phantom images (3.75 mm per pixel).

Incorporating attenuation correction was outside of the scope of this study. In this study all the image processing algorithms were performed on attenuation corrected PET data with physical phantom. Error could occur during the process of attenuation correction because only one snapshot of CT is taken during respiration while PET acquisition is a continuous process. Therefore, the CT images do not correlate exactly with the PET

images. This could only occur if they were acquired over the exact same period of the respiration. We have tried to minimize the error by selecting the reference PET bin as close as possible to match the CT transmission data with the highest correlation value, but the results cannot be validated unless 4D CT data is acquired. In future work, motion information could be extracted from non-attenuation-corrected image data sets, and then motion compensation applied to attenuation-corrected image data sets. In this way more accurate attenuation correction could be achieved.

Final verification and demonstration of feasibility should be performed using some retrospective and archived clinical PET studies. This will be a future goal of this project: patients with a SPN will be evaluated by experienced radiologists, and also the algorithm proposed in this research will do the same automatically without intervention of any operators. The follow up biopsy could also be performed if possible to verify the findings from the images. The quantification of the tumor and staging of the lung cancer should match the radiologists' diagnosis.

7. CONCLUSIONS

In this research project, we developed and evaluated a computer-assisted method that can automatically localize tumors in lung PET images of discrete bins within the breathing cycle, followed by an algorithm that integrated all the information of a complete respiratory cycle into a single reference bin. Validation and comparison of the algorithms were performed by conducting experiments on a computerized NCAT phantom and on a dynamic physical phantom. Iterations were conducted on different size simulated tumors and different noise levels. Comparing the results of the tumors before correction with after correction, the tumor activity values and tumor volumes are closer to the static tumors (gold standard). Higher correlation values and lower noise are also achieved after applying the correction algorithms.

Of the four registration methods and two registration schemes evaluated, the Optical Flow registration with Successive Scheme demonstrates the best correlation result but is more sensitive to noise. The Centroid based registration with Direct Scheme requires the least processing time but is less accurate than the other methods.

With these motion correction methods the compromise between short PET scan time and reduced image noise can be achieved. The automatic algorithm and practical procedure can be implemented in a busy clinical setting; it will allow accurate quantification of tumor functional volume and accurate three-dimensional quantitative analysis of tumor activity concentration, making the clinical analysis precise and fast.

REFERENCES

[1] A. Jemal, R. Siegel, E. Ward, Y. Hao, J. Xu, T. Murray, and M. J. Thun, "Cancer statistics, 2008," *CA: a cancer journal for clinicians*, vol. 58, pp. 71-96, 2008.

[2] J. A. Christensen, M. A. Nathan, B. P. Mullan, T. E. Hartman, S. J. Swensen, and V. J. Lowe, "Characterization of the solitary pulmonary nodule: 18F-FDG PET versus nodule-enhancement CT," *American Journal of Roentgenology*, vol. 187, pp. 1361-1367, 2006.

[3] R. J. Jackman, C. A. Good, O. T. Clagett, and L. B. Woolner, "Survival rates in peripheral bronchogenic carcinomas up to four centimeters in diameter presenting as solitary pulmonary nodules," *J Thorac Cardiovasc Surg*, vol. 57, pp. 1-8, 1969.

[4] N. Martini, M. S. Bains, M. E. Burt, M. F. Zakowski, P. McCormack, V. W. Rusch, and R. J. Ginsberg, "Incidence of local recurrence and second primary tumors in resected stage I lung cancer," *J Thorac Cardiovasc Surg*, vol. 109, pp. 120-9, 1995.

[5] C. A. Yi, K. S. Lee, B. T. Kim, J. Y. Choi, O. J. Kwon, H. Kim, Y. M. Shim, and M. J. Chung, "Tissue characterization of solitary pulmonary nodule: comparative study between helical dynamic CT and integrated PET/CT," vol. 47: Soc Nuclear Med, 2006, pp. 443-450.

[6] K. Mori, N. Niki, T. Kondo, Y. Kamiyama, T. Kodama, Y. Kawada, and N. Moriyama, "Development of a novel computer-aided diagnosis system for automatic discrimination of malignant from benign solitary pulmonary nodules on thin-section dynamic computed tomography," *Journal of computer assisted tomography*, vol. 29, pp. 215, 2005.

[7] Y. Nakamoto, M. Osman, C. Cohade, L. T. Marshall, J. M. Links, S. Kohlmyer, and R. L. Wahl, "PET/CT: comparison of quantitative tracer uptake between germanium and CT transmission attenuation-corrected images," *J Nucl Med*, vol. 43, pp. 1137-43, 2002.

[8] M. N. Gurcan, B. Sahiner, N. Petrick, H. P. Chan, E. A. Kazerooni, P. N. Cascade, and L. Hadjiiski, "Lung nodule detection on thoracic computed tomography images: preliminary evaluation of a computer-aided diagnosis system," *Med Phys*, vol. 29, pp. 2552-8, 2002.

[9] Z. Zhu, B. M. Tsui, and W. Segars, "A Simulation Study of the Effect of Gating Scheme on Respiratory Motion Blurring in FDG Lung PET," *49th Annual meeting of the Society of Nuclear Medicine, Los Angeles, CA. J. Nucl. Med*, vol. 43, pp. 57, 2002.

[10] G. J. K. B.W. Reutter, K.M. Brennan, "Acquisition and automated 3-D segmentation of respiratory/vcardiac-gated PET transmission images.," *IEEE Nuclear Science Symposium and Medical Imaging Conference*, vol. 1357-1361, 1996.

[11] S. V. J.M. Franquiz, G. Soler, "Computer-aided lung nodule detection and assessment by using a hybrid PET/CT scanner. Accepted for publication," *Proceedings of Medical Imaging 2004, SPIE code number 5369-49. San Diego, CA*, 2004.

[12] D. E. Midthun, "Solitary pulmonary nodule: time to think small," *Curr Opin Pulm Med*, vol. 6, pp. 364-70, 2000.

[13] J. M. Franquiz and S. Shukla, "A multiresolution restoration method for cardiac SPECT imaging," *Med Phys*, vol. 25, pp. 2469-75, 1998.

[14] P. Touliopoulos and P. Costello, "Helical (spiral) CT of the thorax," *Radiol Clin North Am*, vol. 33, pp. 843-61, 1995.

[15] H. Toomes, A. Delphendahl, H. G. Manke, and I. Vogt-Moykopf, "The coin lesion of the lung. A review of 955 resected coin lesions," *Cancer*, vol. 51, pp. 534-7, 1983.

[16] C. S. Yap, J. Czernin, M. C. Fishbein, R. B. Cameron, C. Schiepers, M. E. Phelps, and W. A. Weber, "Evaluation of Thoracic Tumors With 18F-Fluorothymidine and 18F-Fluorodeoxyglucose-Positron Emission Tomography," vol. 129: Am Coll Chest Phys, 2006, pp. 393-401.

[17] Y. Demura, T. Tsuchida, T. Ishizaki, S. Mizuno, Y. Totani, S. Ameshima, I. Miyamori, M. Sasaki, and Y. Yonekura, "18F-FDG accumulation with PET for differentiation between benign and malignant lesions in the thorax," *J Nucl Med*, vol. 44, pp. 540-8, 2003.

[18] R. J. Hicks, V. Kalff, M. P. MacManus, R. E. Ware, A. Hogg, A. F. McKenzie, J. P. Matthews, and D. L. Ball, "(18)F-FDG PET provides high-impact and powerful prognostic stratification in staging newly diagnosed non-small cell lung cancer," *J Nucl Med*, vol. 42, pp. 1596-604, 2001.

[19] S. F. Hain, K. M. Curran, A. D. Beggs, I. Fogelman, M. J. O'Doherty, and M. N. Maisey, "FDG-PET as a "metabolic biopsy" tool in thoracic lesions with indeterminate biopsy," *Eur J Nucl Med*, vol. 28, pp. 1336-40, 2001.

[20] D. Shaham and L. Guralnik, "The solitary pulmonary nodule: radiologic considerations," *Semin Ultrasound CT MR*, vol. 21, pp. 97-115, 2000.

[21] J. J. Erasmus, J. E. Connolly, H. P. McAdams, and V. L. Roggli, "Solitary pulmonary nodules: Part I. Morphologic evaluation for differentiation of benign and malignant lesions," *Radiographics*, vol. 20, pp. 43-58, 2000.

[22] J. J. Erasmus, H. P. McAdams, and J. E. Connolly, "Solitary pulmonary nodules: Part II. Evaluation of the indeterminate nodule," *Radiographics*, vol. 20, pp. 59-66, 2000.

[23] M. J. Liptay, "Solitary pulmonary nodule: treatment options," *Chest*, vol. 116, pp. 517S-518S, 1999.

[24] K. Higashi, Y. Ueda, Y. Arisaka, T. Sakuma, Y. Nambu, M. Oguchi, H. Seki, S. Taki, H. Tonami, and I. Yamamoto, "18F-FDG uptake as a biologic prognostic factor for recurrence in patients with surgically resected non-small cell lung cancer," *J Nucl Med*, vol. 43, pp. 39-45, 2002.

[25] R. J. Hicks, V. Kalff, M. P. MacManus, R. E. Ware, A. F. McKenzie, J. P. Matthews, and D. L. Ball, "The utility of (18)F-FDG PET for suspected recurrent non-small cell lung cancer after potentially curative therapy: impact on management and prognostic stratification," *J Nucl Med*, vol. 42, pp. 1605-13, 2001.

[26] H. Vesselle, R. A. Schmidt, J. M. Pugsley, M. Li, S. G. Kohlmyer, E. Vallires, and D. E. Wood, "Lung cancer proliferation correlates with [F-18]fluorodeoxyglucose uptake by positron emission tomography," *Clin Cancer Res*, vol. 6, pp. 3837-44, 2000.

[27] M. K. Gould and G. A. Lillington, "Strategy and cost in investigating solitary pulmonary nodules," *Thorax*, vol. 53 Suppl 2, pp. S32-7, 1998.

[28] N. A. Dewan, S. D. Reeb, N. C. Gupta, L. S. Gobar, and W. J. Scott, "PET-FDG imaging and transthoracic needle lung aspiration biopsy in evaluation of pulmonary lesions. A comparative risk-benefit analysis," *Chest*, vol. 108, pp. 441-6, 1995.

[29] Q. S. Chen, M. S. Weinhous, F. C. Deibel, J. P. Ciezki, and R. M. Macklis, "Fluoroscopic study of tumor motion due to breathing: facilitating precise radiation therapy for lung cancer patients," *Med Phys*, vol. 28, pp. 1850-6, 2001.

[30] M. Martinelli, D. Townsend, C. Meltzer, and V. V. Villemagne, "7. Survey of Results of Whole Body Imaging Using the PET/CT at the University of Pittsburgh Medical Center PET Facility," *Clin Positron Imaging*, vol. 3, pp. 161, 2000.

[31] C. F. Mountain, "Revisions in the international system for staging lung cancer," *Chest*, vol. 111, pp. 1710-1717, 1997.

[32] D. Lardinois, W. Weder, T. F. Hany, E. M. Kamel, S. Korom, B. Seifert, G. K. von Schulthess, and H. C. Steinert, "Staging of non-small-cell lung cancer with integrated positron-emission tomography and computed tomography," vol. 348, 2003, pp. 2500-2507.

[33] P. Giraud, D. Grahek, F. Montravers, M. F. Carette, E. Deniaud-Alexandre, F. Julia, J. C. Rosenwald, J. M. Cosset, J. N. Talbot, M. Housset, and E. Touboul, "CT and (18)F-deoxyglucose (FDG) image fusion for optimization of conformal radiotherapy of lung cancers," *Int J Radiat Oncol Biol Phys*, vol. 49, pp. 1249-57, 2001.

[34] M. J. Yaffe and J. A. Rowlands, "X-ray detectors for digital radiography," *Physics in Medicine and Biology*, vol. 42, pp. 1-40, 1997.

[35] M. L. Giger and S. G. Armato, "Current status and future direction of computer-aided diagnosis in chest CT," *International Congress Series*, vol. 1230, 2001.

[36] S. G. Armato, M. L. Giger, and H. MacMahon, "Automated detection of lung nodules in CT scans: preliminary results," *Med Phys*, vol. 28, pp. 1552-61, 2001.

[37] R. Bar-Shalom, N. Yefremov, L. Guralnik, D. Gaitini, A. Frenkel, A. Kuten, H. Altman, Z. Keidar, and O. Israel, "Clinical performance of PET/CT in evaluation of cancer: additional value for diagnostic imaging and patient management," *J Nucl Med*, vol. 44, pp. 1200-9, 2003.

[38] C. B. Caldwell, K. Mah, Y. C. Ung, C. E. Danjoux, J. M. Balogh, S. N. Ganguli, and L. E. Ehrlich, "Observer variation in contouring gross tumor volume in patients with poorly defined non-small-cell lung tumors on CT: the impact of 18FDG-hybrid PET fusion," *Int J Radiat Oncol Biol Phys*, vol. 51, pp. 923-31, 2001.

[39] P. C. Shrimpton, M. C. Hillier, M. A. Lewis, and M. Dunn, *Doses from computed tomography (CT) examinations in the UK-2003 review*: NRPB, 2005.

[40] J. S. Karp, M. E. Daube-Witherspoon, E. J. Hoffman, T. K. Lewellen, J. M. Links, W. H. Wong, R. D. Hichwa, M. E. Casey, J. G. Colsher, R. E. Hitchens, and et al., "Performance standards in positron emission tomography," *J Nucl Med*, vol. 32, pp. 2342-50, 1991.

[41] S. A. Nehmeh, Y. E. Erdi, K. E. Rosenzweig, H. Schoder, S. M. Larson, O. D. Squire, and J. L. Humm, "Reduction of respiratory motion artifacts in PET imaging of lung cancer by respiratory correlated dynamic PET: methodology and comparison with respiratory gated PET," *J Nucl Med*, vol. 44, pp. 1644-8, 2003.

[42] J. Skalski, R. L. Wahl, and C. R. Meyer, "Comparison of mutual information-based warping accuracy for fusing body CT and PET by 2 methods: CT mapped

onto PET emission scan versus CT mapped onto PET transmission scan," *J Nucl Med*, vol. 43, pp. 1184-7, 2002.

[43] P. E. Kinahan, D. W. Townsend, T. Beyer, and D. Sashin, "Attenuation correction for a combined 3D PET/CT scanner," *Med Phys*, vol. 25, pp. 2046-53, 1998.

[44] D. Visvikis, Lamare F., Bruyant P., Boussion N., and C. Cheze Le Rest, "Respiratory motion in positron emission tomography for oncology applications : Problems and solutions," *Nuclear Instruments & Methods in Physics Research, A*, vol. 569, pp. 453-57, 2006.

[45] J. W. Keyes Jr, "SUV: standard uptake or silly useless value?," vol. 36: Soc Nuclear Med, 1995, pp. 1836-1839.

[46] A. S. Bryant, R. J. Cerfolio, K. M. Klemm, and B. Ojha, "Maximum standard uptake value of mediastinal lymph nodes on integrated FDG-PET-CT predicts pathology in patients with non-small cell lung cancer," *The Annals of thoracic surgery*, vol. 82, pp. 417-423, 2006.

[47] J. A. Thie, K. F. Hubner, and G. T. Smith, "The diagnostic utility of the lognormal behavior of PET standardized uptake values in tumors," *J Nucl Med*, vol. 41, pp. 1664-72, 2000.

[48] M. Reinhardt, M. Beu, H. Vosberg, H. Herzog, A. Hubinger, H. Reinauer, and H. W. Muller-Gartner, "Quantification of glucose transport and phosphorylation in human skeletal muscle using FDG PET," *J Nucl Med*, vol. 40, pp. 977-85, 1999.

[49] D. J. Kim, B. R. Murray, R. Halperin, and W. H. Roa, "Held-breath self-gating technique for radiotherapy of non-small-cell lung cancer: a feasibility study," *Int J Radiat Oncol Biol Phys*, vol. 49, pp. 43-9, 2001.

[50] H. D. Kubo and L. Wang, "Introduction of audio gating to further reduce organ motion in breathing synchronized radiotherapy," *Med Phys*, vol. 29, pp. 345-50, 2002.

[51] K. E. Sixel, M. C. Aznar, and Y. C. Ung, "Deep inspiration breath hold to reduce irradiated heart volume in breast cancer patients," *Int J Radiat Oncol Biol Phys*, vol. 49, pp. 199-204, 2001.

[52] N. M. S. Groot, M. Bootsma, E. T. Velde, and M. J. Schalij, "Three-dimensional catheter positioning during radiofrequency ablation in patients: first application of a real-time position management system," *Journal of Cardiovascular Electrophysiology*, vol. 11, pp. 1183-1192, 2000.

[53] T. Pan, T. Y. Lee, E. Rietzel, and G. T. Y. Chen, "4D-CT imaging of a volume influenced by respiratory motion on multi-slice CT," *Medical physics*, vol. 31, pp. 333, 2004.

[54] S. A. Nehmeh, Y. E. Erdi, C. C. Ling, K. E. Rosenzweig, O. D. Squire, L. E. Braban, E. Ford, K. Sidhu, G. S. Mageras, S. M. Larson, and J. L. Humm, "Effect of respiratory gating on reducing lung motion artifacts in PET imaging of lung cancer," *Med Phys*, vol. 29, pp. 366-71, 2002.

[55] S. A. Nehmeh, Y. E. Erdi, C. C. Ling, K. E. Rosenzweig, H. Schoder, S. M. Larson, H. A. Macapinlac, O. D. Squire, and J. L. Humm, "Effect of respiratory gating on quantifying PET images of lung cancer," *J Nucl Med*, vol. 43, pp. 876-81, 2002.

[56] R. I. Berbeco, S. Nishioka, H. Shirato, G. T. Y. Chen, and S. B. Jiang, "Residual motion of lung tumours in gated radiotherapy with external respiratory surrogates," *Physics in Medicine and Biology*, vol. 50, pp. 3655-3668, 2005.

[57] Y. Seppenwoolde, R. I. Berbeco, S. Nishioka, H. Shirato, and B. Heijmen, "Accuracy of tumor motion compensation algorithm from a robotic respiratory tracking system: a simulation study," *Medical Physics*, vol. 34, pp. 2774, 2007.

[58] A. Rahmim, "Advanced Motion Correction Methods in PET," *Iran J Nucl Med*, vol. 13, pp. 1-17, 2005.

[59] Y. Wang, H. Baghaei, H. Li, Y. Liu, T. Xing, J. Uribe, R. Ramirez, S. Xie, S. Kim, and W.-H. Wong, "A Simple Respiration Gating Technique and Its Application in High-Resolution PET Camera," *IEEE Trans. Nuclear Science*, vol. 52, pp. 125 - 129, 2005.

[60] J. Wang, J. Byrne, J. Franquiz, and A. J. McGoron, "Evaluation of amplitude-based sorting algorithm to reduce lung tumor blurring in PET images using 4D NCAT phantom," *Comput Methods Programs Biomed*, vol. 87, pp. 112-22, 2007.

[61] F. Lamare, T. Cresson, J. Savean, C. Cheze Le Rest, A. J. Reader, and D. Visvikis, "Respiratory motion correction for PET oncology applications using affine transformation of list mode data," *Phys Med Biol*, vol. 52, pp. 121-40, 2007.

[62] F. Qiao, J. Clark, T. Pan, and O. Mawlawi, "Expectation Maximization Reconstruction of PET Image with Non-rigid Motion Compensation," *Conf Proc IEEE Eng Med Biol Soc*, vol. 4, pp. 4453-6, 2005.

[63] I. El Naqa, D. A. Low, J. D. Bradley, M. Vicic, and J. O. Deasy, "Deblurring of breathing motion artifacts in thoracic PET images by deconvolution methods," *Med Phys*, vol. 33, pp. 3587-600, 2006.

[64] F. Qiao, T. Pan, J. W. Clark, and O. R. Mawlawi, "Region of interest motion compensation for PET image reconstruction," *Phys Med Biol*, vol. 52, pp. 2675-89, 2007.

[65] M. Dawood, F. Buther, X. Jiang, and K. P. Schafers, "Respiratory motion correction in 3-D PET data with advanced optical flow algorithms," *IEEE Transactions on Medical Imaging*, vol. 27, pp. 1164-1175, 2008.

[66] M. Dawood, N. Lang, X. Jiang, and K. P. Schafers, "Lung motion correction on respiratory gated 3-D PET/CT images," *IEEE Trans Med Imaging*, vol. 25, pp. 476-85, 2006.

[67] B. Thorndyke, E. Schreibmann, A. Koong, and L. Xing, "Reducing respiratory motion artifacts in positron emission tomography through retrospective stacking," *Med Phys*, vol. 33, pp. 2632-41, 2006.

[68] W. P. Segars, B. M. Tsui, and A. J. D. Silva, "CT-PET image fusion using the 4D NCAT phantom with the purpose of attenuation correction," *IEEE Trans. Nuclear Science*, vol. 3, pp. 1775 - 1779 2002.

[69] W. P. Segars and B. M. Tsui, "Study of the efficacy of respiratory gating in myocardial SPECT with the new 4D NCAT phantom," *IEEE Trans. Nuclear Science*, vol. 49, pp. 675-679, 2002.

[70] W. P. Segars, D. S. Lalush, and B. M. Tsui, "Modeling respiratory mechanics in the MCAT and spline-based MCAT phantoms," *IEEE Trans. Nuclear Science*, vol. 48, pp. 89 - 97, 2001.

[71] W. P. Segars, "Development of a new dynamic NURBS-based cardiac torso (NCAT) phantom," *PhD dissertation, The University of North Carolina*, 2001.

[72] A. M. Loening and S. S. Gambhir, "AMIDE: a free software tool for multimodality medical image analysis," *Molecular Imaging*, vol. 2, pp. 131-137, 2003.

[73] G. G. Zhang, T. C. Huang, T. Guerrero, K. P. Lin, C. Stevens, G. Starkschall, and K. Forster, "Use of three-dimensional (3D) optical flow method in mapping 3D anatomic structure and tumor contours across four-dimensional computed tomography data," *J Appl Clin Med Phys*, vol. 9, pp. 2738, 2008.

[74] M. Dawood, F. Buther, N. Lang, O. Schober, and K. P. Schafers, "Respiratory gating in positron emission tomography: a quantitative comparison of different gating schemes," *Med Phys*, vol. 34, pp. 3067-76, 2007.

[75] L. Greer and C. Scarfone, "Data Spectrum's SPECT User's Manual," *Data Spectrum Corporation*, vol. 437, 1999.

[76] M. del Valle, M. Goryawala, and A. J. McGoron, "Dynamic lung tumor phantom coupled with chest motion," presented at Medical Imaging 2008: Visualization, Image-guided Procedures, and Modeling, San Diego, CA, USA, 2008.

[77] P. Razifar, M. Lubberink, H. Schneider, B. Langstrom, E. Bengtsson, and M. Bergstrom, "Non-isotropic noise correlation in PET data reconstructed by FBP but not by OSEM demonstrated using auto-correlation function," *BMC Med Imaging*, vol. 5, pp. 3, 2005.

[78] A. F. Laine, S. Schuler, J. Fan, and W. Huda, "Mammographic feature enhancement by multiscale analysis," *IEEE Trans Med Imaging*, vol. 13, pp. 725-40, 1994.

[79] K. V. Mardia and T. J. Hainsworth, "A spatial thresholding method for image segmentation," *IEEE transactions on pattern analysis and machine intelligence*, vol. 10, pp. 919-927, 1988.

[80] J. Fan, D. K. Y. Yau, A. K. Elmagarmid, and W. G. Aref, "Automatic image segmentation by integrating color-edge extraction and seeded region growing," *IEEE Transactions on Image Processing*, vol. 10, pp. 1454-1466, 2001.

[81] J. L. Barron, D. J. Fleet, and S. S. Beauchemin, "Performance of optical flow techniques," *International journal of computer vision*, vol. 12, pp. 43-77, 1994.

[82] F. G. Duhaylongsod, V. J. Lowe, E. F. Patz, Jr., A. L. Vaughn, R. E. Coleman, and W. G. Wolfe, "Lung tumor growth correlates with glucose metabolism measured by fluoride-18 fluorodeoxyglucose positron emission tomography," *Ann Thorac Surg*, vol. 60, pp. 1348-52, 1995.

[83] B. D. Lucas and T. Kanade, "An iterative image registration technique with an application to stereo vision," 1981.

[84] B. D. Lucas, "Generalized image matching by the method of differences," 1985.

[85] B. K. P. Horn and B. G. Schunck, "Determining optical flow," *Computer vision*, vol. 17, pp. 185-203, 1981.

[86] J. Ashburner and K. J. Friston, "Rigid body registration," *Human Brain Function 振 rackowiak RS, Friston KJ, Frith CD, et al, eds*, pp. 635?5, 2003.

[87] S. A. Nehmeh and Y. E. Erdi, "Respiratory Motion in Positron Emission Tomography/Computed Tomography : A Review," *Seminars in nuclear medicine*, vol. 38, pp. 167-76, 2008.

[88] L. Livieratos, L. Stegger, P. M. Bloomfield, K. Schafers, D. L. Bailey, and P. G. Camici, "Rigid-body transformation of list-mode projection data for respiratory motion correction in cardiac PET," *Phys Med Biol*, vol. 50, pp. 3313-22, 2005.

VITA

JIALI WANG

February 19, 1980	Born, Nantong, Jiangsu, P.R.China
2003	B.E., Biomedical Engineering Zhejiang University Hangzhou, Zhejiang, P.R.China
2005	M.S., Biomedical Engineering Florida International University Miami, Florida
2005 - 2009	Doctorate in Philosophy, Biomedical Engineering Florida International University Miami, Florida

PUBLICATIONS AND PRESENTATIONS

Wang, J., J. Franquiz, and A.J. McGoron, "Comparison of Respiratory Motion Correction Methods in PET Lung Tumor Quantification," *IFMBE Proceedings* 24, p. 63-66. 2009.

McGoron, A.J., Wang, J., et al, "Quantative Comparison of Two Gating Schemes in Lung PET: Simulation with Computer Phantom," *Biomedical Engineering, Recent Developments,* 2008, p. 27-32, ISBN 978-1-930636-07-1.

Wang, J., Valle, D.M., et al, "Automated Lung Tumor Detection and Quantification for Respiratory Gated PET/CT Images," Image Processing, *Proc. SPIE, Int. Soc. Opt. Eng.* Volume 6914, p. 69144G 1-10, 2008.

Goryawalaa, Z.M., Valle, D.M., Wang, J., et al, "Low-cost Respiratory Motion Tracking System," Visualization, Image-guided Procedures and Modeling, *Proc. SPIE, Int. Soc. Opt. Eng.* Volume 6918, p. 691822 1-12, 2008.

Wang, J., Byrne, J., Franquiz, J, McGoron, A.J., "Evaluation of Amplitude-based Sorting Algorithm to Reduce Lung Tumor Blurring in PET Images Using 4D NCAT Phantom," *Computer Methods and Programs in Biomedicine*, Volume 87, Issue 2, p. 112-122, 2007.

Wang, J., McGoron, A.J., et al, "Respiratory Gating System Design for Motion Tracking in PET Molecular Imaging," *Proceedings of the Biomedical Engineering Society*, Chicago, IL. October 11-14, 2006.

Wang, J., McGoron, A.J., Byrne, J., Franquiz, J, "A Novel PET Respiratory Gating Algorithm to Reduce Lung Tumor Blurring Using the 4D NCAT Phantom," *Medical Physics*, Volume 33, Issue 6, p. 2278, August 2006.

Wang, J., McGoron, A.J., et al, "Tracking of Lung Tumor Motion during Respiration in PET/CT, Device Development," *Proceedings of ASME Summer Bioengineering Conference*, June 2006.

Wang, J., McGoron, A.J., et al, "Amplitude Sorting Method to Compensate for Breathing Induced Motion Artifacts in PET/CT," *Proceedings of ASME Summer Bioengineering Conference*, June 2006.